

**The Cooling and Lubrication Performance of Graphene Platelets in
Micro-Machining Environments**

by

Bryan Chu

A Thesis Submitted to the Graduate
Faculty of Rensselaer Polytechnic Institute

in Partial Fulfillment of the
Requirements for the degree of
DOCTOR OF PHILOSOPHY

Major Subject: Mechanical Engineering

Approved by the
Examining Committee:

Johnson Samuel, Thesis Adviser

Nikhil Koratkar, Member

Yunfeng Shi, Member

Daniel Walczyk, Member

Rensselaer Polytechnic Institute
Troy, New York

April 2016
(For Graduation May 2016)

© Copyright 2016

by

Bryan Chu

All Rights Reserved

Chapter 3 © 2013 by American Scientific Publishers

Chapters 4, 5, and 6 © 2015 by American Society of Mechanical Engineers

CONTENTS

LIST OF TABLES.....	vi
LIST OF FIGURES.....	vii
ACKNOWLEDGMENT.....	ix
ABSTRACT.....	xi
1. INTRODUCTION.....	1
1.1 Motivation and Background.....	1
1.2 Research Objectives, Scope, and Tasks.....	3
1.3 Thesis Outline.....	5
2. LITERATURE REVIEW.....	7
2.1 Graphene and Graphene Platelets.....	7
2.1.1 Structure and Properties.....	7
2.1.2 Fabrication Routes.....	9
2.1.3 Applications Relevant to Machining.....	11
2.2 Graphene Composites.....	13
2.2.1 Fabrication Routes.....	13
2.2.2 Properties and Applications.....	15
2.2.3 Machining of Graphene Composites.....	17
2.3 Machining Mechanics.....	18
2.3.1 Experimental Methods.....	18
2.3.2 Analytical Models.....	20
2.3.3 Computational Models.....	22
2.4 Cutting Fluids.....	25
2.4.1 Summary of Relevant Properties.....	25
2.4.2 Role in Machining Mechanics.....	26
2.5 Transition Metal-Catalyzed Diamond Tool Wear.....	28
2.5.1 Thermodynamic and Chemical Basis.....	28
2.5.2 Mitigation of Transition Metal-Catalyzed Diamond Tool Wear.....	29
2.6 Gaps in Knowledge and Need for Research.....	31
3. EMBEDDED DELIVERY USING HIERARCHICAL GRAPHENE COMPOSITES.....	33
3.1 Material Synthesis and Mechanical Property Characterization.....	33
3.1.1 Graphene Platelets.....	33
3.1.2 Hierarchical Three-Phase Composite.....	34
3.1.3 Material Properties.....	36
3.2 Micro-milling Experiment Design.....	37
3.3 Experimental Observations.....	38
3.3.1 Microtool Wear Characteristics.....	38
3.3.2 Chip Morphology.....	40
3.3.3 Cutting Forces.....	44
3.3.4 Surface Roughness.....	46
3.3.5 Fiber-Matrix Debonding.....	47

3.4	Summary	49
4.	EXTERNAL DELIVERY USING GRAPHENE-ENHANCED ENVIRONMENTALLY-BENIGN CUTTING FLUIDS	51
4.1	Experimental Details.....	51
4.1.1	Dispersion of Graphene Platelets.....	51
4.1.2	Dispersion Characteristics.....	52
4.1.3	Micro-Machining Experimental Setup.....	54
4.1.4	Cutting Temperatures.....	55
4.1.5	Cutting Forces	56
4.1.6	Surface Roughness	57
4.2	Results and Discussion.....	57
4.3	Summary	58
5.	EXTERNAL DELIVERY USING GRAPHENE OXIDE COLLOIDAL SUSPENSIONS AS CUTTING FLUIDS	60
5.1	Graphene Oxide Platelet Fabrication and Characterization.....	60
5.1.1	Graphene Oxide Platelet Fabrication	60
5.1.2	Dimensional Characterization of Graphene Oxide Platelets.....	63
5.1.3	Cutting Fluid Fabrication	67
5.2	Micro-machining Performance Evaluation Experiments.....	68
5.2.1	Experimental Setup	68
5.2.2	Cutting Temperature and Cutting Force	70
5.2.3	Surface Roughness	72
5.3	Discussion	73
5.4	Summary	74
6.	DROPLET DYNAMICS AND FILM FORMATION MECHANISMS OF GRAPHENE OXIDE COLLOIDAL SUSPENSIONS	76
6.1	Experimental Setup for the Single-droplet Impingement Study.....	76
6.2	Experimental Findings	78
6.2.1	Droplet Temperature Profile	78
6.2.2	Droplet Evaporation: Pinning Regime	82
6.2.3	Droplet Evaporation: Receding Regime	84
6.2.4	Residual Graphene Oxide Film Characterization	86
6.3	Discussion	89
6.3.1	Film-Formation Hypothesis	89
6.3.2	Experimental Validation	92
6.4	Summary	94
7.	CHEMICAL WEAR MITIGATION MECHANISMS OF GRAPHENE DURING DIAMOND CUTTING OF STEEL.....	96
7.1	Review of Experimental Findings.....	96
7.2	Interatomic Force Fields and Molecular Dynamics Simulations.....	98
7.2.1	Selection of Interatomic Force Field.....	98
7.2.2	Force Field Evaluation	99
7.2.3	Nanometric Cutting Simulation	103
7.3	Simulation Results	107

7.3.1	Wear and Graphitization Analysis	109
7.3.2	Carbon Transfer Analysis	112
7.4	Discussion	114
7.4.1	Comparison to Experimental Results.....	114
7.4.2	Observed Mechanisms	115
7.5	Summary	118
8.	CONCLUSIONS AND RECOMMENDATIONS	119
8.1	Conclusions.....	119
8.1.1	Embedded Delivery Using Hierarchical Graphene Composites	120
8.1.2	External Delivery Using Graphene-Enhanced Environmentally-Benign Cutting Fluids	121
8.1.3	External Delivery Using Graphene Oxide Colloidal Suspensions as Cutting Fluids.....	122
8.1.4	Droplet Dynamics and Film Formation Mechanisms of Graphene Oxide Colloidal Suspensions	123
8.1.5	Chemical Wear Mitigation Mechanisms of Graphene During Diamond Cutting of Steel.....	125
8.2	Recommendations for Future Work.....	126
8.2.1	Experimental Studies	126
8.2.2	Modeling Studies	127
	References.....	129
	Author's Biography	144

LIST OF TABLES

Table 3.1: Material properties of composites	36
Table 3.2: Cutting conditions for hierarchical composite milling	37
Table 4.1: Cutting conditions for turning with graphene-enhanced canola oil	55
Table 5.1: Dimensional characterization of graphene oxide platelets	66
Table 5.2: Properties of graphene oxide suspensions in semi-synthetic cutting fluid.....	69
Table 5.3: Turning conditions using graphene-enhanced semi-synthetic cutting fluid...	70
Table 6.1: Experimental conditions for droplet impingement study	78
Table 6.2: Lubrication and cooling performance of graphene oxide platelet solutions ..	90
Table 7.1: Summary of machining conditions in Smith <i>et al.</i>	97
Table 7.2: Equilibration simulation results compared to published values	100
Table 7.3: Geometric and cutting parameters for molecular dynamics simulations	106
Table 7.4: Molecular dynamics cutting simulation details	107
Table 7.5: Cutting conditions measured and averaged on the tool.....	109

LIST OF FIGURES

Figure 1.1: Outline of research objective and its relation to thrust areas	4
Figure 2.1: Scanning electron micrograph of graphene crystal	7
Figure 2.2: Schematic of covalent functionalization of graphene oxide by fullerene	8
Figure 2.3: A non-contact AFM image of exfoliated graphene oxide sheets	9
Figure 2.4: Schematic representation of graphene oxide platelet fabrication	9
Figure 2.5: Atomistic model of the graphite oxide to graphene transition.....	10
Figure 2.6: Schematic of ultrasonically assisted exfoliation aided by surfactant.....	11
Figure 2.7: Tribological parameters of flake/nano-sheet graphite versus concentration. 12	12
Figure 2.8: Trends in cutting parameters encountered for various nano-scale additives 12	12
Figure 2.9: Dispersion of graphene sheets in epoxy-matrix <i>via</i> solution mixing.....	13
Figure 2.10: Schematic of <i>in-situ</i> formation of polystyrene-graphene nano-composite . 14	14
Figure 2.11: Procedure for graphene reinforcement of metal matrix	14
Figure 2.12: Ultrasound porosity analysis of hierarchical graphene composite.....	15
Figure 2.13: Schematic representation of O ₂ molecules following a “tortuous path”	16
Figure 2.14: Flexible interleaved structure consisting of GNSs and Fe ₃ O ₄ particles	16
Figure 2.15: Methylene blue in solution after 10 min stirring in dark	17
Figure 2.16: Surface morphology of machined graphene composite	17
Figure 2.17: Conventional features of turning tool wear measurement.	18
Figure 2.18: Temperature measurement in machining	19
Figure 2.19: Theoretical surface profile in micro-milling	19
Figure 2.20: Effect of aluminum crystallographic orientation on cutting parameters.....	20
Figure 2.21: Condensed Merchant’s circle diagram.....	20
Figure 2.22: Typical distributions in continuous-chip formation.....	21
Figure 2.23: Edge radius size effect	21
Figure 2.24: End milling of ductile iron workpiece	22
Figure 2.25: Serrated chip formation.....	22
Figure 2.26: Damage observed in Al-SiC MMC using FEM.....	23
Figure 2.27: Schematic of common MD setup for simulation of nanometric cutting	24
Figure 2.28: Displacement of worn atoms in MD simulated diamond tool	24
Figure 2.29: Difference between conventional and MQL application of cutting fluids..	25
Figure 2.30: Comparison of G-ratio for various cutting fluids and nanofluids.....	26
Figure 2.31: Mechanisms for cutting fluid access to rake face.	27
Figure 2.32: Parameterization of rotating droplet shape.	27
Figure 2.33: Reaction coordinate diagram of the diamond↔graphite transformation....	28
Figure 2.34: Diamond wear mechanisms simulated with molecular dynamics	29
Figure 2.35: Schematic of surface nitriding of steel.....	30
Figure 2.36: Possible chemical pathways for carbon diffusion.....	31
Figure 3.1: High resolution transmission electron microscopy of graphene platelets.....	34
Figure 3.2: Microstructure details of the hierarchical three-phase graphene composite. 35	35
Figure 3.3: Setup for micro-milling of hierarchical composite	37
Figure 3.4: Micro-tool geometry after cutting at a velocity of 62m/min.....	38
Figure 3.5: Tool wear pattern seen at a cutting velocity of 62m/min and FPT of 1µm ..	39
Figure 3.6: Morphology of the chips collected at cutting velocity 30m/min	41
Figure 3.7: Close-up of Figure 3.6 showing fiber failure modes.....	41

Figure 3.8: Concept of effective fiber failure length for the same depth-of-cut.....	43
Figure 3.9: SEM image of the floor of the machined slots.....	44
Figure 3.10: Cutting force signals and spectra in hierarchical composite milling	45
Figure 3.11: Peak-to-valley cutting forces in hierarchical composite milling.....	45
Figure 3.12: Surface roughness trends in hierarchical composite milling.....	47
Figure 3.13: Surface scan of the top of the machined slots	48
Figure 3.14: Side-wall images taken along the climb milling side of the slot.....	48
Figure 4.1: Characterization of a typical graphene platelet.	52
Figure 4.2: Characteristics of graphene-enhanced canola oil.....	53
Figure 4.3: Schematic of micro-turning setup	54
Figure 4.4: Cooling performance of graphene-enhanced canola oils	56
Figure 4.5: Average resultant cutting force for graphene-enhance canola oils	56
Figure 4.6: Surface roughness at slot centerline for graphene-enhanced canola oils.....	57
Figure 5.1: Overall process flow for preferred methods of GOP production	61
Figure 5.2: X-Ray diffraction data of GO	61
Figure 5.3: SEM images of GOP	63
Figure 5.4: DLS data showing the statistical distribution of various GOP sizes.....	64
Figure 5.5: BET adsorption-desorption isotherms for TR GOP powders	65
Figure 5.6: Experimental setup with inset showing thermocouple bead location	70
Figure 5.7: Cutting temperature and force trends seen for the GOP colloidal solutions. 71	
Figure 5.8: Surface roughness trends seen for GOP colloidal solutions	73
Figure 6.1: Experimental setup for single-droplet impingement study	77
Figure 6.2: Characteristic temperature profile of a 0.2 wt% TR500 droplet.....	79
Figure 6.3: Numerical metrics for comparing temperature profiles	80
Figure 6.4: Characteristic temperature profile of a 1.0 wt% US GOP solution	81
Figure 6.5: Droplet height and contact angle during the pinning regime	82
Figure 6.6: Trends for multiplicative coefficients, α_h and α_θ	83
Figure 6.7: Trends for multiplicative coefficients, β_h and β_θ	83
Figure 6.8: Droplet evaporation behavior in the receding regime.....	84
Figure 6.9: Representative graphene oxide film profile scans.	87
Figure 6.10: Relative-frequency curves for thickness distribution.....	87
Figure 6.11: Hypothesized GOP film deposition at the tool–workpiece interface.....	91
Figure 6.12: Digital images of the turning tool showing GOP film formation.....	93
Figure 7.1: Volumetric tool wear patterns seen in region A-B-C-D.	97
Figure 7.2: Results of temperature-driven graphitization benchmarking simulation	101
Figure 7.3: Number of sp^2 hybridized atoms in the nano-particles	103
Figure 7.4: Initial configuration of workpiece, tool, and platelet in MD simulation	105
Figure 7.5: Screenshots of simulation progress	108
Figure 7.6: Final unworn tool and platelet configurations with coordination analysis .	110
Figure 7.7: Analysis of carbon transfer	113
Figure 7.8: Head-on view of the rake face of tool.....	115
Figure 7.9: Platelet cleaving mechanism	116
Figure 7.10: Interlayer sliding mechanism	118

ACKNOWLEDGMENT

This thesis is the culmination of five years of effort. As I reflect on the time spent on this work, I realize how lucky I have been for the support of those around me through the setbacks, delays, and occasional triumphs that marked my research. Above all else, I must thank my advisor, Professor Johnson Samuel, for his mentorship and guidance. I will be forever grateful to him for entrusting me with the responsibility of being his first doctoral student and the lead student on his first NSF grant as a professor. I can only hope that our shared experiences have influenced him as much as they have me. Finally, I must mention his impeccable ability to identify those who inspire success in others. Both within our group and outside, he has connected me with people who I sincerely believe have helped me succeed and *vice versa*, many of whom I will acknowledge below. I look forward to the continued success of Professor Samuel and his Nano/Micro-scale Manufacturing and Material (Nano-M3) Design Lab at Rensselaer Polytechnic Institute (RPI), in the manufacturing community, and beyond. I would also like to thank the National Science Foundation (Grant No. CMMI 11-30215) for sponsoring my thesis work. Without this funding, none of this would have been possible.

I would like to thank our co-PI on this work, Professor Nikhil Koratkar, his past graduate students, Dr. Eklavya Singh and Dr. Fazel Yavari, and visiting scholar Dr. Osman Eksik. Their expertise and facilities were instrumental in the fabrication and characterization of the graphene used in the experimental portion of this work. I thank Dr. Singh, in particular, for serving as a model of a successful graduate student for me to follow. I would also like to thank Professor Yunfeng Shi for serving on my committee and providing computing resources and consultation for the molecular dynamics (MD) study. I am also grateful to Professor Daniel Walczyk for serving on my committee. Acknowledgement is also given to Professor Walczyk and his former student Dr. Lai Jiang for allowing access to their kinematic viscosity measuring devices. I must also give thanks to Randy McDougal, Professor Diana Borca-Tasciuc, and Professor Thierry Blanchet for allowing the use of their Instron testing machines, thermal conductivity and tribological measurement equipment, respectively. Finally, I am extremely grateful for the preliminary work of Dr. Indira Sheshadri and Phil Smith, which formed the experimental basis for my MD simulation studies.

I am indebted to the support staff from the Mechanical, Aerospace, and Nuclear Engineering Department and from the Center for Automation Technologies and Systems at RPI. Special thanks go to Glenn Saunders, Dr. Steve Rock, Dr. Larry Ruff, Bill Mielke, Chris Sikora, Jeanette Young, Hollis McEvelly, Rose Boshoff, Esther Rendano, and Sue Miller. Each of you, in your own way, helped lift some of the burden of performing research at Rensselaer.

To my fellow and former graduate student colleagues in the Nano-M3 Design Lab, Clayson Spackman, Michael Conward, Kyle Picha, Robert Altman, Roshan Mishra, James Nowak, Curtis Bradley, Bill Carter, Robert Reeves, Robert Rizzolo, Andrew Nitschke, Jillian Hiu, and Robin Frank, I thank you for being there. Consulting with each of you on your projects was always refreshing. I hope that my presence was likewise appreciated and that my feedback helped you in your work too. I would also like to include John Lawler, Corey Li, John Lee and Chris Cave from Saturn Industries in this group. Although you were not a part of the Nano-M3 Design Lab, the projects we collaborated on were also fulfilling.

To my former undergraduate colleagues, David Silverman, Garrett Gross, Phil Smith, Larry Oligny, Jacob Merson, Christina Pacifico, Anthony Peto, Kyle Mattson, Nathan Montiminy, Yuzo Uchiyama, and Ben Jacoby, I very much valued our time together. It was heartening to see many of you transition to graduate school while working with me. I wish you the best in your current stations. To my current undergraduate colleagues, Clare Severance and Charles Parslow, you are in good company. I sincerely believe that you are fully capable of taking the reins of my work and running with it after I leave RPI.

To my parents, George and Min, all I can say is that I am finally done. Thank you for encouraging me and supporting me all these years. To my closest friends, Tom Schmeelk and Andrew Lo, I am glad you dragged me away from graduate school from time-to-time to remind me what it was to have a life.

ABSTRACT

The research presented in this thesis is aimed at investigating the use of graphene platelets (GPL) to address the challenges of excessive tool wear, reduced part quality, and high specific power consumption encountered in micro-machining processes. There are two viable methods of introducing GPL into micro-machining environments, *viz.*, the *embedded delivery* method, where the platelets are embedded into the part being machined, and the *external delivery method*, where graphene is carried into the cutting zone by jetting or atomizing a carrier fluid.

The study involving the *embedded delivery* method is focused on the micro-machining performance of hierarchical graphene composites. The results of this study show that the presence of graphene in the epoxy matrix improves the machinability of the composite. In general, the tool wear, cutting forces, surface roughness, and extent of delamination are all seen to be lower for the hierarchical composite when compared to the conventional two-phase glass fiber composite. These improvements are attributed to the fact that graphene platelets improve the thermal conductivity of the matrix, provide lubrication at the tool-chip interface and also improve the interface strength between the glass fibers and the matrix.

The benefits of graphene are seen to also carry over to the *external delivery* method. The platelets provide improved cooling and lubrication performance to both environmentally-benign cutting fluids as well as to semi-synthetic cutting fluids used in micro-machining. The cutting performance is seen to be a function of the geometry (*i.e.*, lateral size and thickness) and extent of oxygen-functionalization of the platelet. Ultrasonically exfoliated platelets (with 2–3 graphene layers and lowest in-solution characteristic lateral length of 120 nm) appear to be the most favorable for micro-machining applications. Even at the lowest concentration of 0.1 wt%, they are capable of providing a 51% reduction in the cutting temperature and a 25% reduction in the surface roughness value over that of the baseline semi-synthetic cutting fluid. For the thermally-reduced platelets (with 4–8 graphene layers and in-solution characteristic lateral length of 562–2780 nm), a concentration of 0.2 wt% appears to be optimal. An investigation into the impingement dynamics of the graphene-laden colloidal solutions on a heated substrate reveals that the most important criterion dictating their machining performance

is their ability to form uniform, submicron thick films of the platelets upon evaporation of the carrier fluid. As such, the characterization of the residual platelet film left behind on a heated substrate may be an effective technique for evaluating different graphene colloidal solutions for cutting fluids applications in micromachining.

Graphene platelets have also recently been shown to reduce the aggressive chemical wear of diamond tools during the machining of transition metal alloys. However, the specific mechanisms responsible for this improvement are currently unknown. The modeling work presented in this thesis uses molecular dynamics techniques to shed light on the wear mitigation mechanisms that are active during the diamond cutting of steel when in the presence of graphene platelets. The dual mechanisms responsible for graphene-induced chemical wear mitigation are: 1) The formation of a physical barrier between the metal and tool atoms, preventing graphitization; and 2) The preferential transfer of carbon from the graphene platelet rather than from the diamond tool. The results of the simulations also provide new insight into the behavior of the 2D graphene platelets in the cutting zone, specifically illustrating the mechanisms of cleaving and interlayer sliding in graphene platelets under the high pressures in cutting zones.

1. INTRODUCTION

1.1 Motivation and Background

Micro-machining operations such as micro-milling, micro-drilling and micro-turning/hard-turning are currently used to manufacture a wide-range of precision micro-parts that are part of a multi-billion dollar market spanning industries such as defense, healthcare and consumer electronics [1-5]. These micro-machining operations are high-strain-rate deformation processes characterized by extreme cutting temperatures and cutting forces. These intense conditions adversely affect the life of the low-stiffness micro-tools and also reduce the life-cycle of the micro-part by inducing thermal damage and residual stresses [6, 7]. The situation is further complicated due to unique micro-scale phenomena, such as the elastic recovery of the workpiece and the minimum chip thickness effect [8-11], which lead to increased tool wear, tool failure, and degradation in the quality of the machined surface, especially while machining hard materials such as stainless steel and fiber-reinforced composites [5, 12-15]. These tool wear and dimensional accuracy issues are a major component of the costs associated with micro-machining and therefore demand an innovative solution.

The Nobel Physics Prize of 2010 awarded to Geim and Novoselov has generated enormous interest within the scientific community in investigating the use of graphene for engineering applications. Graphene is manufactured by splitting strong carbon-based layered materials such as graphite into individual atomic planes [16-18]. This splitting of layered graphite results in graphene or, more frequently, few-layered graphene platelets [19, 20], i.e., structures that are comprised of ~2-10 individual graphene sheets held together by van der Waals (vdW) forces. The micro-scale lateral dimensions and nano-scale thickness of GPL could allow them to effectively enter the micro-cutting zone and provide lubrication *via* interlayer sliding without affecting dimensional accuracy. This possibility, combined with the excellent thermal properties of graphene, make GPL an ideal fit for reducing tool wear in micro-machining applications.

There are two viable methods of introducing GPL into micro-machining environments, *viz.* ***embedded delivery*** and ***external delivery***. In the ***embedded delivery*** method, the platelets are embedded in the part to be machined. This allows the graphene

to influence the cooling and lubrication conditions during the cut, the failure mechanism of the work piece material, and consequently the tool wear. Recent work by Arora *et al.* [21] explored the effects of embedded delivery of graphene on the micro-machining of epoxy. This study revealed that the presence of GPL leads to improvements in the micro-machining responses of the epoxy composite. While these results look promising, epoxy is a fairly soft material that is easy to cut, even at the micro-scale. The success of the embedded delivery method for GPL can only be effectively tested by machining composites containing harder reinforcing phases, such as glass or carbon fibers, which are more likely to be used in high-performance applications. The recent development of hierarchical GPL composites containing glass fibers provides a candidate system for such an investigation [22]. The addition of graphene in this material improves its mechanical properties, but the micro-machining characteristics of this composite have yet to be investigated.

The *external delivery* method requires graphene to be carried into the cutting zone by jetting or atomizing a carrier fluid. In this method, the GPL serves the same role as a high-performance cutting fluid additive. Bulk graphite platelets (~15 μm lateral size, 20-60 graphene layers) are proven, effective cutting fluid additives, reducing tool wear for macro-scale machining purposes [23-24]. However, their use in micro-scale machining operations has been seen to significantly deteriorate the dimensional accuracy of the workpiece and also cause higher tool wear. These negative effects are attributed to the trapping of graphite agglomerations between the tool and workpiece during the micro-machining operation, which is due to the comparable length-scale of the graphite (~15 μm) and machined micro-feature size (~30 μm). The large number of graphene sheets within a single platelet also contributes to this problem. Graphene platelets, with lateral dimensions of 1-3 μm and having only 2-10 graphene sheets, are likely to provide a more suitable alternative for micro-machining applications. They have also been identified as a potential solution to the problem of chemical tool wear in diamond machining of transition metals [25]. However, their performance in micro-machining environments when delivered externally needs to be carefully investigated.

1.2 Research Objectives, Scope, and Tasks

The overall objective of this research is to study the cooling and lubrication performance of graphene platelets in micro-machining environments. In order to achieve this objective, research efforts have been focused on the following three thrust areas:

Thrust 1- Embedded Delivery: Studies in this thrust area will investigate the performance of GPL introduced into microstructured materials with a particular focus on its impacts on micro-machining responses. Specifically, machining studies on a three-phase hierarchical composite containing graphene, glass fibers, and epoxy will be undertaken. The metrics to be measured include chip morphology, tool wear, cutting forces, cutting temperatures, and surface roughness.

Thrust 2- External Delivery: Investigations in this thrust will involve enhancing the performance of both environmentally-benign and semi-synthetic cutting fluids using GPL additives. Experiments will be conducted to understand the effects of the addition of GPL on lubricity and cooling. Machining responses to be measured in these studies include cutting forces, cutting temperatures, and surface roughness. In addition, key cutting fluid properties, such as viscosity and thermal conductivity, will also be measured.

Thrust 3- Cooling and Lubrication Mechanisms: This thrust will first focus on single droplet impingement experiments to study more fundamental behaviors of the cutting fluids developed in Thrust 2. Specifically, the heat capacity, spreading behavior, and graphene film formation mechanisms will be examined. This thrust will also use molecular dynamics (MD) techniques to investigate the mechanisms responsible for the mitigation of chemical diamond tool wear when machining transition metals.

Figure 1.1 lays out the overall research objective and its relationship to the three thrust areas. This research will result in a thorough evaluation of GPL performance in different micro-machining scenarios. Findings from Thrust 1 may show that GPL

enhancement can increase the machinability of the otherwise difficult-to-machine fiber-reinforced composite in addition to enhancing its mechanical properties. This might eliminate the need for providing external cooling and lubrication when micro-machining this class of composites. Thrusts 2 and 3 will provide a scientific basis for designing the lateral dimensions and thickness of graphene platelets for use as high-performance cutting fluid additives. Ultimately, the findings of this research are expected to improve the overall efficiency of micro-machining operations used in critical applications in the areas of defense, healthcare and consumer electronics.

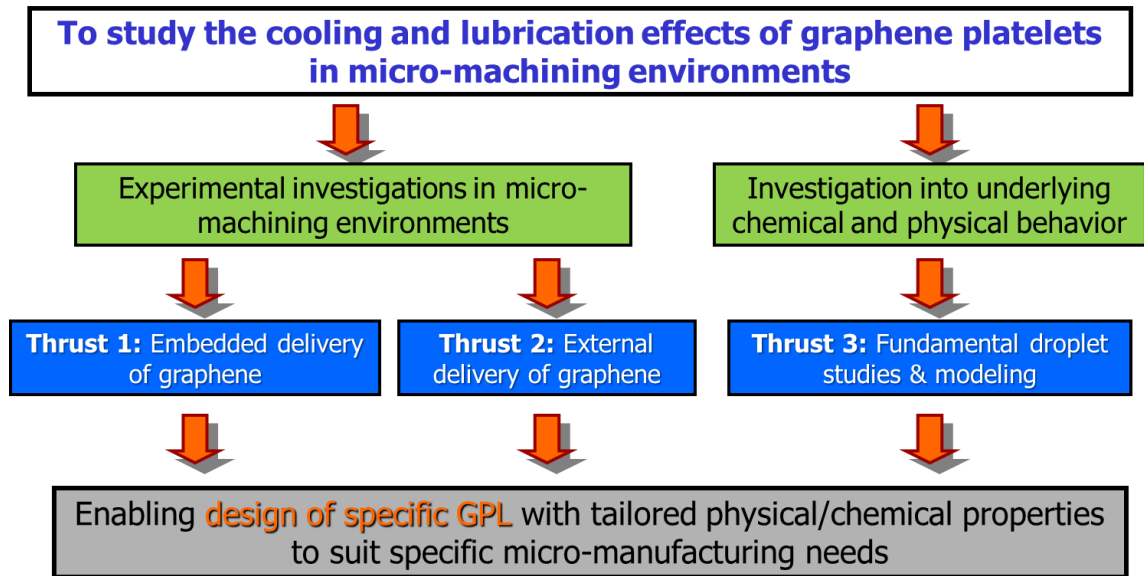


Figure 1.1: Outline of research objective and its relation to thrust areas. 1) Embedded delivery of graphene; 2) External delivery of graphene; and 3) Fundamental droplet studies and modeling

Scope: The study of embedded delivery of GPL will be limited to a hierarchical-GPL composite, consisting of micro-scale glass fibers that are held together in a graphene-laden epoxy matrix. The external delivery investigations will explore the use of both semi-synthetic and plant-based cutting fluids as carriers of GPL. The machining operations that will be used include micro-milling and micro-turning. The fundamental droplet studies will be limited to the cutting fluids formulated in Thrust 2. Finally, the diamond wear investigations will use steel as the transition metal workpiece in both the experimental work and MD simulations.

1.3 Thesis Outline

The remainder of the thesis is organized as follows. Chapter 2 provides a thorough review of the published literature in relevant areas. This chapter begins with an overview of the state-of-the-art in graphene, with a particular focus on its fabrication, properties and use with respect to tribological applications. After this, literature on the use of graphene in composite materials is presented. The next section summarizes literature regarding experimental, analytical, and computational models of machining mechanics. Then studies on cutting fluids, particularly nanofluids, are reviewed. This includes examining the behavior and tribological/rheological properties of these fluids that dictate their impact on machining mechanics. The chapter concludes with a review of transition metal-catalyzed diamond tool wear and proposed solutions to this problem.

Chapter 3 presents the results from the micro-milling experiments performed on hierarchical graphene composites and contrasts its machinability with that of a baseline, glass-fiber reinforced composite. The differences in machinability are characterized by metrics such as the tool wear, cutting forces, surface roughness, and fiber-matrix debonding. The work described in this chapter falls under Thrust 1 of the research tasks.

Chapter 4 focuses on the fabrication and use of an environmentally-benign cutting fluid enhanced with graphene. Here, graphene-enhanced canola oil is used in micro-turning experiments and its performance contrasted with dry machining and the baseline canola oil cutting fluid. The graphene-enhanced fluid is characterized to determine its dispersion characteristics, viscosity, thermal conductivity, and tribological behavior. Its impact on the machining process is characterized by cutting temperatures and cutting forces measured during the process, as well as surface roughness measured on the finished workpiece. This work falls under Thrust 2 of the research tasks.

Chapter 5 describes the experiments that are conducted to identify the relation between the cooling and lubrication performance of graphene-enhanced cutting fluids and the geometric and chemical properties of the constituent graphene platelets. First, the fabrication and characterization of graphene platelets of varying size and oxygen functionalization is presented. These graphene platelets are then dispersed in a semi-synthetic cutting fluid and the resulting fluids are analyzed to determine their viscosity and thermal conductivity. Micro-turning experiments are then conducted to evaluate the

impact of these solutions on cutting forces, cutting temperatures, and surface roughness. These experiments fall under Thrust 2 of the research tasks.

Chapter 6 details follow-up studies performed to explain the results presented in Chapter 5. Here, single droplet impingement studies are performed by depositing graphene-enhanced cutting fluids onto a heated substrate. The time evolution of the droplet shape, temperature, and graphene distribution are measured using high-speed data collection techniques. The nature of the residual graphene film formed upon evaporation of the fluid phase is also characterized. These metrics are then related back to the results of the machining presented in Chapter 5. The droplet studies are part of Thrust 3 of the research tasks.

Chapter 7 focuses on a simulation-based follow-up to the work presented in Smith *et al.* [25], which showed the mitigation of iron-catalyzed diamond tool wear by graphene-enhanced cutting fluids. Molecular dynamics simulations of nanometric cutting scenarios involving diamond tools, steel workpieces, and graphene are performed to shed light on the behavior observed during the experiments performed by Smith *et al.* [25]. This chapter presents details of the identification and evaluation of the appropriate MD potential and the results of the nanometric cutting simulation. From the simulation, wear rates, graphitization rates, carbon transfer, and specific physical/chemical mechanisms are identified and compared to the experimental results where possible. This MD simulation work falls under Thrust 3 of the research tasks.

Finally, Chapter 8 summarizes the significant findings drawn from the entirety of this research. The contribution of the work as a whole to the fundamental manufacturing science knowledge-base is identified. Possible pathways for future work are also proposed.

2. LITERATURE REVIEW

This chapter lays out the case for studying the use of graphene in micro-machining applications by presenting relevant literature regarding the properties of graphene as a material and its use in tribological and related applications. This will be followed by a review of machining mechanics and the use of cutting fluids in machining operations. Finally this chapter will cover the problem of transition metal-catalyzed diamond tool wear.

2.1 Graphene and Graphene Platelets

This section will review literature that describes graphene and graphene platelets along with various fabrication methods and its current use in applications relevant to machining processes.

2.1.1 Structure and Properties

Graphene is a 2-D nano-material in the form of a single atom thick, hexagonal network of carbon, as shown in Figure 2.1. For many years, graphene has been examined theoretically [26], but was considered unstable [27]. The first isolation of graphene from macro-scale graphite was performed by Geim and Novoselov, using a scotch-tape based peeling technique, for which they eventually won the 2010 Nobel Prize [17, 28]. A related material, graphene oxide, consists of the same type of carbon sheet, but functionalized with various oxygen moieties such as alcohol and epoxide functional groups [29]

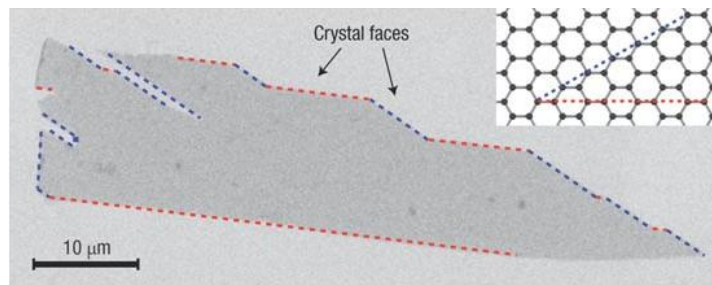


Figure 2.1: Scanning electron micrograph of graphene crystal with inset showing crystal faces [17]

Even before the isolation of single-layer graphene, many of its unique properties, such as its high conductivity in the absence of charge carriers [26] and high material strength [30], were predicted theoretically. Similar techniques were used to predict the

properties of related carbon nano-materials, such as carbon nanotubes (CNT) and fullerenes [30-32] and have been experimentally validated. With the work of Geim and Novoselov [17], many of the theorized properties of graphene were able to be confirmed experimentally, such as material yield strength on the order of gigapascals [18] and thermal conductivity of >1000 W/mK [33].

One of the interesting properties of graphene (and graphene oxide) is its proclivity for bonding. Both covalent bonding, using the myriad chemical interactions of elemental carbon, and non-covalent bonding, *via* π - π stacking and van der Waals (vdW) interactions, is possible [29, 34]. This can be exploited to produce graphene with a near-limitless variety of different functionalizations [29, 34-37]. One example, a fullerene functionalized graphene sheet, is shown in Figure 2.2. These functionalizations can serve a number of purposes including changing the dispersibility of the graphene in different solvents [35] and tailoring material properties [36-37].

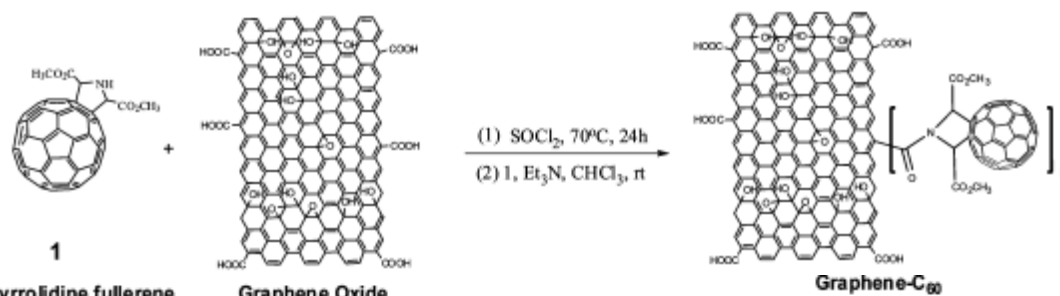


Figure 2.2: Schematic of covalent functionalization of graphene oxide by fullerene [37]

An important consequence of this bonding is the ability of graphene to form graphene platelets and graphene oxide platelets (GOP). These are several layered stacks of graphene [38] or graphene oxide [39] (also called sheets, nano-sheets, flakes, or nano-flakes). As an intermediate between atomic-scale single layer graphene and macro-scale bulk graphite, GPL and GOP offer the benefits of both. Platelets maintain the high aspect ratio of the single layer form, as seen in Figure 2.3, as well as the high thermal conductivity [33, 40-41]. The multilayered nature of the platelets introduces the possibility of interlayer sliding within the platelet, adding to the lubrication potential of the material. This was demonstrated by Feng *et al.* [42], who termed the behavior superlubric sliding, after observing the behavior of graphene when displaced *via* a scanning tunneling microscopy tip.

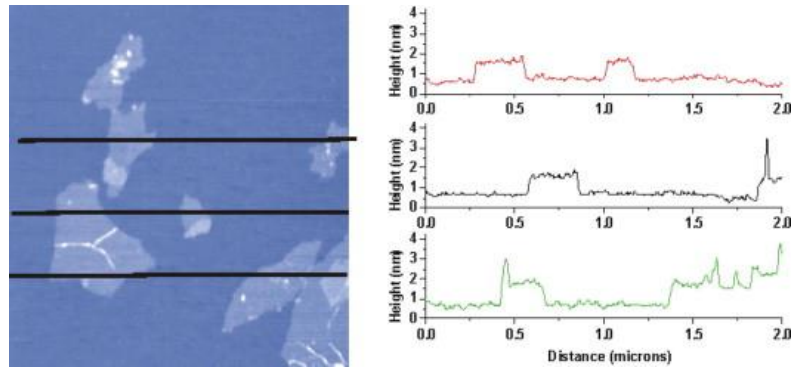


Figure 2.3: A non-contact AFM image of exfoliated graphene oxide sheets with three height profiles acquired in different locations [43]

2.1.2 Fabrication Routes

The fabrication methods for graphene and graphene platelet production have evolved continuously since the original peeling method of Geim and Novoselov [28]. Bulk graphene, GPL, and GOP can now be fabricated through various chemical and mechanical methods. In the creation of free-standing graphene, GPL, and GOP, the majority of fabrication pathways involve the oxidation of the bulk graphite precursor into graphite oxide, followed by subsequent exfoliation, as shown in Figure 2.4. The oxidation step widens the interlayer spacing between the layers in the graphite, thereby lowering their interaction energy [44]. The appropriate addition of exfoliation energy can then be used to separate the layers and to split the graphite oxide into platelets.

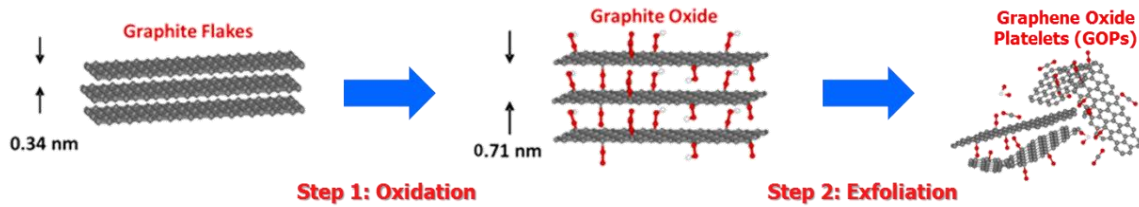


Figure 2.4: Schematic representation of graphene oxide platelet fabrication. Adapted from [45]

Methods of producing graphite oxide (GO) from graphite have been in-use since the mid-1800s. Two of the most common methods are the modified Hummer's (MH) method and the Staudenmaier method. In the MH method [46], the oxidation is accomplished by mixing sulfuric acid, graphite, and sodium nitrate under constant stirring in a 46mL:2g:1g ratio. After 1 hour, potassium permanganate, at 3 grams per gram of graphite, is added gradually to keep the temperature below 20°C. This resulting mixture is stirred for 12 hours at 35°C before dilution with water. Following this,

treatments with peroxide, hydrochloric acid, and water are conducted to isolate the GO flakes. Filtration or centrifugation along with drying can also be performed to obtain the platelets in dry form. In the Staudenmaier technique [45], nitric acid, sulfuric acid, potassium chlorate, and graphite are mixed at a 9mL:17.5mL:11g:1g ratio. When the reaction is complete, the mixture is diluted in water and washed with hydrochloric acid. Again filtration, centrifugation, and drying can then be used to obtain dry flakes. Poh *et al.* [46] found that the method of oxidation can have a profound effect on the graphene resulting from these different preparation methods.

Schniepp *et al.* [48] described a method for exfoliating graphite oxide into graphene flakes. This involves the rapid heating of the GO at a rate of $> 2000^{\circ}\text{C}/\text{min}$ to a temperature of 1050°C , leading to a 500-1000x increase in volume. Their experimental and computational analyses indicate the formation of carbon dioxide gas in the interlayer spacing of the graphite oxide. The rapid heating causes expansion of the gas which provides the pressure needed to counteract the vdW binding energy, thereby resulting in exfoliation. This mechanism is illustrated in Figure 2.5.

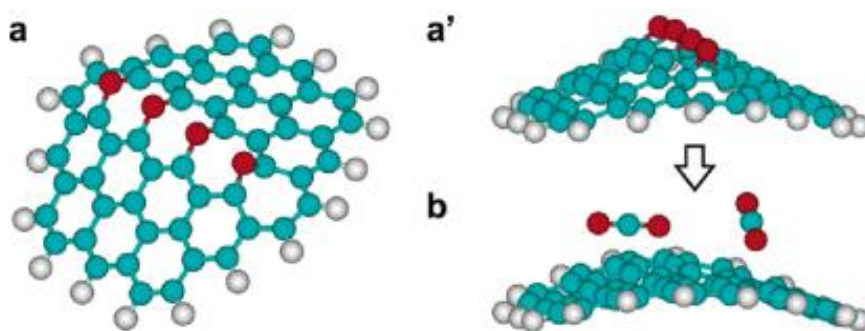


Figure 2.5: Atomistic model of the graphite oxide to graphene transition. (a, a') During oxidization of graphite, linear clusters of epoxy groups are formed through cooperative binding that lead to a bent sheet. **(b)** Carbon dioxide is released during thermal treatment [48]

Stankovich *et al.* [43] proposed a GOP fabrication process involving the chemical reduction of GO. In their method, the GO was dispersed and sonicated in DI water at 1g/L. Hydrazine hydrate was added to the mixture and the resulting solution heated at 100°C for 24 hours. The reduced graphene precipitated from the solution in solid form, which can then be isolated by filtration. It was hypothesized that the reduction of the oxygen moieties on the graphite oxide by the hydrazine reduces the hydrophilicity of the GO by removing these surface moieties. Eventually, this results in aggregation and

precipitation of graphene. A review of other chemical methods for fabrication of graphene is given in Park and Ruoff [16].

Hernandez *et al.* [49] demonstrated a technique for the in-solution production of graphene. Here, they begin with a dispersion of graphite in N-methylpyrrolidone, an organic solvent. In this solvent, bath ultrasonication is enough to provide exfoliation due to the interaction between the graphite and solvent. Others have obtained similar results using techniques such as nonionic surfactants in water, illustrated in Figure 2.6 (Notley *et al.* [50]).

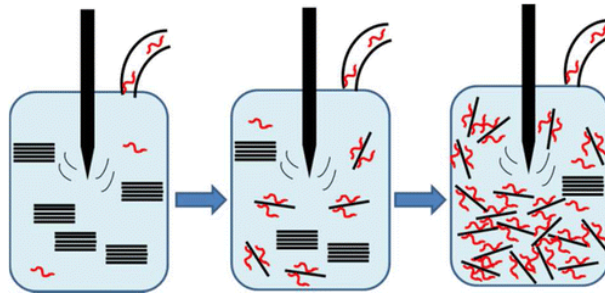


Figure 2.6: Schematic of ultrasonically assisted exfoliation aided by surfactant [50]

2.1.3 Applications Relevant to Machining

Bulk graphite has long been used as a solid lubricant in machining and tribological applications. The addition of graphite to macro-scale processes such as grinding [51], turning [52], and milling [53] lead to improvements in responses such as the cutting forces, cutting temperatures, and finished part quality. However, Marcon *et al.* [54] found that the lubricating properties of graphite have a detrimental effect on the finished part quality and tool life on micro-scale machining processes. This was attributed to the entrapment of the graphite between the clearance face of the tool and the newly machined workpiece surface.

Alberts *et al.* [24] demonstrated the use of graphene platelets as an additive to vegetable oil delivered using minimum quantity lubrication (MQL) techniques in macro-scale ball endmilling. They concluded that the addition of GPL decreases wear and chipping at the cutting edge of the tool.

Huang *et al.* [55] compared the use of graphite nano-sheets in place of bulk graphite flakes as an additive to paraffin oil in a four-ball tribology setup. They found that both the nano-sheets and flakes were capable of improving the wear resistance, load capacity, and friction coefficient of the base oil, with the nano-sheets significantly outperforming

the bulk graphite in all regards. They also discovered a concentration dependence on the performance of both materials, with both load capacity and wear resistance optimized at $\sim 1.0 \times 10^{-2}$ wt%. This is shown in Figure 2.7. They attributed the performance enhancements to the ability of the graphite nano-sheets to easily penetrate into the rubbing interface.

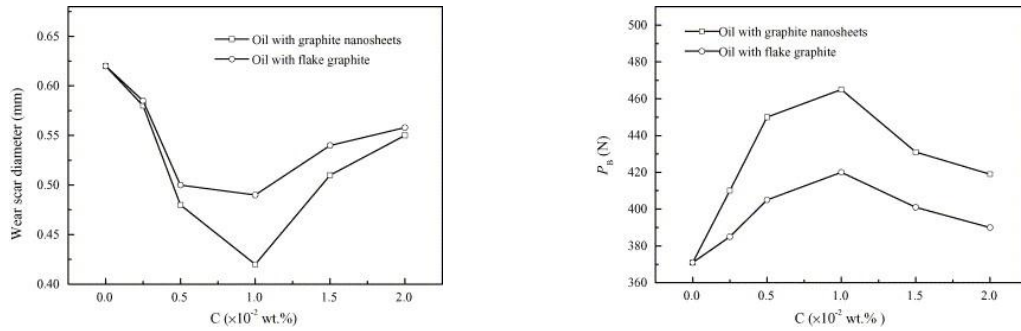


Figure 2.7: Tribological parameters of flake/nano-sheet graphite versus concentration. Four-ball, 1500 rpm, 245N, 30min. (left) Wear scar diameter (right) maximum carrying load [55]

Samuel *et al.* [56] reported the use of graphene platelets as a cutting fluid additive in micro-machining. They used thermally-reduced graphene dispersed in a semi-synthetic cutting fluid and delivered to a micro-turning setup using atomization and directed air flow. Concentrations of 0.1%, 0.2%, and 0.5% GPL by weight were used and compared to the baseline cutting fluid and carbon nanotube-laden colloidal suspensions. Cutting forces and cutting temperatures in the process were seen to decrease with increasing GPL concentration (see Figure 2.8). The GPL solutions outperformed those enhanced with carbon nanotubes. The performance of the GPL solutions was attributed to i) improved wettability that enabled effective penetration of the platelets into the cutting zone; ii) lubrication provided by interlayer sliding; and iii) the thermal conductivity of the platelets aiding their ability to act as heat sinks in the cutting zone.



Figure 2.8: Trends in cutting parameters encountered for various nano-scale additives. (a) cutting temperatures (b) cutting forces [56]

2.2 Graphene Composites

This section will review literature describing the use of graphene and graphene platelets as a reinforcement phase in composites. It will review the fabrication routes used to create these composites, the relevant material properties of the resultant composites, and their machinability.

2.2.1 Fabrication Routes

Huang *et al.* [57] and Stankovich *et al.* [58] provide an extensive review of graphene-based composites. In the past decade, graphene has been used to create composites with a large variety of other materials, including metals, oxides, chalcogenides, polymers, and biomaterials. The processing routes are equally diverse, ranging from exploiting the dynamics of π - π stacking and covalent bonding to simple mechanically-assisted mixing of graphene into polymer solutions. This review will focus on graphene-polymer and graphene-metal composites, as they are the most likely to require processing *via* machining processes.

Kuilla *et al.* [59] and Potts *et al.* [60] present a more targeted review of polymer-graphene composites. One common fabrication path is creating mixtures of GPL in non-solid phase polymer, depicted in Figure 2.9. This can be either a polymer in solvent solution or the melt phase of thermoplastic material. Once the mixtures are impregnated with GPL, they can be treated much like conventional thermoplastic or thermosetting polymers with thermoforming and vacuum forming procedures. This processing route can bypass issues of polarity that would render *in-situ* polymerization unfeasible and has been used to create graphene composites in matrices composed of materials such as epoxy, acrylic, polystyrene, etc.

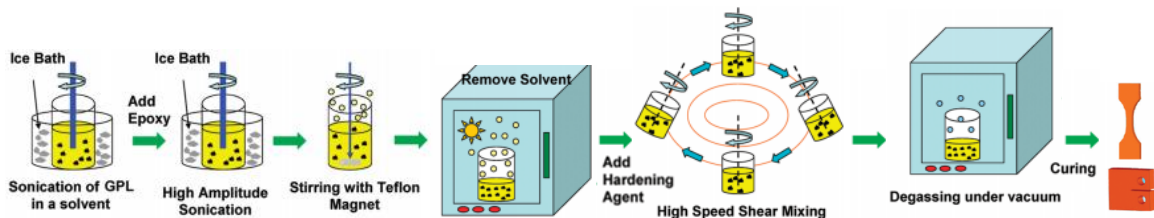


Figure 2.9: Dispersion of graphene sheets in epoxy-matrix *via* solution mixing with high amplitude ultrasonic agitation and high-speed shear mixing [61]

Another common process is the *in-situ* polymerization of monomers on the surface and interlayer space of a graphene platelet, shown in Figure 2.10. In this route, a monomer and graphene platelets are emulsified together in some solvent and the monomer is made to intercalate the graphene sheets. Then, polymerization of the monomer is induced, resulting in the composite structure. This method has been used to create composites of graphene with polymers such as polystyrene, nylon and polyaniline.

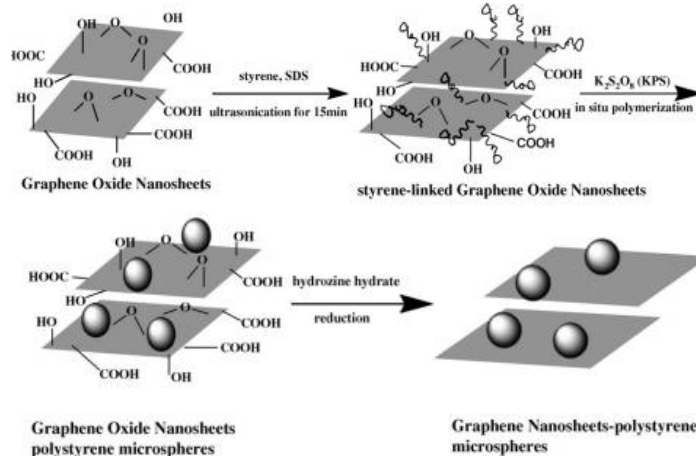


Figure 2.10: Schematic of *in-situ* formation of polystyrene-graphene nano-composite [59]

Metal matrix composites (MMC) with graphene are also beginning to be developed. Chen *et al.* [62] created a magnesium-graphene MMC. They dispersed GPL in molten magnesium prior to casting, shown in Figure 2.11(a). The cast MMC plate was then subjected to solid-state friction stir processing to remove clumping, shown in Figure 2.11(b). The addition of graphene to the Mg resulted in an ~80% increase in hardness at 1 vol%, which is superior to other typical additives such as CNT and silicon carbide.

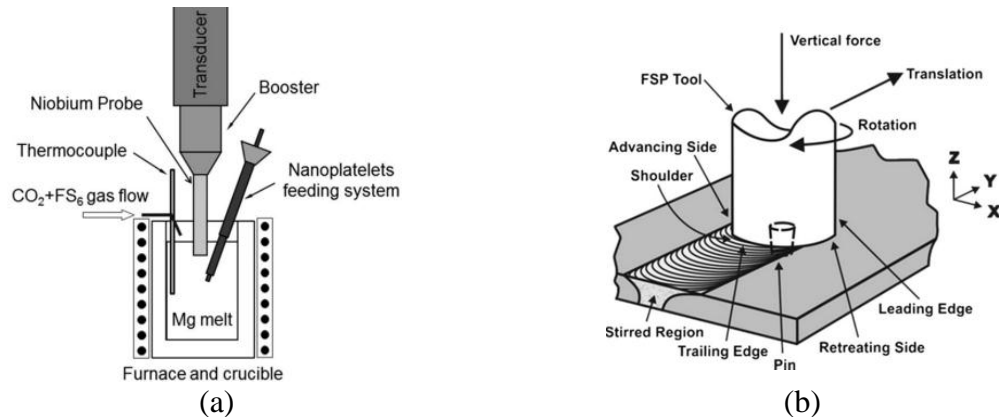


Figure 2.11: Procedure for graphene reinforcement of metal matrix. [62] (a) Dispersion of platelets into molten Mg. (b) Friction stir processing of cast plate

A vastly different technique by Wang *et al.* [63] recently demonstrated the use of polyvinyl alcohol-treatment of aluminum flakes to enable the adsorption of graphene flakes. This powder-form composite was then compacted, sintered, and extruded to produce the bulk MMC. The addition of the graphene was seen to improve strength by >60% without embrittlement.

2.2.2 Properties and Applications

M. Rafiee and N. Koratkar have examined various mechanical properties of graphene-epoxy nanocomposites such as its buckling behavior [44], strength [61], and fatigue behavior [64]. In all cases, they found significant improvements in these mechanical properties over both pure epoxy as well as carbon nanotube-enhanced epoxies, making the case for the use of these materials in structural applications. They noted a general improvement from 0.1 to 0.2 wt%, but then a decrease at 0.3 wt%, which they attributed to agglomeration of GPL.

Yavari *et al.* [22] extended this work to a hierarchical composite composed of the same GPL-enhanced epoxy matrix but with the addition of a glass fiber reinforcing phase. This composite was created using a layer-by-layer build-up method. They noticed a dramatic increase, up to three orders of magnitude, in the fatigue life of these materials over that of a plain glass fiber reinforced composite. This was attributed to a reduction in damage accumulation due to the ability of GPL to suppress interlaminar crack propagation and delamination under compressive stress, as illustrated by ultrasound analysis shown in Figure 2.12. They also identified the importance of localizing the GPL at the fiber/epoxy interface to prevent delamination and improve the overall strength of the composite.

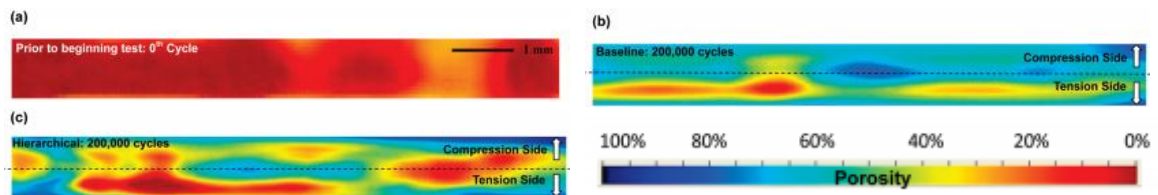


Figure 2.12: Ultrasound porosity analysis of hierarchical graphene composite after 200,000 cycles of bending at ~300MPa peak stress [22] (a) Sample prior to testing. (b) Baseline sample (c) Hierarchical composite sample

Compton *et al.* [65] investigated the use of graphene platelet composites as a barrier to the diffusion of oxygen molecules. The use of graphene (0.02 vol%) in polystyrene was found to be ~40 times more effective at limiting gas transmission than the conventional clay nanoadditives. They attributed this increase to the 2D nature of the graphene additives, creating a “tortuous path” for the O₂ molecules to traverse (Figure 2.13). This would enable the use of light-weight, gas-permeable plastics as packaging materials in applications where mitigating any degradation caused by gas is of high importance. These plastics are also effective in blocking the transmission of light.

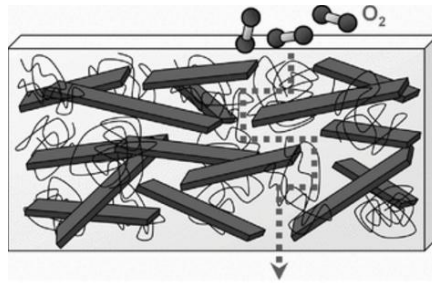


Figure 2.13: Schematic representation of O₂ molecules following a “tortuous path” [65]

Graphene composites are attractive for use as electrodes in supercapacitors and batteries. K. Zhang *et al.* [66] used graphene/polyaniline composites as supercapacitor electrodes and obtained high specific capacitances (maximum 480 F/g at a current density of 0.1A/g) and good cycling stability. Zhou *et al.* [67] used graphene-Fe₃O₄ as an anode material for lithium ion batteries. The flexible interleaved structure of this material, depicted in Figure 2.14, led to enhancements in lithium storage capacity, cyclic stability, and rate capability.

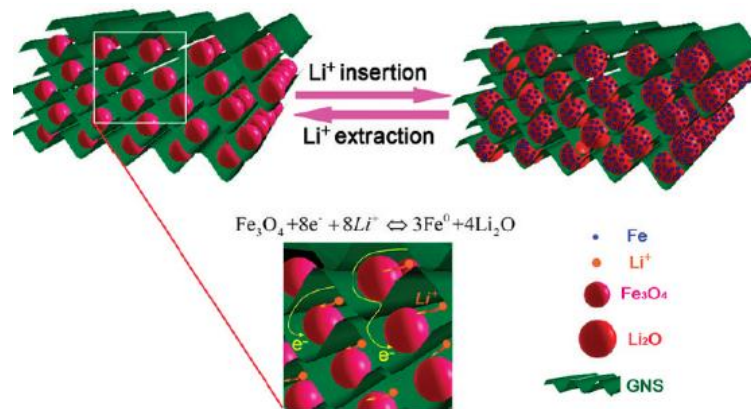


Figure 2.14: Flexible interleaved structure consisting of GNSs and Fe₃O₄ particles [67]

H. Zhang *et al.* [68] experimented with the use of chemically-bonded titanium oxide and graphene as a photocatalyst for the purification of water and air. Their experiments involving the degradation of methylene blue in visible and UV light showed a more than 2-fold increase in degradation after 10 minutes over pure TiO₂ and a significant increase over TiO₂ carbon nanotube composites. They also demonstrated increased absorptivity of the graphene composite compared to pure and CNT-TiO₂ in the absence of light, shown in Figure 2.15.

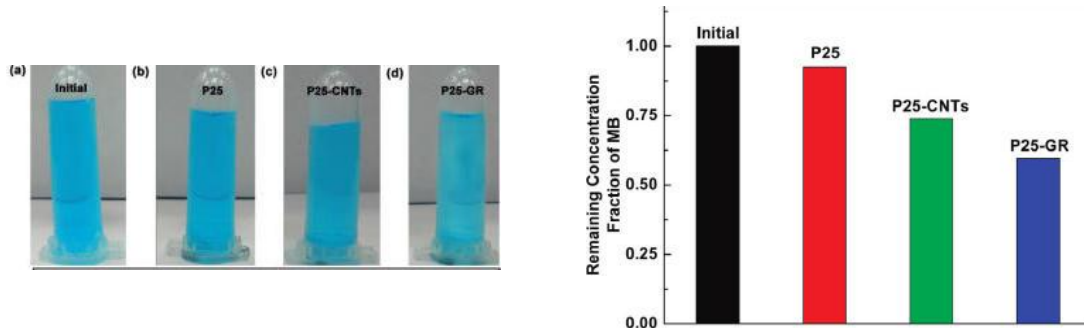


Figure 2.15: Methylene blue in solution after 10 min stirring in dark [68]

2.2.3 Machining of Graphene Composites

Arora *et al.* [21] performed micro-milling experiments on GPL-epoxy composites, similar to those used in studies by M. Rafiee and N. Koratkar. A ~400 μ m single-fluted tungsten carbide endmill with edge radius 2 μ m was used to cut composites containing 0.1%, 0.2%, and 0.3% by weight GPL. The effects of feed-per-tooth and strain rate were studied by varying these two parameters between 0.3-10 μ m and 7.5-50m/min, respectively, at a depth-of-cut of 200 μ m. They found that the GPL loading reduces minimum chip thickness, modifies the finished surface morphology, and decreases tool wear. The change in surface morphology, shown in Figure 2.16, is due to the presence of cracks and debris found in the graphene-rich zones. They also observed a nonlinear relation between the cutting forces, the concentration of GPL, and the strain rate.

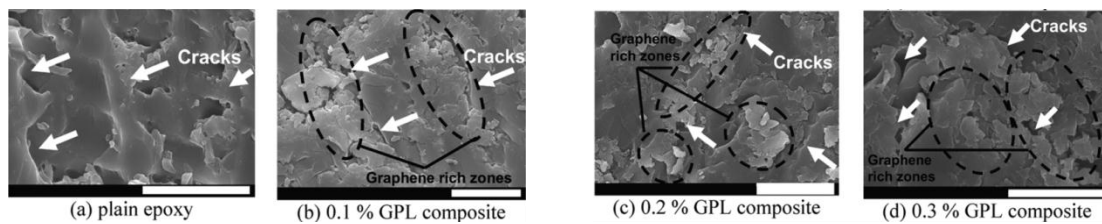


Figure 2.16: Surface morphology of machined graphene composite at feed-per-tooth of 1 μ m and cutting speed of 17m/min. [21] (scale bar = 5 μ m)

2.3 Machining Mechanics

This section will review the experimental, analytical, and computational approaches to understanding the underlying physics of machining. In the analytical and computational sections, particular attention will be paid to the challenges faced in micro-scale machining.

2.3.1 Experimental Methods

In machining experiments, the main factors of concern are the quality of the workpiece, the wear of the tool, and the power consumption, as these are of direct importance to the efficiency of the machining operation. Wear of the tool and quality of the workpiece can be determined *via* probing methods such as spectroscopy [69], or in other cases, by visual techniques such as profilometry (Figure 2.17). Power consumption can be estimated by examining the power draw of the machine tool.

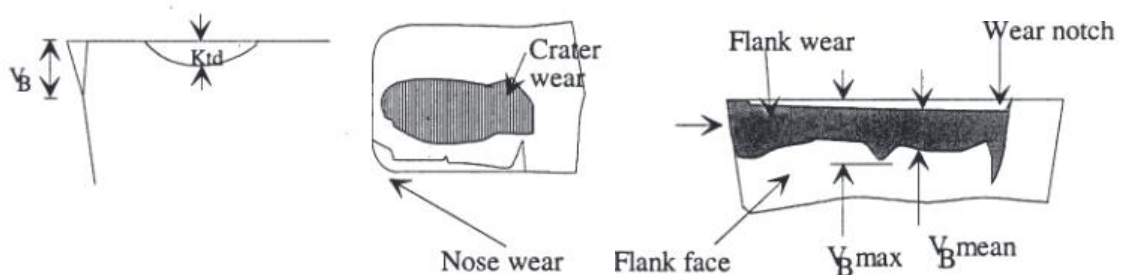


Figure 2.17: Conventional features of turning tool wear measurement [70]

However, when examining the machining mechanics in-depth, it can also be beneficial to look at the cutting temperature and cutting force as indicators of the machining efficiency. Since these metrics can be gathered continuously during cutting processes, they can be used to identify changes, such as catastrophic tool wear [70] or the formation of built-up edges [71], which cannot be identified post-process. Cutting forces are generally measured by dynamometers or load cells integrated into the machine tool. Cutting temperature measurement is more complex, and a perfect solution has yet to be found, but techniques include the use of thermocouples, pyrometry, thermography, and the use of temperature sensitive materials (Figure 2.18).

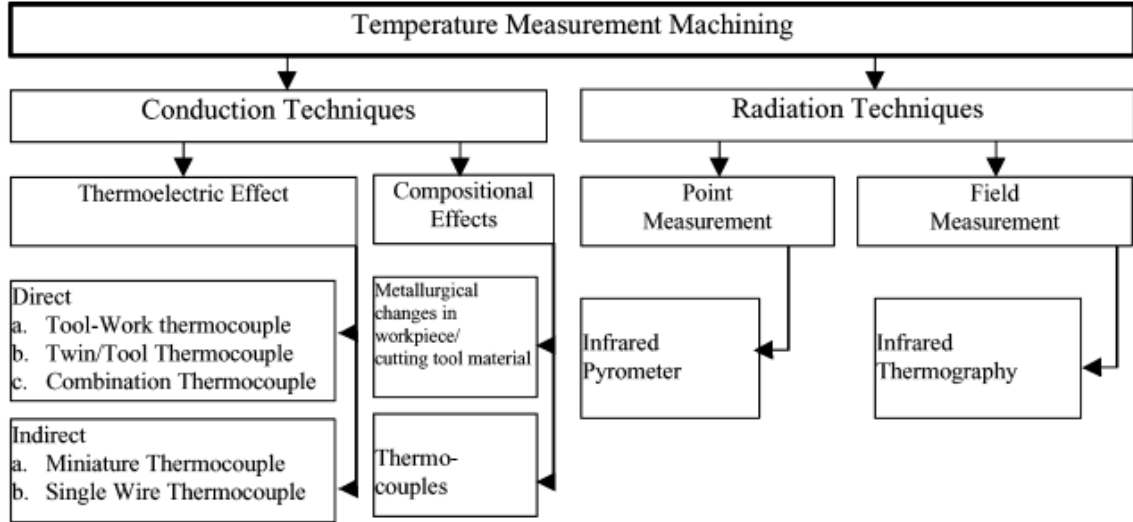


Figure 2.18: Temperature measurement in machining [72]

The techniques mentioned above have been adapted for use in micro-scale machining operations that are characterized by a number of size-scale related effects. Chief among these was the discovery of the minimum chip thickness effect by Weule *et al.* [73]. They analyzed the surface morphology of micro-features machined into SAE 1045 steel with a tungsten carbide tool and found that the surface roughness (R_{th}) is a function of the feed per tooth, f_z , the radius of the tool, r , and the minimum chip thickness, h_{min} , based on the assumed saw-tooth profile produced by springback (Figure 2.19). The minimum achievable surface roughness can be found by setting its derivative, R'_{th} , equal to zero.

$$R_{th} = \frac{f_z^2}{8r} + \frac{h_{min}}{2} \left(1 + \frac{r h_{min}}{f_z^2} \right) \quad (1)$$

$$R'_{th} = \frac{f_z}{4r} - \frac{r h_{min}^2}{f_z^3} = 0 \quad (2)$$

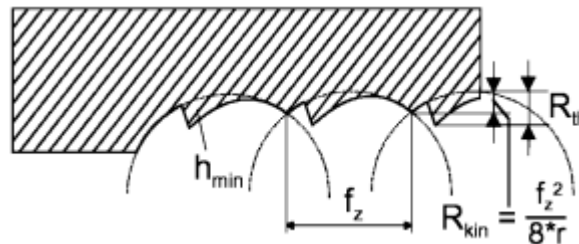


Figure 2.19: Theoretical surface profile in micro-milling, assuming that the minimum cutting depth determines the achievable surface roughness [73]

Another important aspect of micro-machining mechanics is the profound effect of microstructure on the machining outcomes. This is due to the comparable size of the material grains and the desired feature sized. To *et al.* [74] demonstrated the effect of the crystallographic orientation of aluminum on diamond turning outcomes. They found distinguishable differences in the cutting forces and surface profiles based on the difference in crystallographic plane (Figure 2.20) with the {110} plane producing the highest forces and surface roughness.

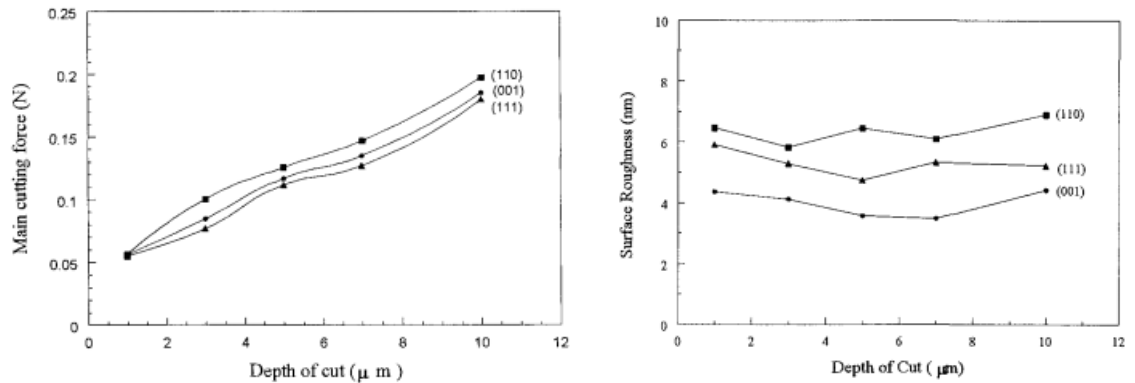


Figure 2.20: Effect of aluminum crystallographic orientation on cutting parameters. [74] (left) cutting force. (right) surface roughness

2.3.2 Analytical Models

The most well-known model of machining mechanics is the Merchant Model [75]. This model (Figure 2.21) uses the geometry of the tool and cutting parameters, in concert with the shear failure of the material and power minimization, to derive cutting forces and chip flow mechanics.

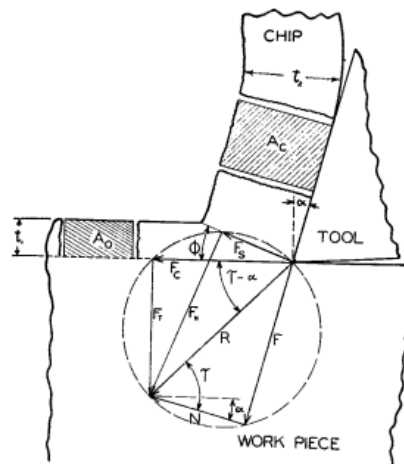


Figure 2.21: Condensed Merchant's circle diagram showing relationships between various components of the forces in machining [76]

Since its formulation in 1945, this basic model has been supplemented by different analytical, empirical, and semi-empirical extensions to account for discrepancies between the model predictions and experiments and to also capture the effects of other relevant parameters, such as the properties of the tool and workpiece materials. Other developments in this field focus on increasing the predictive power of this basic model to factors such as tool wear, surface morphology, chip morphology, temperature and stress distributions (Figure 2.22). Childs and Rowe [77] provide a detailed review of these well-established models.

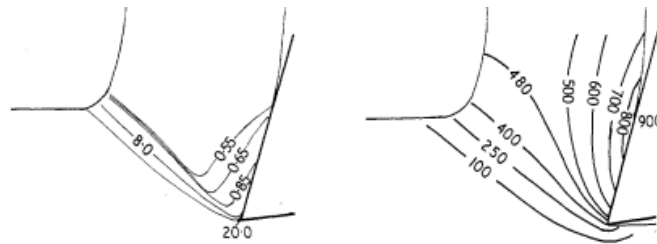


Figure 2.22: Typical distributions in continuous-chip formation. (left) shear strain rate (right) temperature [77]

The above-mentioned 2D modeling approach is also used for micro-machining. Bissacco *et al.* [78] demonstrated a close agreement between their model and micro-machining results. Their approach was a modification of a model proposed by Armarego [79], which treats the rounded edge of the cutting tool as a series of discrete, straight cutting edges summed over the entire tool radius. Their correction to the Armarego model was to recalculate the cutting coefficients to account for localized differences in the chip sliding plane (Figure 2.23), and the minimum chip thickness effect.

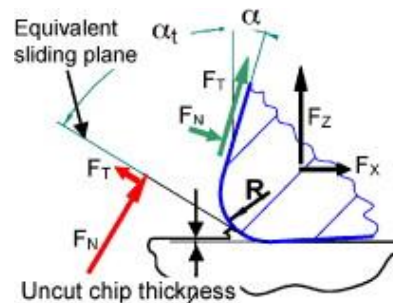


Figure 2.23: Edge radius size effect showing equivalent sliding plane and rake angle [78]

Vogler *et al.* [80] created a 3D mechanistic model to account for the effect of heterogeneous microstructure on the micro-milling of iron. To achieve this, they created a statistical model of the iron microstructure. Using this model, a simulated

microstructure was created and combined with known material properties of the constituent microstructural phases. By summing up the expected force along axial slices of the tool as it is engaged in different parts of the microstructure, the cutting force on the tool can be predicted (Figure 2.24 inset). The model was validated by comparing these predicted forces to experimental force signatures. The simulated force spectra agreed well with the experimental data, showing peaks at locations representing the high frequency variation in the force signature caused by the spacing of the secondary microstructural phases.

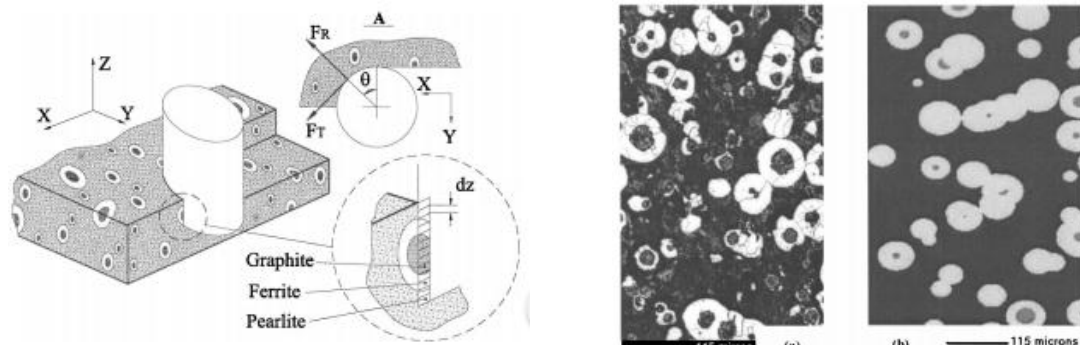
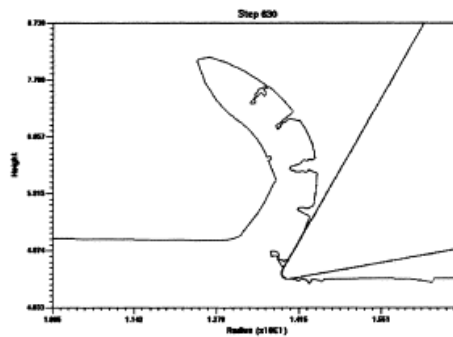


Figure 2.24: End milling of ductile iron workpiece [80] (a) Actual microstructure (b) Simulated microstructure

2.3.3 Computational Models

Many studies use finite element models (FEM) to analyze machining mechanics. The biggest obstacle to the validity of these models is defining appropriate contact, fracture criteria, and meshing routines [81]. One of the major mechanisms examined using FEM is chip formation. The model developed by Ceretti *et al.* [82] showed the influence of various cutting parameters on the formation of serrated chips. Guo *et al.* [83] used their model to examine the same with discontinuous chips.



tool travel = 6 mm

Figure 2.25: Serrated chip formation [82]

Kim *et al.* [84] used FEM to examine the temperature and stress distributions in the micro-machining of copper with diamond tools. Their analysis showed the influence of the size effect at the micro-scale. Dandekar *et al.* [85] used a 3D FEM to examine the micro-scale subsurface damage in a metal matrix composite, using cohesive zone elements to model the interface between silicon carbide additives in an aluminum matrix. This model was able to capture various forms of damage such as debonding, void formation, and particle fracture (Figure 2.26). Their modeling results agreed well with the experimental data.

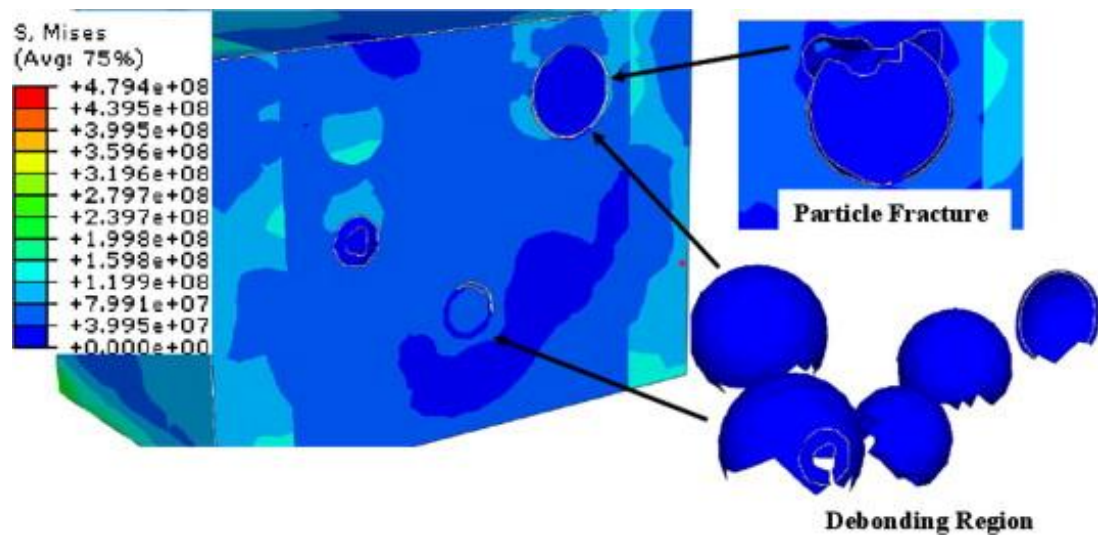


Figure 2.26: Damage observed in Al-SiC MMC using FEM [85]

Borrowing from the chemistry and materials science fields, machining researchers have recently started to use molecular dynamics techniques to study machining mechanics at the nano-scale. In MD, Newtonian physics is implemented at the molecular scale using force fields developed either from empirical data or *ab initio*. Komanduri drove much of the early developments of MD for simulating machining and his publication provides an excellent review of the field [86]. A majority of the MD simulation setups used in these studies are similar to that shown in Figure 2.27. Here, the boundary atoms are set as fixed or constant velocity, depending on whether the tool or workpiece is stationary in the chosen frame of reference. This is equivalent to a velocity boundary condition. The peripheral atoms are usually set as thermostat atoms, which are

used to remove energy from the system. These are equivalent to constant temperature boundary conditions.

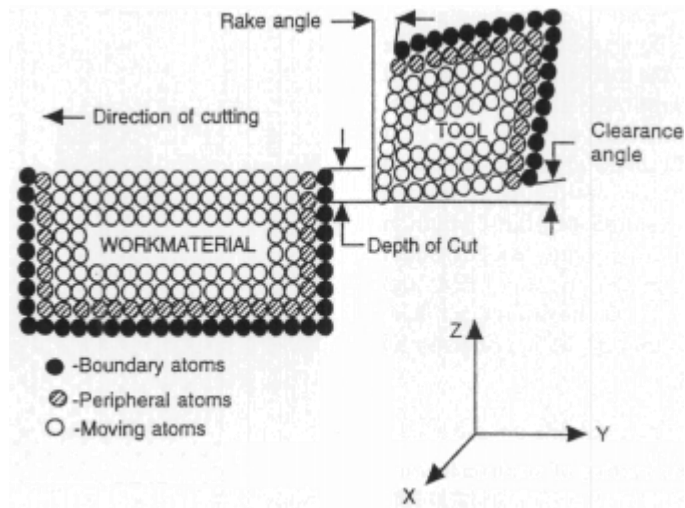


Fig. 5 Schematic of the MD simulation of nanometric cutting

Figure 2.27: Schematic of common MD setup for simulation of nanometric cutting [86]

MD techniques are very useful in simulating wear, since they can account for both chemical and physical forms of wear with the appropriate choice of potentials. Unlike in FEM, there is no arbitrarily chosen mesh to distort the results. Goel *et al.* [87] present the use of MD to examine the wear of diamond tools when machining silicon carbide. They found that high temperatures in the cutting zone lead to reduction in hardness of the tool, and then subsequent wear. As seen in Figure 2.28, they were able to determine the final location of the worn tool material by tracking the atom locations.

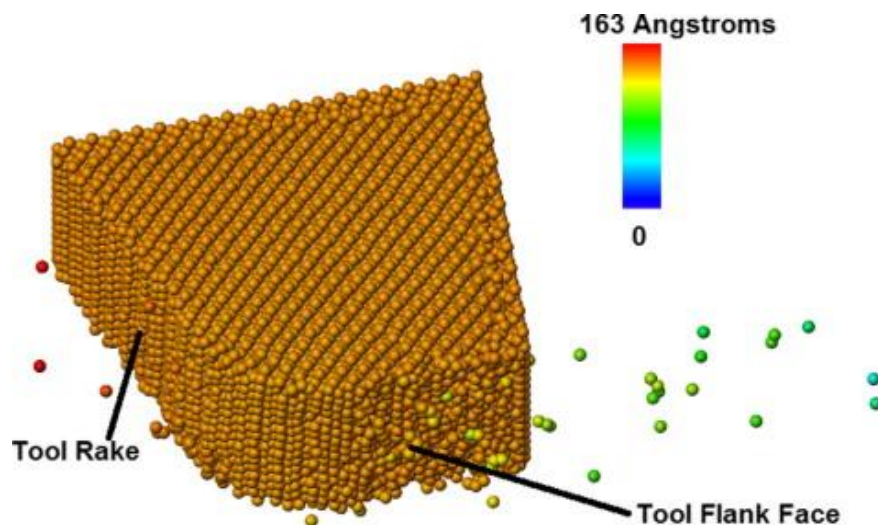


Figure 2.28: Displacement of worn atoms in MD simulated diamond tool after 10nm of cut [87]

2.4 Cutting Fluids

This section will review studies involving cutting fluids (otherwise known as metalworking fluids, metalworking oils, or cutting oils) used to provide cooling and lubrication to machining processes. This section also includes the discussion of nanofluids, i.e., fluids containing nanometer-sized dispersed particles, used as cutting fluids. The review will focus on the rheological, tribological, and chemical properties of these fluids and their effects on machining mechanics.

2.4.1 Summary of Relevant Properties

The main purpose of a cutting fluid is to provide cooling and lubrication to the cutting process, thereby reducing wear rate. For this to happen, cutting fluids must have high thermal conductivity, wettability, and kinematic viscosity in order to transport heat, spread through the entire cutting zone, and adhere to the tool and workpiece materials [88]. The main categories of cutting fluids are neat oils, water-soluble fluids, and gases [89]. There are numerous ways to apply cutting fluids including atomization (also known as minimum quantity lubrication or MQL), flood cooling *via* high pressure jet, and full-immersion (Figure 2.29).

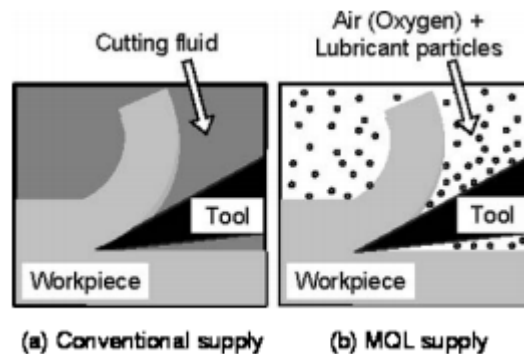


Figure 2.29: Difference between conventional and MQL application of cutting fluids [90]

One of the main concerns of cutting fluid researchers is the environmental implications of its use [91]. It is this concern that has driven the development of techniques such as minimum quantity lubrication and the use of environmentally-benign cutting fluids. Shashidhara *et al.* [92] presents a review of research in this regard. The work summarizes the use of vegetable oils, including soybean, canola, and sunflower, as

cutting fluids. Advantages of these fluids include high viscosity and biodegradability, while disadvantages include low stability and poor corrosion protection.

Nano-additives (often called extreme pressure additives) are used to promote the wear resistance of cutting fluids. Traditionally, these additives are molecules containing phosphorous, sulfur, or chlorine [93]. With the production of new nano-materials, different types of nanofluids have been tested for cutting applications. Shen *et al.* [94] performed an investigation in the use of Al_2O_3 and diamond nanofluids in a grinding application. They found improvements in both the G-ratio, i.e., the ratio of the material removed to the grinding wheel wear (Figure 2.30), as well as in the surface roughness values.

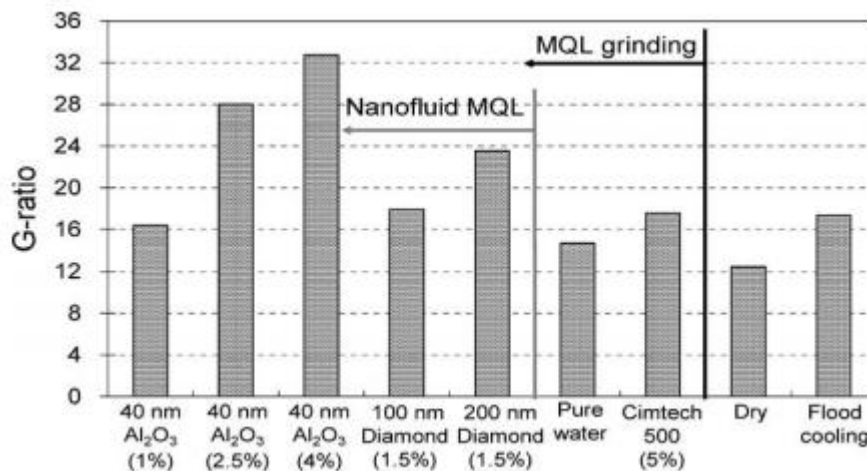


Figure 2.30: Comparison of G-ratio for various cutting fluids and nanofluids. (amount of material removed versus grinding wheel wear) [94]

Xie *et al.* [95] examined the use of alumina, CNT, and graphene nanofluids. They found that thermal conductivity varies inversely with the size of the nano-particle and suggested that the properties of the fluids could be manipulated by modifying the morphology of the additive. Buongiorno [96] conjectured that the thermal conductivity enhancement caused by nano-particles is due to the Brownian motion of the suspended particles as well as diffusiophoresis.

2.4.2 Role in Machining Mechanics

The mechanisms by which cutting fluids access the cutting zone are summarized by De Chiffre [97] and are illustrated in Figure 2.31. The cutting fluid is theorized to enter

the cutting zone through capillary action (Figure 2.31(a)), through voids connected to the formation of built-up edges (Figure 2.31(b)), through gaps caused by the vibration of the tool and workpiece (Figure 2.31(c)), and by propagation through the distorted microstructure of the chip (Figure 2.31(d)). Upon entering the cutting zone, the cutting fluid is assumed to act as a boundary lubricant, decreasing the effective friction as well as providing cooling.

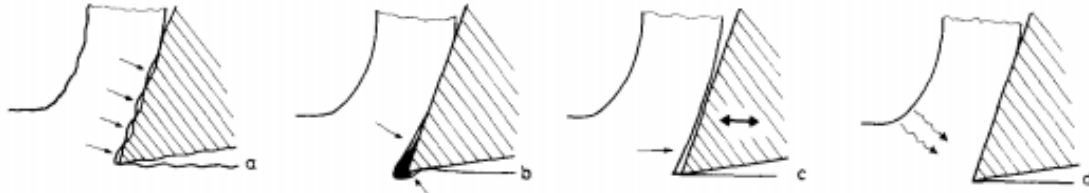


Figure 2.31: Mechanisms for cutting fluid access to rake face. [97]

Ghai *et al.* [98] investigated the droplet spreading characteristics of cutting fluids supplied by MQL impacting a rotating workpiece, similar to what was encountered during micro-turning experiments on 1018 steel. They found that the cutting temperatures have a strong dependence on the evaporation behavior of the droplets, while the cutting forces had no such dependence. Their follow-up modeling work attempted to quantify these effects more rigorously [99]. In this work, they first parameterized the shape of the droplet on the rotating cylinder (Figure 2.32) and then used this geometry to perform a heat transfer analysis, arriving at a model correlating the final shape of the droplet with surface tension, viscosity, initial droplet diameter, droplet speed, and penetration coefficient.

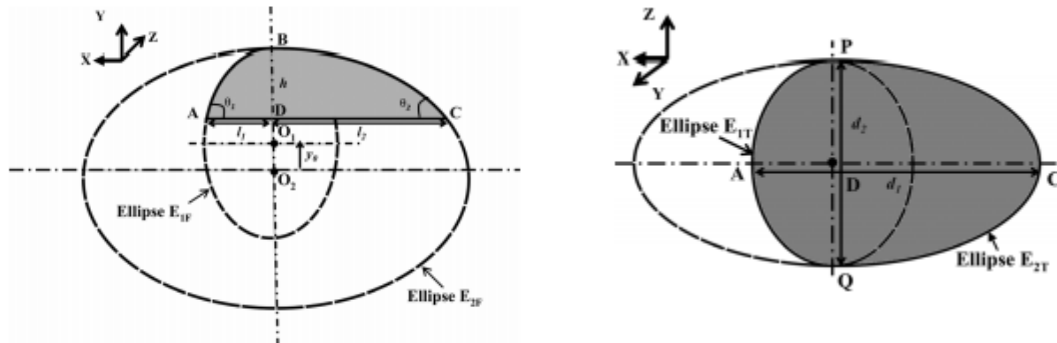


Figure 2.32: Parameterization of rotating droplet shape. (left) side-view (right) top-view [99]

2.5 Transition Metal-Catalyzed Diamond Tool Wear

This section introduces the problem of transition metal-catalyzed diamond tool wear, explaining its underlying thermodynamic and chemical basis. It will also review recent literature related to attempts to mitigate this problem.

2.5.1 Thermodynamic and Chemical Basis

The hardness of diamond makes it an attractive tool material for various machining operations [100]. This hardness, and the ability to hold an extremely sharp edge, allows diamond tools to cut under extreme conditions and create smooth surfaces. For this reason, diamond is particularly well-suited for ultra-precision machining operations involving materials such as glass [101], ceramics [102], and aluminum [103], particularly in optical applications. However, it is common knowledge that diamond tools are ill-suited for cutting transition metals and their alloys (e.g. steel) that are regularly used in engineering applications.

The reason for the accelerated wear of diamond tools when machining transition metals is two-fold. First, high temperatures and pressures encountered in the cutting zone cause spontaneous graphitization of the diamond tool. This is exacerbated by the formation of metal-carbon or metal-carbon-oxygen complexes that decrease the activation energy of the graphite diamond transformation, illustrated in Figure 2.33. These complexes are formed by interactions with the unpaired d-orbital electrons found in transition metals [104]. Since the graphitic phase of carbon is significantly softer than diamond, this transformation results in the tool rapidly losing its hardness. Thornton *et al.* [105] report several orders of magnitude more wear when this chemical wear process

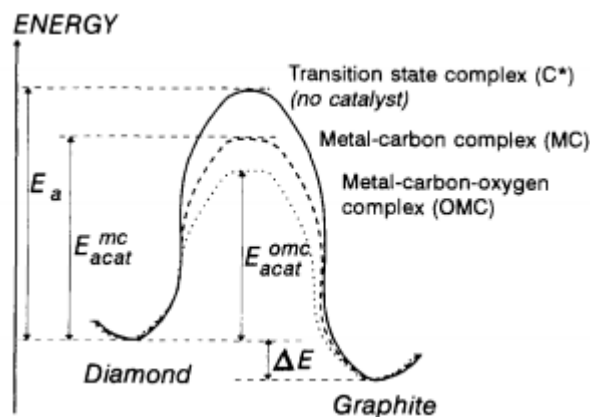


Figure 2.33: Reaction coordinate diagram of the diamond \leftrightarrow graphite transformation [104]

is active and attribute part of this to the increased reactivity of the pristine metallic layer exposed by the machining process.

The second mechanism is the transfer of carbon atoms into the workpiece by the formation of metal carbides, shown experimentally by Tanaka *et al.* [106]. Narulkar *et al.* [107] were able to show both mechanisms using MD simulations of nanometric cutting. They simulated the orthogonal cutting of an iron workpiece using a diamond tool modeled with a hybrid potential. The Fe-Fe and Fe-C interactions were handled by a modified-embedded atom method potential, while the C-C interactions were controlled by a Tersoff potential. These two mechanisms are illustrated in Figure 2.34. They found that there was a strong dependence between the crystallographic orientation of the tool and the graphitization-induced wear.

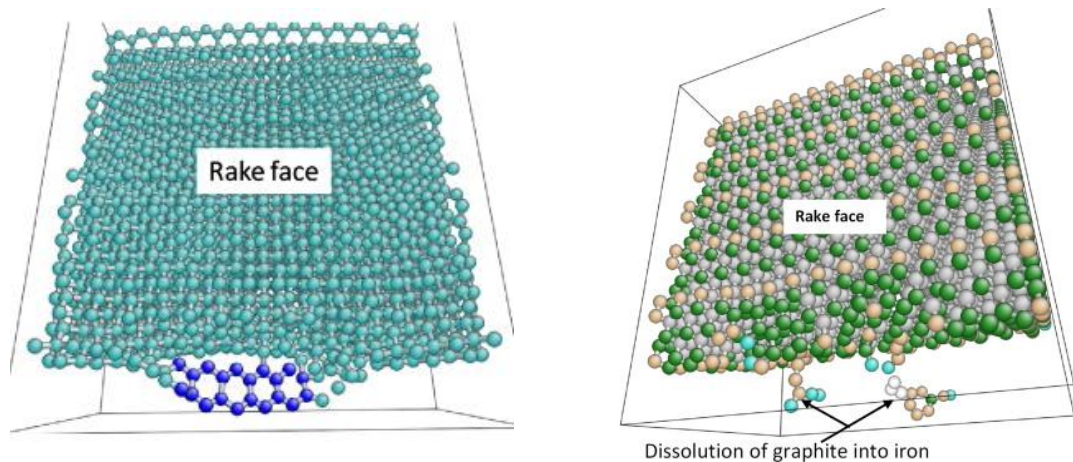


Figure 2.34: Diamond wear mechanisms simulated with molecular dynamics (left) graphitization (b) carbon diffusion [107]

2.5.2 Mitigation of Transition Metal-Catalyzed Diamond Tool Wear

Wang *et al.* [108] investigated the use of tool vibration as a method of mitigating diamond tool wear in the milling of die steel to produce mirror finished parts. The use of interrupted cutting led to a decrease in the tool wear and surface roughness. This was attributed to better heat dissipation. However, the interrupted cutting mitigates some of this improvement. They also investigated the effects of nitriding the surface of the steel (Figure 2.35). This was seen to decrease the chemical tool wear, but led to micro-chipping of the tool edge.

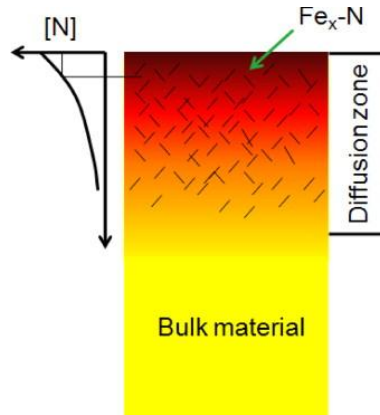


Figure 2.35: Schematic of surface nitriding of steel [108]

Evans *et al.* [109] investigated the use of cryogenic environments to reduce the rate of diamond tool graphitization. In their experiments, the baseline tool was unable to finish cutting their stainless steel annular blank due to rapid wear at room temperature. The cryogenic environment was achieved by chilling *via* thermal conduction along the shank to a temperature of 90-160K. Under the cryogenic conditions, the tool survived the entire cut and showed negligible wear when observed under optical observation at 400x magnification.

Thornton *et al.* [110] utilized inert atmospheres to prevent oxygen in the air from promoting graphitization through the formation of metal-oxygen-carbon complexes (Figure 2.33). They compared wear rates under both vacuum conditions and argon-saturated conditions. Their turning experiments showed that the wear rate in vacuum is higher than in air at low cutting speeds, but *vice versa* at high cutting speeds. The argon atmospheres, when tested, were similar to air under low cutting speeds and similar to vacuum under high cutting speeds. They concluded that some of the variation in their results was due to microstructural stochasticity in the diamond tools resulting in differing levels of atmospheric influence in the cutting zone.

Casstevens *et al.* [111] tried machining in carbon-saturated atmospheres, specifically carbon dioxide and methane. Their experiments involved turning steel specimens using mineral oil as a lubricant. In the CO₂ experiments, they observed no significant change in the wear rates. However, they noticed that the adhesion between diamond and metal was affected by the lack of oxygen. The methane atmosphere was seen to result in lower wear rates compared to machining in air.

Smith et al. [25] recently demonstrated the ability for graphene platelets to mitigate diamond tool wear. They performed micro-turning studies with GPL delivered using a semi-synthetic cutting fluid as the carrier fluid. Tool wear scans and chemical analysis of the workpiece both indicated lower amounts of graphitization and carbon diffusion when graphene platelets were present, with reductions of 32% over the baseline fluid. This reduction could not be fully explained by the cooling and lubrication provided by the cutting fluid. The authors hypothesized the mitigation mechanism to be the creation of a physical and/or chemical barrier to the graphitization and carbon diffusion phenomena, (Figure 2.36). However, these pathways are yet to be confirmed. This work is treated in more detail in Section 7.1.

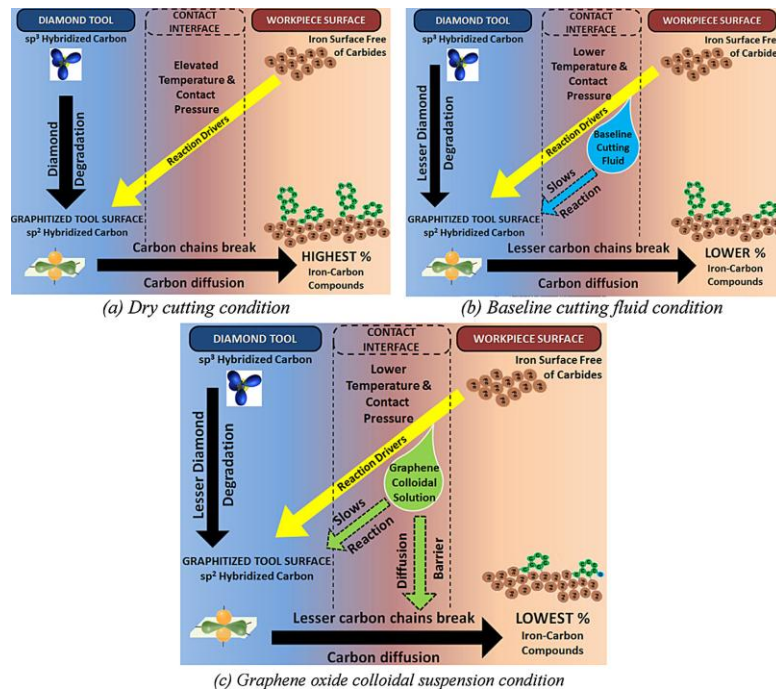


Figure 2.36: Possible chemical pathways for carbon diffusion [25]

2.6 Gaps in Knowledge and Need for Research

Based on a review of the current literature, the following gaps in knowledge can be identified with regards to the use of graphene platelets in micro-machining environments:

1. There is a huge disparity between the number of papers describing new graphene composite materials and the papers investigating its machinability. Current work has investigated the *embedded delivery* of graphene platelets

only for soft epoxy composite materials. However, there are no studies investigating its effect on harsher micro-machining environments involving carbon or glass fiber reinforcements;

2. In the case of *external delivery*, there is little understanding of the precise relationship between the physical dimensions and chemistry of the graphene platelets, the fluid and thermal properties of the colloidal suspension, and the cooling and lubrication effects seen in the cutting zone; and
3. The specific mechanisms responsible for the cooling and lubrication performance of graphene-enhanced cutting fluids in micro-machining environments are not well understood. In addition, the wear mitigation pathways encountered during diamond cutting of transition metals are currently unknown.

The research efforts presented in Chapters 3-7 aim to specifically address these gaps in knowledge.

3. EMBEDDED DELIVERY USING HIERARCHICAL GRAPHENE COMPOSITES

The research presented in this chapter deals with the embedded delivery of graphene in micro-machining environments involving hierarchical graphene composites. This composite consisted of a GPL-enhanced epoxy matrix with a glass fiber reinforcing phase. To determine the effect of the GPL enhancement on the machinability of the composite, micro-endmill slotting experiments were performed. The machining conditions were compared to cuts performed on a conventional two-phase glass fiber composite without the graphene additive. Both the cutting velocities and feed-per-tooth (FPT) values were varied to observe the effects of strain rate and chip load. Tool wear, chip morphology, cutting forces, surface roughness, and fiber-matrix debonding were used as machinability measures.

The remainder of the chapter is divided into the following sections: Section 3.1 discusses the synthesis of the three-phase hierarchical composite, its microstructure, and its mechanical properties. This is followed by Section 3.2, which summarizes the micro-milling set-up and machining conditions. Section 3.3 then shows the trends observed in the machinability measures listed above. Finally, Section 3.4 summarizes the conclusions that can be inferred from this research.

3.1 Material Synthesis and Mechanical Property Characterization

This section will discuss the manufacture of the GPL, and their subsequent integration with a glass fiber and epoxy matrix to create the hierarchical three-phase composite.

3.1.1 Graphene Platelets

The graphene platelets used to create the composite were produced using a two-step process. First, graphite flakes with an average diameter of $\sim 48 \mu\text{m}$ were oxidized in a solution of sulfuric acid, nitric acid, and potassium chlorate for 96 h [56]. The resulting graphite oxide was then subjected to a thermal shock by being placed in a furnace

This chapter previously appeared as: B. Chu, J. Samuel, and N. Koratkar, "Micromilling responses of hierarchical graphene composites," *J. Manuf. Sci. Eng.*, vol. 137, no. 1, p. 011002, Sep. 2014.

preheated to 1050° C. The rapid heating causes a pressure, which overcomes the intermolecular forces between the layers of the graphite causing it to exfoliate into platelets.

The GPL are dispersed in acetone at a ratio of 100 ml acetone per 0.1 g graphene, using an ultrasonic horn sonicator (SonicsVibracell VC 750, Sonics and Materials Inc., USA) for 1.5 h in an ice bath. Characterization of the platelets was performed by allowing a drop of the solution to evaporate on a TEM grid. The resulting TEM image in Figure 3.1(a) shows lateral dimensions of 2–3 μm and a wrinkled surface morphology that is likely to aid in strong interlocking with the epoxy matrix. Higher resolution imaging, shown in Figure 3.1(b) reveals the platelets are composed of 3–4 layers of graphene, which is corroborated by the electron diffraction pattern shown in the inset.

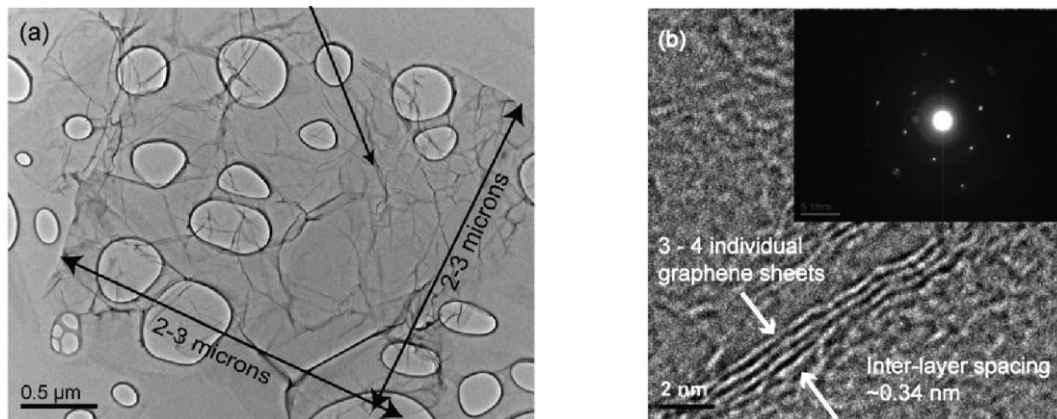


Figure 3.1: High resolution transmission electron microscopy of graphene platelets. [21, 41]. (a) Micrograph of a typical GPL flake indicating lateral dimensions in the micron range. (b) Micrograph of GPL indicating thickness of ~2nm. Inset shows the measured electron diffraction pattern

3.1.2 Hierarchical Three-Phase Composite

The hierarchical three-phase composite used in this study is primarily composed of layers of E-glass woven fabric plies (bidirectional, twill weave, Fibreglast USA, Figure 3.2(a)) held together by a matrix comprising of GPL dispersed in a bisphenol-A epoxy. The first step in making the hierarchical three-phase composite involves making a dispersion of GPL in the epoxy solution. This is followed by a layer-by-layer application of this graphene-laden epoxy to the glass fiber weave. This section describes the processing steps involved in both these stages.

To make the graphene-laden epoxy dispersion, the epoxy was first added to the acetone-graphene solution described above. The resulting solution was sonicated for an

additional 1.5h. Afterward, the bulk of the acetone was evaporated by heating the mixture on a hot plate with magnetic stirrer for 3h at 70°C. The mixture was then placed in a vacuum chamber for 12 h at 70°C to remove any remaining acetone. The resulting epoxy–graphene mixture was estimated to contain ~0.2% GPL by weight. After cooling to room temperature, a low viscosity curing agent (2120 Epoxy Hardener, Fibreglast Inc., USA) was mixed in using a high speed shear mixer (ARE-250, Thinky, Japan) for 2 min at 2000 RPM. The epoxy–graphene mixture was then placed in the vacuum oven again for 30 min to remove any mixed-in gas. Figure 3.2 (b) shows a SEM image depicting the resulting dispersion of the GPL in the epoxy matrix.

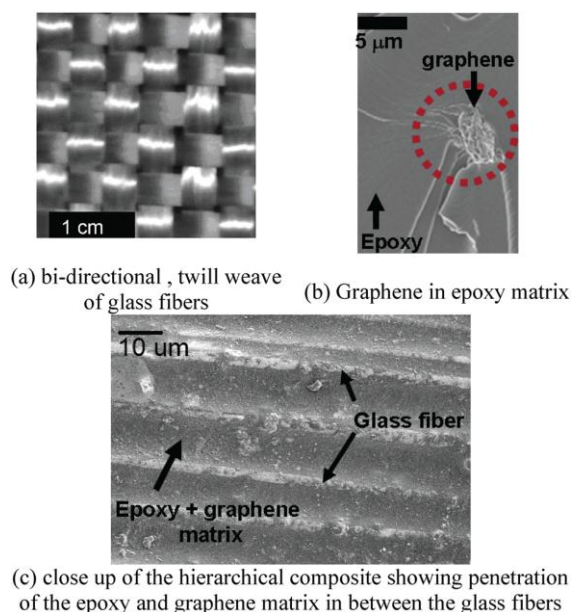


Figure 3.2: Microstructure details of the hierarchical three-phase graphene composite

To make the hierarchical three-phase composite, the graphene- laden epoxy dispersion was then applied layer-by-layer to the glass fiber plies (Figure 3.2 (a)) to make a test sample with a total of eight plies. The sample was then cured for 24 h in a vacuum bag at room temperature to ensure resin penetration. This was followed by oven curing at 90°C for 4h [22]. The volume fraction of glass fiber in the final composite is estimated to be ~0.8. The weight fraction of epoxy and graphene in the composite ply is estimated to be ~10% and ~0.02%, respectively. Figure 3.2 (c) shows a SEM image of a section of the hierarchical three-phase composite. As seen in the figure, there is a clear evidence of matrix penetration in between the glass fibers. Given the relatively larger scale of the glass fibers, it is difficult to see the presence of GPL in these images [22].

In order to establish a baseline reference, a two-phase glass-fiber-epoxy composite was also fabricated under the same manufacturing conditions. The SEM images of the two-phase composite do not show any characteristic difference from that of the hierarchical composite shown in Figure 3.2 (c), and therefore are not presented here.

3.1.3 Material Properties

The prior study of Yavari *et al.* [22] performed an extensive set of mechanical property measurements on the above two materials. Their results are briefly summarized here to ensure proper interpretation of the machining responses. Yavari *et al.* [22] tested the baseline glass fiber and epoxy composite using a three point bending test and observed it to exhibit a flexural bending strength of 520 MPa. The hierarchical composite showed an increase of 20–30% in the flexural bending strength over the baseline composite [22, 112]. In addition, the fatigue life of the hierarchical composite was seen to increase by three orders of magnitude over that of the baseline composite. Other quasi-static mechanical properties, such as the flexural modulus, tensile strength, and the elastic modulus, were observed to be unchanged [22, 112]. These trends in the mechanical properties imply that the presence of the GPL is primarily affecting the propagation of the micro-cracks within the epoxy matrix, which is expected to have a bearing on the micro-machining responses. Macroscale tensile tests appear to be insensitive to detect the effect of the presence of the GPL [64]. Table 3.1 summarizes the material properties of the composites studied in this work.

Table 3.1: Material properties of composites[22,112]

	Baseline two-phase composite	Hierarchical three-phase composite
Static Tests		
Flexural bending strength	520 MPa	670 MPa
Flexural modulus		40 GPa ^a
Tensile modulus		35 GPa ^a
Tensile strength		420 MPa ^a
Dynamic tests-cycles to failure		
Under 500 MPa bending stress	80 cycles	10 ⁴ cycles
Under 300MPa bending stress	3000 cycles	10 ⁶ cycles
Under 500MPa tensile stress	25 cycles	125 cycles
Under 300 MPa tensile stress	10 ⁵ cycles	10.3 E5 cycles

^aNo statistically significant difference seen between the two composites

3.2 Micro-milling Experiment Design

The micro-milling experiments were performed on a three-axis micro-scale computer numeric control machine tool (DT-110, Mikrottools™, Singapore). An electric NSK air bearing spindle with maximum speed of 80,000 RPM and a static runout of 1 μm was used to perform the milling tests. The samples were affixed to a Kistler 9256C1 dynamometer, to measure the cutting forces. Figure 3.3(a)-(c) show the overall experimental setup.

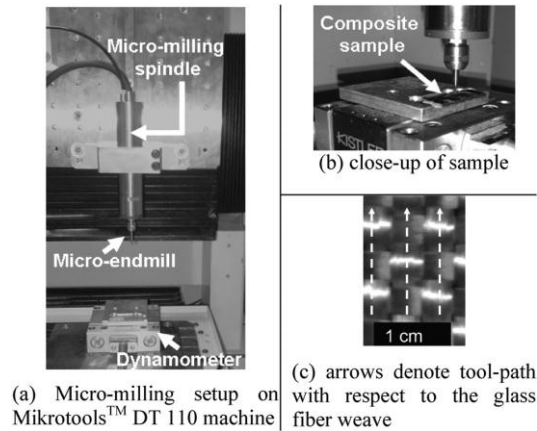


Figure 3.3: Setup for micro-milling of hierarchical composite

Micro-milling slotting tests were performed on both the hierarchical three-phase composite as well as the baseline two-phase composite. Figure 3.3(c) depicts the spacing and the direction of the slots with respect to the weave. Each slot was created using a new 508 μm diameter, two-fluted tungsten carbide endmill with an edge radius of 2 μm . The slots were 5 mm long with an axial depth-of-cut of 200 μm . The FPT was varied between 1 μm and 10 μm at cutting speeds of 30 m/min and 62 m/min. No cutting fluid was used in this study. The machining conditions are summarized in Table 3.2. It should be noted that these conditions are comparable to those used by Arora *et al.* [21] while

Table 3.2: Cutting conditions for hierarchical composite milling

Workpiece	<ul style="list-style-type: none"> • Two-phase baseline composite (glass fiber + epoxy) • Three-phase hierarchical composite (glass fiber + epoxy + graphene platelets)
Tool	<ul style="list-style-type: none"> • Size: 20 mm X 30 mm X 1 mm • 508 μm diameter, double fluted, tungsten carbide endmill with 2 μm edge radius, rake angle 3 deg., helix angle 30 deg. (Source: Performance Micro Tool TR-2-0200-S)
Cutting Speed	<ul style="list-style-type: none"> • 30 m/min, and 62 m/min
Length of cut	<ul style="list-style-type: none"> • 5mm
Depth of Cut	<ul style="list-style-type: none"> • 200 μm
Feed per Tooth	<ul style="list-style-type: none"> • 1 μm, 5 μm, 8 μm and 10 μm

studying the machinability of graphene–epoxy composites. Furthermore, the axial depth-of-cut was kept constant in this study since the work of Arora *et al.* [21] and Calzada *et al.* [113-114] revealed that increasing the axial depth-of-cut only increases the volume of material being machined and does not change the fundamental mechanisms of failure in composites.

Tool wear, chip morphology, cutting forces, surface roughness, and fiber–matrix debonding were used as the machinability measures. A Zeta 20™ optical profilometer (Zeta Instruments, USA) and a Carl Zeiss Ultra 1540 SEM were used to characterize the tool wear, chips, and surface morphology. Cutting force data was collected by sampling at 30 kHz.

3.3 Experimental Observations

3.3.1 Microtool Wear Characteristics

Figure 3.4(a)-(d) depict the SEM images of the micro-endmills that were used to machine the two materials at the cutting speed of 62 m/min. It should be noted that similar trends were also seen at the lower cutting velocity of 30 m/min. The images

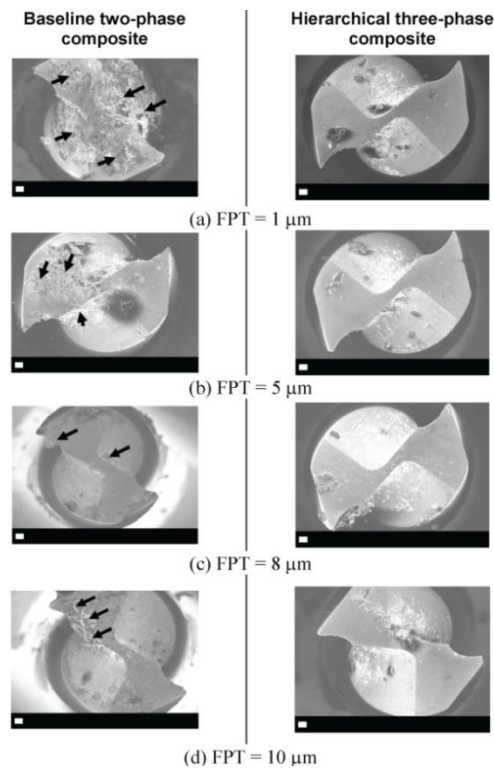


Figure 3.4: Micro-tool geometry after cutting at a velocity of 62m/min (*Note: Arrows depict epoxy debris attachments, Scale bar = 20μm*)

reveal that for the baseline glass fiber-epoxy composite one observes significant adherence of the epoxy to the cutting tool (indicated by arrows in Figure 3.4(a)-(d)). This is particularly more prominent at low FPT values of 1 and 5 μm . The hierarchical composite shows little to no adherence of the matrix phase to the micro-tool. Figure 3.5(a)-(b) depict a close-up of the rake face of the tools depicted in Figure 3.4(a). The 2D wear area of the tools was estimated by using a digital image processing technique reported by Arora *et al.* [21]. These results reveal that on an average, the hierarchical composite shows 80% lower tool wear than the baseline composite.

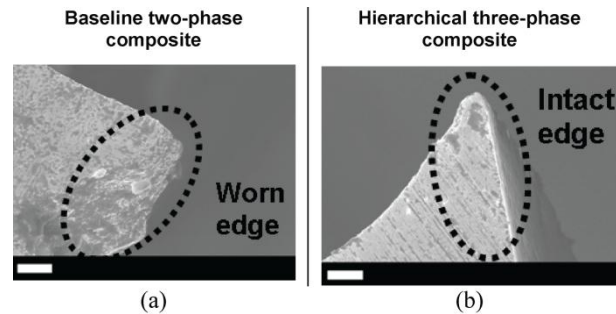


Figure 3.5: Tool wear pattern seen at a cutting velocity of 62m/min and FPT of 1 μm . (Close up of Figure 3.4(a), scale bar=10 μm)

The minimal attachment of epoxy debris and reduced tool wear seen in the case of the hierarchical composite could be explained by a combination of three mechanisms that have been reported in literature involving graphene platelets. First, the addition of GPL to the epoxy matrix has been observed to improve the thermal conductivity of the epoxy matrix [41, 115]. This implies that at lower FPT values when there is significant ploughing of the polymer phase, the hierarchical composite exhibits faster heat conduction away from the cutting zone. Prior studies by Samuel *et al.* [56], which investigated the effect of GPL as a cutting fluid additive in micro-machining, have also shown evidence supporting this heat conduction mechanism. Since plain epoxy is a poor conductor of the heat, the thermal softening of the epoxy phase is likely to be one reason for the increased debris attachment seen for the baseline composite [21, 116].

The second mechanism that could result in the observed tool wear trends is the ability of the GPL to reduce the effective coefficient of friction at the tool-chip interface [56]. The sliding between the different atomic layers of carbon within a single platelet coupled with the fact that the lateral surface area of the GPL flake is big enough to cover

the 2 μm edge radius of the tool is expected to result in reduced tool wear. While most of the tool wear is likely caused by the interaction of the tool with the glass fibers, the presence of these platelets in the cutting zone is seen to make a significant difference (Figure 3.5(a)-(b)). The third mechanism is the effect of the GPL on the failure patterns seen both in the epoxy and the glass fibers. In prior studies, the presence of GPL in the epoxy matrix has been observed to act as stress concentrations that allow for failure of the epoxy matrix along the location of GPL clusters [21]. Furthermore, as seen from the images of the chip morphology and the subsequent discussion in Sub-section 4.2, the glass fibers are seen to primarily fail in the bending mode for the baseline composite and in the shearing mode for the hierarchical composite. Since the shearing mode of failure for the glass fiber requires a lower force than that needed in the bending mode [117-118], tool wear is observed to be lower for the hierarchical composite.

3.3.2 Chip Morphology

Chip morphology is a measure that provides significant insights into the mechanism of material failure during machining [113-114]. Since the composites in this study have a 0-900 weave pattern, during a single revolution of the end-mill the cutting edge encounters glass fibers at various orientations between 0 to 180 degrees with respect to the direction of the cutting velocity vector. Furthermore, since the chip load is also varying during a single revolution, this would imply that these glass fibers that are encountered at different orientations are also being machined with varying chiploads. Given this reality, the chip morphology is expected to show effects of both varying FPT and varying glass fiber orientations in a single cut and therefore should be carefully interpreted. Since the maximum chip load seen in a single revolution does not exceed the programmed FPT, the length of the resulting glass fibers and their failure surfaces can be used as an indicator of the failure modes in the material.

Figure 3.6(a)-(h) depict the characteristic chips that are obtained at the various FPT values while machining with a cutting velocity of 30 m/min. Figure 3.7(a)-(h) provide a close up of the fractured surface of the glass fibers seen in Figure 3.6(a)-(h). These two figures when analyzed in-conjunction provides insight into the difference in the failure mechanisms that come into play between the two materials. It should be noted here that

the presence of GPL in hierarchical composite could not be imaged using the SEM given the lack of contrast that existed between the GPL and the epoxy matrix [22, 112]. However, the effects of its presence can be clearly discerned by observing the differences in Figure 3.6-Figure 3.7.

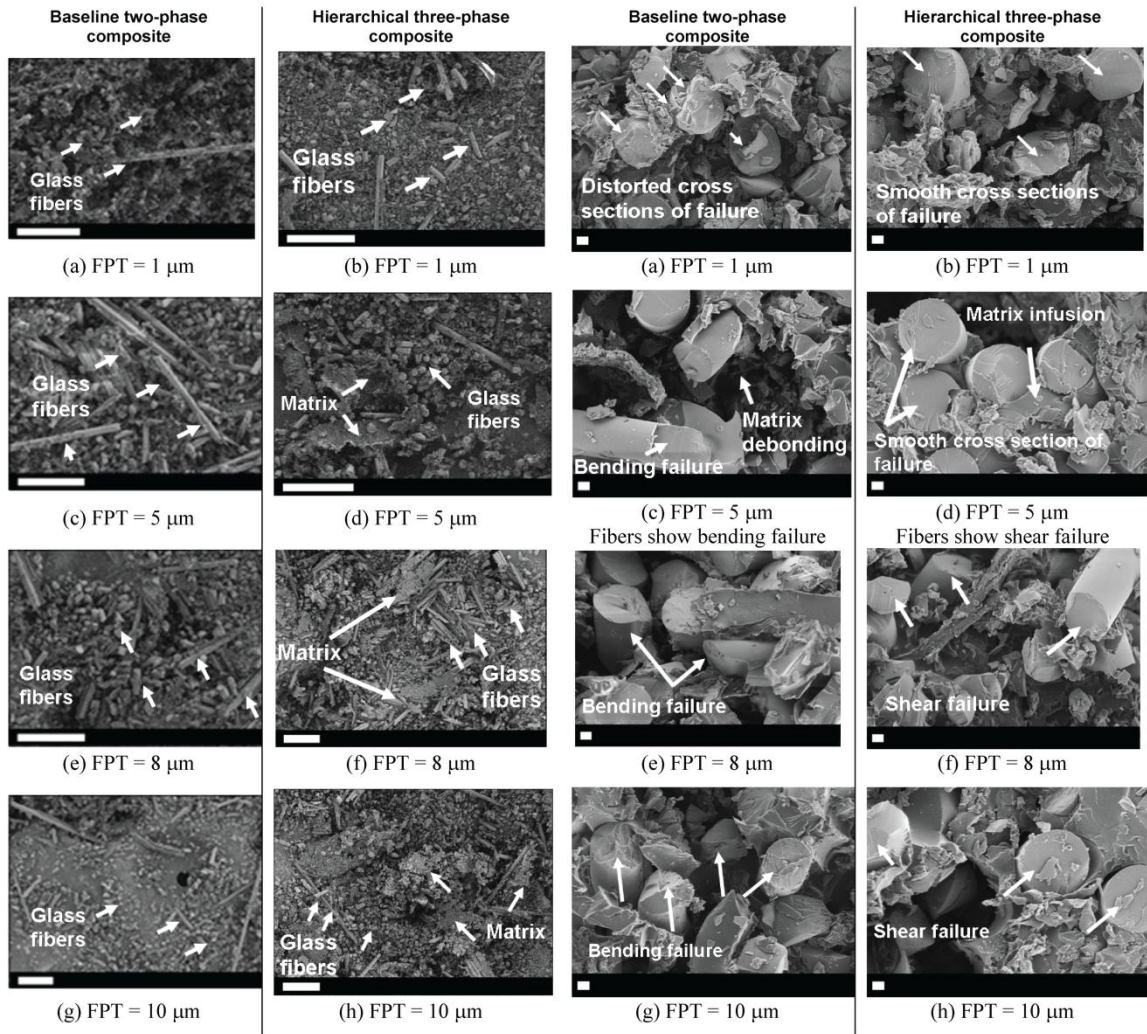


Figure 3.6: Morphology of the chips collected at cutting velocity 30m/min for various FPT values.(Scale Bar = 100μm)

Figure 3.7: Close-up of Figure 3.6 showing fiber failure modes at a cutting velocity of 30m/min for various FPT values.(Scale bar = 2μm)

As expected, the chips in Figure 3.6(a)-(h) primarily show the presence of failed glass fibers held together by a small amount of matrix. At all the FPTs tested, the chips formed for the hierarchical composite show a relatively higher percentage of the matrix holding the glass fibers together than what is seen for the baseline composite (Figure 3.6(b),(d),(f),(h)). This is likely because the presence of graphene in the matrix allows

for better adhesion of the matrix to the glass fibers. In fact this adhesion has been suggested to be the reason for the improved mechanical properties of the hierarchical composite [22, 112]. Similar evidence has been found in other hierarchical composites that have shown carbon nanotube additives improving the interfacial bonding between the glass fibers and the epoxy [119]. Figure 3.7(a)-(h) show further evidence of this being the case, in that the hierarchical composite shows an overall greater encapsulation of the failed glass fibers by the surrounding matrix.

The length and the failure pattern of the glass fibers seen in the chips formed at various FPT values reveal interesting differences between the mechanisms of failure in the two materials. The diameter of the glass fibers is $\sim 6-8 \mu\text{m}$, therefore while machining at $\text{FPT} < 5 \mu\text{m}$, the chiploads are smaller than the diameter of the glass fibers. While machining at a FPT of $1 \mu\text{m}$ (Figure 3.6(a)-(b)), which is significantly smaller than the fiber diameter, it is likely that the tool is crushing the fibers [113-114]. For most part these chips are comprised of crushed glass fibers that are held together by the polymer matrix. On an average, the size scale of these crushed fragments is comparable to the chip load values (Figure 3.7(a)-(b)). As seen in Figure 3.6(a)-(b), there are occasionally some fibers that are extremely long compared to the FPT tested. Those longer fibers are likely from the fibers oriented at 0° , 90° , or 180° to the cutting velocity [120-121].

At a FPT of $5 \mu\text{m}$, the chip load is more or less comparable to the diameter of the glass fiber. Figure 3.6(c)-(d) reveal that at a chip load of $5 \mu\text{m}$, the longest fiber length seen in the chips is $\sim 100 \mu\text{m}$ and $\sim 10 \mu\text{m}$, respectively, for the baseline and the hierarchical composite. In fact, this trend where the baseline composite shows significantly longer fiber failure lengths as compared to the hierarchical composite appears to continue even at FPT values of 8 and $10 \mu\text{m}$ (Figure 3.6(e)-(h)).

In addition to the differences in the failure lengths of the fibers, there is a noticeable difference in the cross section of the failed glass fibers seen for both the materials. In Figure 3.7(a)-(h), it is noticeable that the cross sections of the glass fibers seen for the hierarchical composite are very smooth. The surface clearly shows the onset of the failure as characterized by the wrinkled patterns, which is then followed by a smooth cleaved surface. This indicates that shear is the dominant failure mode in those fibers

[122-123]. Under the same machining conditions, the fibers for the baseline composite show a highly distorted surface (Figure 3.7(a)-(h)). The differences are most noticeable in the $1\mu\text{m}$ and $10\mu\text{m}$ FPT images where the glass fibers for the baseline composite show a very rough surface indicating that the failure mode is largely due to bending [122-123].

The difference in the length of the failed glass fibers and their modes of failure across the two materials can be explained by the concept of an “effective fiber failure length” that is a function of the fiber-matrix interface strength. Figure 3.8(a) depicts this concept for a glass fiber with a 90-degree orientation with respect to the cutting velocity. The glass fiber that is being cut can be thought of as a cantilever beam with a point load applied at its point of contact with the tool cutting edge. The effective clamping length of this cantilever beam is expected to be function of the glass fiber-matrix interface strength. For the baseline composite that has a relatively weaker interface between the matrix and the glass fiber, the application of the point load will cause de-bonding at the interface, which will in-turn lead to a larger effective clamping length for the cantilever (L_{eff} in Figure 3.8(a)). This larger clamping length results in a predominantly bending load on the glass fiber. For the hierarchical composite with a stronger interface between the matrix and the glass fiber, the effective clamping length for the cantilever will be shorter implying that the fiber will be subjected to a shear load as opposed to bending (Figure 3.8(b)).

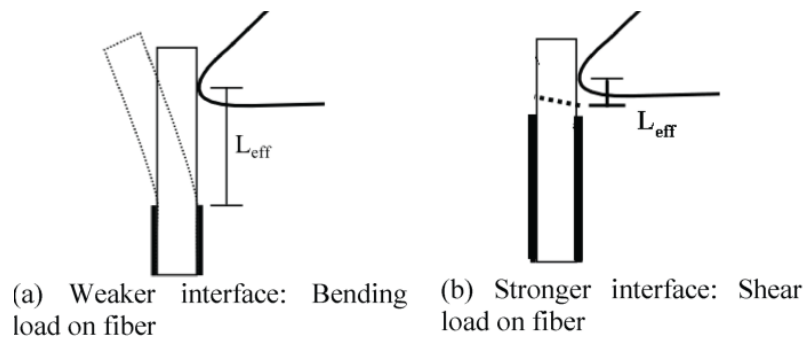
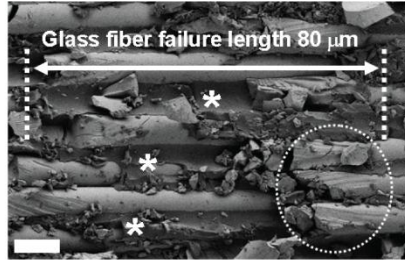


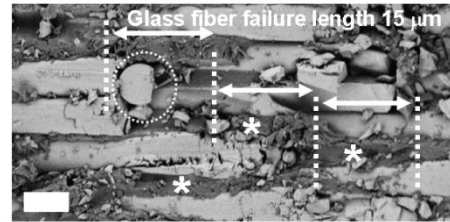
Figure 3.8: Concept of effective fiber failure length for the same depth-of-cut

The experimental evidence backing up the above hypothesis is seen on the floor of the machined slot depicted in Figure 3.9(a)-(b). As seen in Figure 3.9(a), for the baseline composite machined at a FPT of $10\mu\text{m}$, the failed glass fiber lengths are significantly larger at $\sim 80\mu\text{m}$. Furthermore the regions marked with an asterisk (*) in Figure 3.9(a)

denote the de-bonding zone where progressive failure of the fiber-matrix interface occurs. This de-bonding zone is seen to then culminate in bending failure of the fibers (circled zone in Figure 3.9(a)). The bending mode of failure is very apparent in the morphology of the failed fiber ends [122-123].



(a) Baseline two-phase composite: Locations with (*) show evidence of glass fiber-matrix de-bonding and the circled area shows evidence of bending failure of the glass fiber.



(b) Hierarchical three-phase composite: Locations with (*) show evidence of strong interface that results in shorter fiber failure lengths and the circled areas shows evidence of shear failure of the glass fiber

Figure 3.9: SEM image of the floor of the machined slots at a FPT of 10 μm and a cutting velocity of 30 m/min. (Scale bar = 10 μm)

Figure 3.9(b) shows the corresponding image of the floor of the slot machined in the hierarchical composite. As seen in Figure 3.9(b), the failed fiber areas appear to have a length of $\sim 15 \mu\text{m}$, which is very close to the 10 μm FPT value. This indicates that the effective length of failure of the glass fiber is lower. Furthermore, the regions marked with an asterisk (*) show evidence of the penetration of the graphene-laden epoxy matrix that results in a stronger fiber-matrix interface strength. The surface also shows evidence of shear-failed glass fibers that have a smooth cross section (circled zone in Figure 3.9(b)).

The failure mechanisms described above were even observed at higher cutting velocities. The increase of the cutting velocity from 30 m/min to 62 m/min did not have a noticeably different effect on the chip morphology.

3.3.3 Cutting Forces

Figure 3.10(a)-(b) depict the characteristic force signals that were picked up in the radial and tangential directions, along with their power spectrum. The spectrum shows both the spindle frequency and the tooth passing frequency. The difference in the power at the two frequencies is indicative of the run out that is present in the two-fluted tool. The peak-to-valley variation in the cutting forces was measured over every revolution.

The force variation was then averaged over the central portion of the cut, excluding the first and last millimeter and the results from those are presented in Figure 3.11(a)-(b).

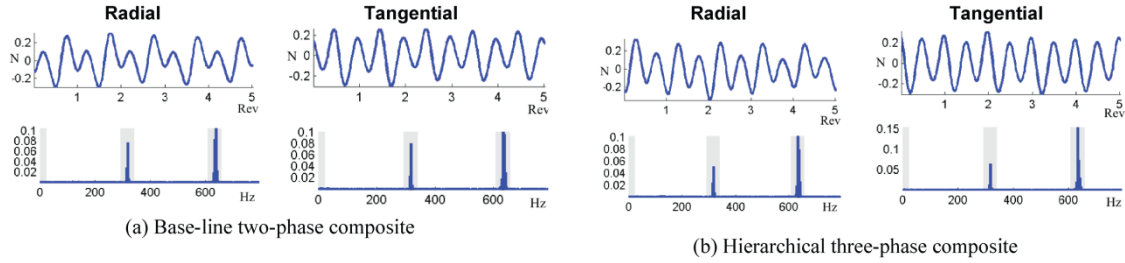


Figure 3.10: Cutting force signals and spectra in hierarchical composite milling measured at a cutting velocity of 30 m/min and FPT of 1 μm

At a cutting velocity of 30 m/min, as the FPT is increased the cutting forces are seen to increase for both the materials (Figure 3.11(a)-(b)). For that cutting velocity, the radial cutting force begins showing a difference between the two materials at a FPT value of 5 μm . The tangential cutting force does not show a noticeable difference between the two materials until a FPT value of 8 μm . In both these cases, one observes a lower cutting force for the hierarchical composite. At the higher cutting speed, this difference between the two materials is more noticeable in the radial direction.

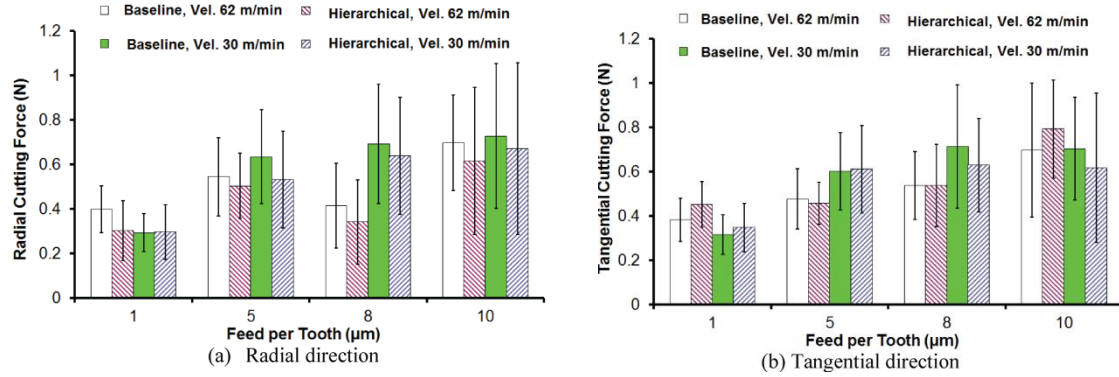


Figure 3.11: Peak-to-valley cutting forces in hierarchical composite milling

The drop in the cutting forces for the hierarchical composite is likely due to three factors. First, the tool wear and the extent of the epoxy gumming to the edge of the cutting tool is significantly lower for the hierarchical composite (refer Section 3.3.1). This ensures that the sharpness of the cutting edge is maintained for a longer duration compared to that in the case of the baseline composite, thereby lowering the cutting force. The second likely reason is that the presence of graphene reduces the coefficient of friction thereby reducing the cutting force [56, 124]. The third reason is the shorter

“effective length of fiber failure” in the hierarchical composites as explained in Section 3.3.2. This ensures that the length of the glass fibers being cut is very close to the FPT value unlike that for baseline composite where a majority of the fibers appears to have longer lengths. Furthermore, it also results in a shear-based primary mode of failure for the glass fibers in the hierarchical composite. The shear mode of failure in glass fibers requires lower forces when compared to the force needed for the bending mode in the base-line composite [117].

The cutting forces appear to show some strain rate sensitivity as the cutting velocity is increased to 62 m/min. For the baseline composite, on an average, the cutting forces appear to be lower at higher cutting speeds at all FPT values except for the FPT of 1 μm . This is because at the lowest FPT of 1 μm , the tool undergoes wear while still crushing the glass fibers severely resulting in the high cutting forces seen (Figure 3.4).

For the hierarchical composite, the component that is in the radial direction shows a drop with an increase in the cutting velocity at FPT values above 1 μm . The component in the tangential direction does not follow an obvious pattern. Looking at the trends seen in the resultant cutting force magnitudes it appears that for the base-line composite it is preferable to machine at higher cutting speeds at all FPT values, whereas for the hierarchical composites, a higher cutting speed is seen to increase the cutting forces especially while machining at FPT values higher than the critical fiber size. This behavior is likely due to the effect that graphene platelets have on the strain hardening of the epoxy matrix. Further tests are needed to critically understand this effect.

3.3.4 Surface Roughness

To measure the effect that the addition of graphene has on the finish of parts and features, the surface roughness of the bottom of the slot was measured for both the materials. Three 190 μm x 143 μm areas were imaged along the centerline of each slot using the Zeta 20TM optical profilometer and the area surface roughness (S_a) was calculated. Figure 3.12 depicts the trends seen as a function of both cutting velocity and FPT values. Irrespective of the cutting velocities used, the hierarchical composite is seen to result in the lowest surface roughness at all FPT values. Figure 3.9(a)-(b) (in Section 3.3.2) show the morphology of the machined surface. The lower surface roughness

values for the hierarchical composite are attributed to the very same factors outlined in Section 3.3.2 that result in a lower cutting force for the material. In general, an increase in cutting velocity is seen to reduce the surface roughness for both the materials.

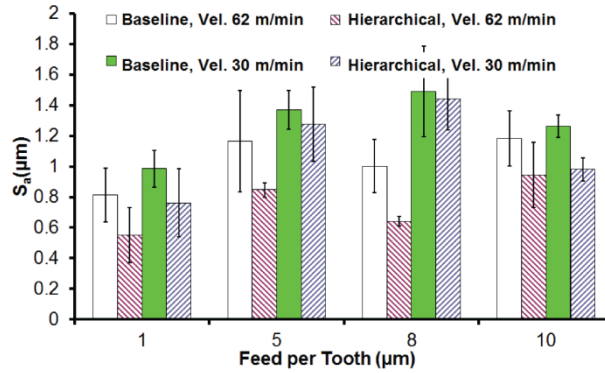


Figure 3.12: Surface roughness trends in hierarchical composite milling

3.3.5 Fiber-Matrix Debonding

Fiber-matrix debonding is a phenomenon that is commonly experienced during the machining of fiber-reinforced composites [113]. It has to do with the response of the fibers to the cutting process and its subsequent effect on the functionality of the machined part. As outlined in Calzada *et al.* [113] there are two forms of fiber-matrix debonding seen during the micro-milling of conventional fiber-reinforced composites, *viz.*, negative debonding and positive debonding. Negative debonding is when the fibers stick out along the sidewall of the slot thereby reducing the effective width of the machined slot, and positive debonding is when the fibers get pulled out, thereby leaving behind gouges that effectively increase the width of the machined slot.

The top surfaces of the micro-milled slots were scanned using the Zeta 20TM surface profiler to examine the extent of fiber-matrix debonding. Figure 3.13(a)-(h) depict the results from those scans for the slots machined at a cutting velocity of 30 m/min. It should be noted that the scans in Figure 3.13 depict the entire length of the slot and that the black dotted lines indicate the location of the sidewall of the slot, as seen in the top-view. As seen from those figures, for most part, the top surface of the slot shows negative debonding (denoted by arrows in Figure 3.13).

The evidences seen in the chip morphology and the machined surface morphology, point towards the existence of a stronger adhesion between the glass fiber and the matrix for the hierarchical composite. Therefore, one would expect the hierarchical composite

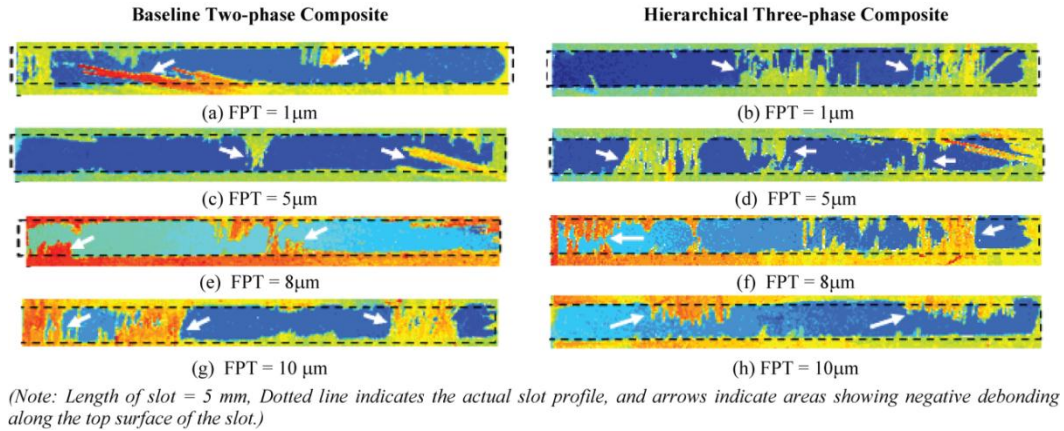


Figure 3.13: Surface scan of the top of the machined slots at a cutting velocity of 30 m/min

to show a lower extent of negative debonding when compared to the baseline composite. However, the trends seen in Figure 3.13 do not yield a clear winner between the two materials. At FPTs $< 5 \mu\text{m}$ it appears that the baseline composite has lower negative debonding, however the trend reverses at $\text{FPT} > 8 \mu\text{m}$. These trends were also seen to randomly switch between the two materials while machining at the higher cutting velocity of 62 m/min. It should be noted that the extent of negative debonding seen on the top of the slot profiles (Figure 3.13) will be strongly influenced by the sub-surface damage inflicted by the rough milling operation that is carried out prior to the slotting operation. Since the extent of this sub-surface damage is a function of the tilt that exists upon fixturing of the samples, the above scans by themselves do not offer a clear picture about the effect of GPL on the debonding trends in the composite.

To negate the effect of the sub-surface damage caused by the rough milling operation, the samples were cut to expose the side walls of the machined slots. Figure 3.14 shows an SEM image of the side-wall of the slot machined at a FPT of $1 \mu\text{m}$ and a cutting velocity of 30 m/min. The SEM characterization reveals that there is little to no

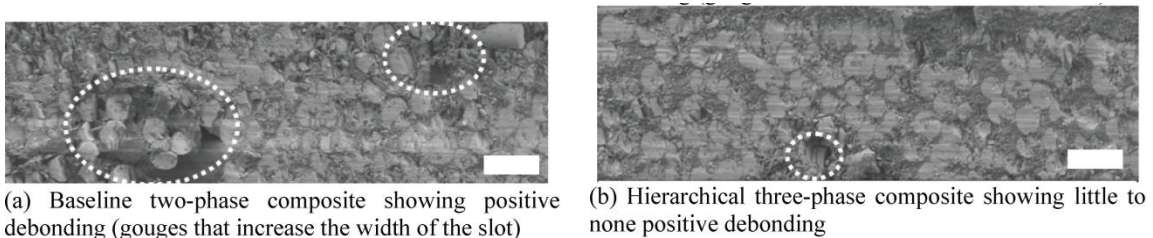


Figure 3.14: Side-wall images taken along the climb milling side of the slot machined at FPT of $1 \mu\text{m}$ at a cutting velocity of 30 m/min. (Scale bar = $10 \mu\text{m}$)

negative debonding along the side walls unlike that observed on the top surface of the slot. Instead one observes gouges (positive debonding) indicating fiber pull-out areas (Figure 3.14). In general, at all machining conditions, the hierarchical composite is seen to have a lower extent of positive debonding along the side walls, when compared to the baseline composite. This trend is similar to that predicted by the chip morphology and machined surface morphology evidences.

3.4 Summary

The following conclusions can be drawn from this study:

1. A manufacturing process for the making of hierarchical graphene composites involving glass fiber weaves and epoxy has been established. It uses the process used to manufacture graphene epoxy composites in conjunction with a hand lay-up and vacuum bagging process.
2. The micro-milling tests reveal that in general the tool wear, cutting forces and surface roughness are lower for the hierarchical graphene composite when compared to the baseline glass fiber composite thereby implying better machinability, while still improving the mechanical properties of the composite.
3. The primary mechanisms responsible for better machinability of the hierarchical composite include:
 - Graphene platelets improve the thermal conductivity of the epoxy matrix and also provide lubrication at the tool-chip interface. Both of these factors reduce the extent of polymer debris attachment on the tool and subsequent tool-wear.
 - Superior interface strength between the graphene-laden epoxy and the glass fibers allows for shorter effective lengths of failure for the glass fibers. This also results in a shear loading on the fibers in the case of the hierarchical composites as opposed to a bending load seen in the baseline composite.
4. Increase in the cutting velocity is seen to reduce the surface roughness in both materials. The cutting forces reveal that for the base-line composite it is preferable to machine at higher cutting speeds at all FPT values, whereas for the hierarchical

composites, a higher cutting speed is seen to increase the cutting forces especially while machining at FPT values higher than the critical fiber size.

5. The negative debonding trends seen on the surface of the slot are not conclusive because of the sub-surface damage caused by the rough milling operation. However, the side-walls of the slots reveal that the hierarchical composite has lower extent of debonding when compared to the base composite.

4. EXTERNAL DELIVERY USING GRAPHENE-ENHANCED ENVIRONMENTALLY-BENIGN CUTTING FLUIDS

The study presented in this chapter deals with the external delivery of graphene in micro-machining environments through the use of a graphene-enhanced, environmentally-benign cutting fluid. This first involved creating stable suspensions of graphene platelets in a plant-based oil, specifically canola oil, and then characterizing its performance as a cutting fluid in micro-machining applications. Canola oil was chosen as the base oil for this study due to its popularity as a plant-based cutting oil [6]. The GPL-laden canola oil was characterized based on its kinematic viscosity, thermal conductivity and coefficient of friction. Micro-machining tests were then performed to study the effect of GPL loading on the cutting temperature, cutting force, and the surface finish of the part.

The remainder of this chapter is organized as follows: Section 4.1, deals with the development and characterization of GPL dispersions in canola oil, followed by results from the micro-machining tests. The trends in machining responses and how they relate to the properties of the GPL dispersions are discussed in Section 4.2. Finally, the specific conclusions that can be drawn from this study are summarized in Section 4.3

4.1 Experimental Details

4.1.1 Dispersion of Graphene Platelets

In order to use graphene platelets to improve the cooling and lubricating properties of canola oil, a stable dispersion of GPL is required. The benefits of using GPL are likely to be reduced or even eliminated if the platelets are not dispersed well. The stability of graphene-based aqueous dispersions has been explored in various studies [10-12]. However, the weak bonding of the GPL with largely non-polar chains of fatty acids leads to GPL aggregation in the case of canola oil [6]. In such cases, a covalent functionalization with carboxyl groups may be preferred since the long acid chains have carboxyl groups at their ends. Such dispersion methods have been demonstrated with

This chapter previously appeared as: B. Chu, E. Singh, N. Koratkar, and J. Samuel, "Graphene-enhanced environmentally-benign cutting fluids for high-performance micro-machining applications," *J. Nanosci. Nanotechnol.*, vol. 13, no. 8, pp. 5500-5504, Aug. 2013.

carbon nanotubes CNT and microwave exfoliated graphene nano-platelets before [14-15].

The carboxyl graphene used for the dispersions was obtained from ACS Materials and was dispersed in the canola oil using a combination of horn and bath sonication. Sonication time was concentration dependent and averaged 3-4 hours. Dispersions using 0.05%, 0.10% and 0.15% concentrations by weight of carboxyl graphene were made with canola oil. Loadings greater than 0.15% by weight were not considered for this study since it was difficult to achieve homogeneous dispersions of the graphene at those high loadings using sonication techniques.

Figure 4.1(a)-(b) show the characterization of the graphene platelet by scanning electron microscopy (SEM) and X-ray photoelectron spectroscopy (XPS). The SEM image shows a flat sheet of graphene with lateral dimensions on the order of few microns. The XPS data shows clear peaks for carboxyl and hydroxyl groups.

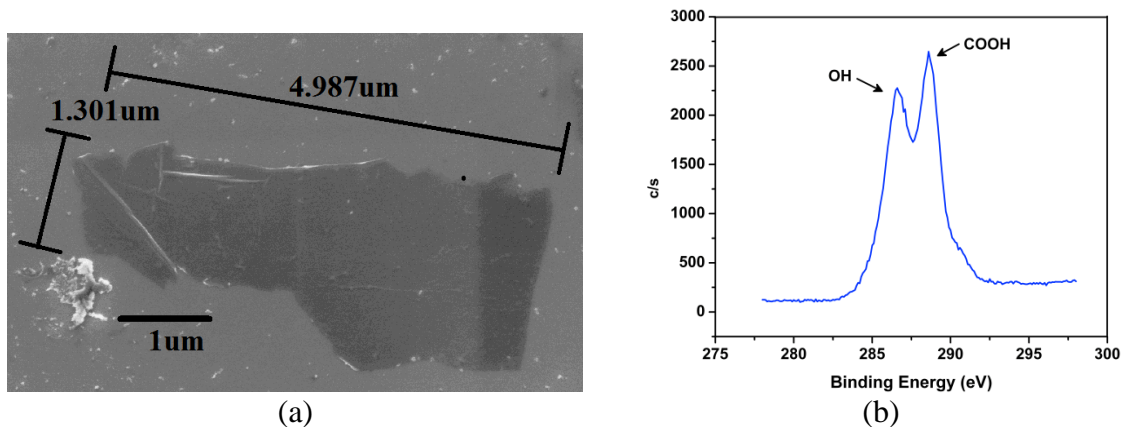


Figure 4.1: Characterization of a typical graphene platelet. (a) Scanning electron microscopy and (b) X-ray Photo-electron Spectroscopy

4.1.2 Dispersion Characteristics

The carboxyl-GPL dispersions in canola oil were characterized by measuring the coefficients of friction, thermal conductivity, and kinematic viscosity. The results from these measurements are shown in Figure 4.2(a)-(c). Friction was determined by applying a compression load of 50 lbf through two glass-filled PTFE pins and an aluminum plate attached to a universal testing machine. This arrangement was similar to the reciprocating apparatus used by Maru and Tanaka [125]. For each of the cutting oil formulations, a thin layer ($\sim 500\mu\text{L}$) of the oil was applied to the surface of the aluminum

plate before the apparatus was assembled. The aluminum plate was then reciprocally actuated, which allowed the load cell to measure the dynamic friction force.

As seen in Figure 4.2(a), the friction study shows that the addition of graphene causes the coefficient of friction to decrease significantly from that of the baseline canola oil. Pure canola oil has a 57.14% reduction when compared against a dry test. The coefficient of friction is seen to further reduce by 45.45%, 36.36% and 21.21% for the 0.05%, 0.10 % and 0.15% loadings of GPL, respectively. While the coefficient of friction of all the GPL suspensions is lower than that for the pure canola oil, an increase in GPL content is seen to increase the friction coefficient.

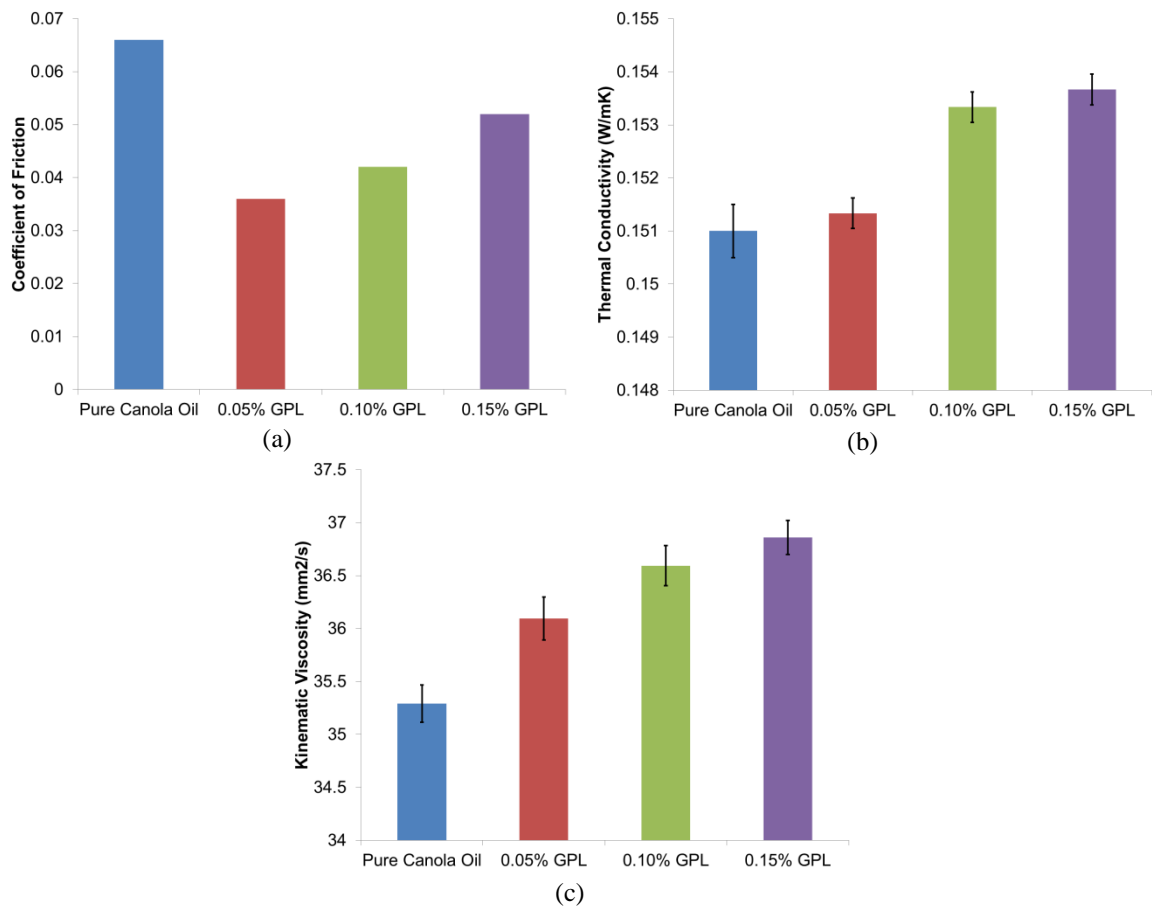


Figure 4.2: Characteristics of graphene-enhanced canola oil. (a) Coefficient of friction (b), thermal conductivity, and (c) kinematic viscosity

Thermal conductivity and kinematic viscosity were measured with a KD-2 Pro thermal conductivity probe and a Canon-Fenske routine viscometer, respectively. Thermal conductivity is also observed to increase with GPL loading. The thermal conductivity values improve by 0.66%, 1.9% and 2% for the 0.05%, 0.10 % and 0.15%

loadings of GPL, respectively. These improvements are relatively lower than the corresponding improvements seen in a semi-synthetic metal working fluid (MWF) GPL suspension [8], which indicates that the oil acts as more of a barrier to the conductive graphene. Kinematic viscosity values are seen to increase with respect to pure canola oil by 2.27%, 3.69% and 4.44% for the 0.05%, 0.10 % and 0.15% GPL loadings, respectively. This slight increase is expected and did not in any way impede the ease of application of the oil.

4.1.3 Micro-Machining Experimental Setup

In this study, the cutting fluids were tested in a micro-turning setup on a Mikrottools DT-110 CNC machine tool. This setup was used to collect the cutting temperature, cutting force and the surface finish data.

Figure 4.3 shows a schematic of the micro-turning setup used. The setup used an NSK spindle with a maximum speed of 80,000 RPM. A right-handed, cubic boron nitride, turning tool with a $\sim 400\mu\text{m}$ nose radius and $8\mu\text{m}$ edge radius was used. The workpiece was a 3mm diameter, C1018 steel, cylindrical rod. The cutting speed was held constant at $\sim 150\text{m/min}$ with a radial depth of cut of $100\mu\text{m}$ and a chip load of $10\mu\text{m/rev}$. The total length of each cut was 3mm. Cutting fluid was supplied as a constant flow through a syringe before and during the cut. Table 4.1 summarizes the experimental conditions.

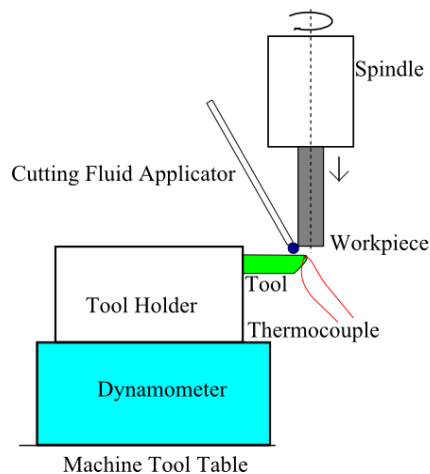


Figure 4.3: Schematic of micro-turning setup

Table 4.1: Cutting conditions for turning with graphene-enhanced canola oil

Workpiece	3mm diameter C1018 steel rod
Tool	Right handed, orthogonal, CBN tool with 8 μ m edge radius
Cutting velocity	150 m/min
Depth of cut	100 μ m
Length of cut	3 mm
Chip load	10 μ m/rev
Cutting Conditions	(1) Dry (2) Pure Canola Oil (3) .05% Graphene (4) .10% Graphene (5) .15% Graphene

Cutting forces and cutting temperatures were recorded during these tests to compare the performance of the oils. Both signals were sampled at 30 kHz. Forces were measured using a Kistler 9256C1 multi-component dynamometer and cutting temperatures were measured using a surface mounted, J-type bead thermocouple attached close to the cutting zone. A National Instruments SCXI-1112 8-Channel Thermocouple Input Module amplified the signal.

The line surface roughness (R_a) of the turned rods from the cuts detailed above was measured using a Zeta-20TM True Color 3D Optical Profiler. Ten profiles of ~950 μ m length were averaged for each condition.

4.1.4 Cutting Temperatures

Figure 4.4 shows the smoothed raw data collected from the thermocouple and the corresponding maximum temperature rise values are shown in Figure 4.4(b). The temperature rise values vary between 30°C and 85°C. The dry cut, as expected, causes a higher temperature rise in the cutting zone than any of the cuts done in the presence of the cutting oil. The data shows that with an increase in GPL loading, there is a decrease in the maximum temperature rise that is seen during the machining operation. When compared with the effect of pure canola oil alone, which causes a ~13% drop in the maximum temperature, the benefits are clear. The 0.05% loading resulted in a further ~24% decrease in temperature rise over pure canola oil, while the 0.10% and 0.15% GPL loadings resulted in decreases of ~31% and ~58% respectively.

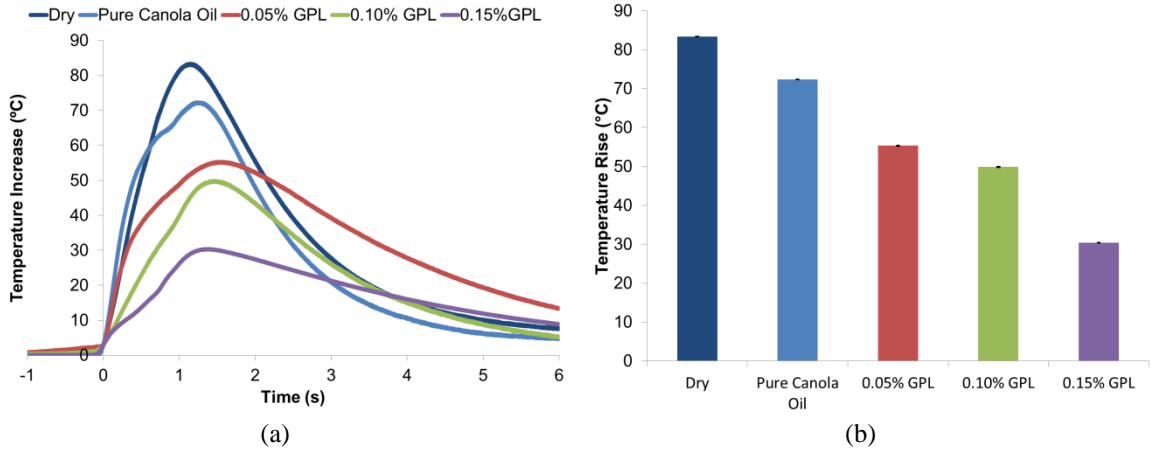


Figure 4.4: Cooling performance of graphene-enhanced canola oils (a) Temperature over time (b) Peak temperature rise

4.1.5 Cutting Forces

Figure 4.5 shows the trends in the resultant cutting force during the micro-turning experiments. The values displayed are averaged over the entire length of cut in each condition.

The use of the pure canola oil causes a force reduction of ~2.3% from the dry cut. Addition of GPL results in a further reduction in the cutting force experienced by the tool by ~6.9%, ~11.3%, and ~8.9% for the 0.05%, 0.10%, and 0.15% loadings. These reductions amount to a drop of ~8.6%, ~12.9% and ~10.5% from dry conditions, respectively for each of the three loadings. The increase in the cutting force between the 0.10% and 0.15% concentrations suggests a degradation of lubrication efficiency at higher loadings.

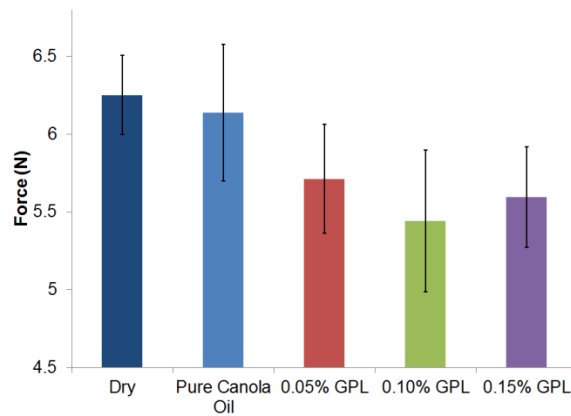


Figure 4.5: Average resultant cutting force for graphene-enhanced canola oils

4.1.6 Surface Roughness

Figure 4.6 shows the trends seen in line surface roughness values (R_a) measured on the surface of the micro-machined part. The values in the figure are averaged over ten profiles of $\sim 950\mu\text{m}$ length for each of the cutting conditions. The use of GPL additives is always seen to result in lower surface roughness values than those achieved with pure canola oil. However, increasing the GPL loading is seen to result in an increase in the surface roughness values. The observed roughness dropped $\sim 10.3\%$, $\sim 8.6\%$, and 5.9% respectively for the 0.05%, 0.10%, and 0.15% GPL solutions when compared to the results from pure canola oil. Compared to the dry cutting condition, the GPL-laden canola oil decreases the surface roughness by $\sim 13.7\%$, $\sim 12.1\%$, and $\sim 9.5\%$ respectively.

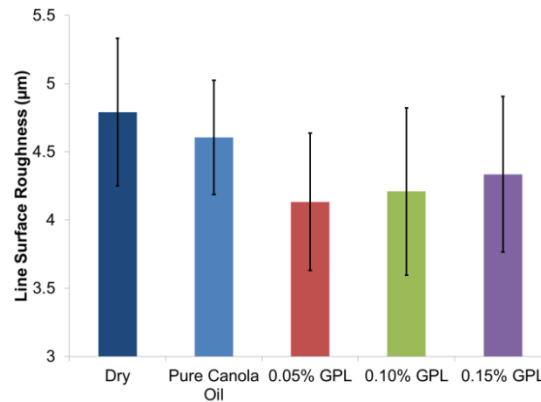


Figure 4.6: Surface roughness at slot centerline for graphene-enhanced canola oils

4.2 Results and Discussion

The addition of carboxyl GPL to canola oil is seen to result in improved performance both in terms of the cooling and lubrication efficiency of the oil, when used for micro-machining operations. This trend was also seen in the previous work with semi-synthetic MWFs [8] and can be explained by the change in the oil properties with the addition of GPL. The thermal conductivity of the oil increases in the presence of the GPL additive, which is likely to improve some of the cooling efficiency of the oil. However, in terms of percentage improvements, the thermal conductivity improvements are overshadowed by the reduction in the coefficient of friction (Figure 4.2). This suggests that the bulk of both the cooling and lubricating improvements come from the reduced rubbing friction at the tool-work interface. This is unlike the mechanism seen in

the earlier semi-synthetic MWF study where the cooling effect was predominantly caused by the evaporation of the water phase that is present in the MWF [8].

While the cutting temperatures are seen to continuously reduce with an increase in GPL loading, the cutting forces show a slight increase with the 0.15% GPL loading. It is likely that at such high concentrations there are undispersed clumps of GPL that are large enough to interfere with the cutting process, by forming built-up edges [16], and consequently cause the cutting fluid to be detrimental to the cutting process. The trends seen in the surface roughness values (R_a) appear to support this hypothesis too. While overall the GPL-laden canola oil has lower surface roughness values when compared to that of pure canola oil, the R_a values are seen to increase with an increase in GPL concentration. This could be due to the presence of GPL debris on the machined feature and/or changes in the cutting dynamics due to formation of built-up edges in the machining zone.

In general, for GPL-laded canola oils, the benefit of obtaining reduced cutting temperatures at higher GPL loadings is offset by the slight increase in both the surface roughness of the finished part and the cutting force.

4.3 Summary

This study aimed to create stable suspensions of graphene platelets in plant-based oils, specifically canola oil, and to then characterize its performance as a cutting oil for micro-machining applications. The following specific conclusions can be drawn from this study:

1. Graphene platelets are difficult to disperse in canola oil. Functionalizing the graphene with carboxyl groups increases its dispersion and allows loadings of up to 0.15% by weight to be created. Loadings $> 0.15\%$ result in visible clumps of undispersed graphene.
2. When compared to the baseline canola oil, both the thermal conductivity and the kinematic viscosity of the cutting oil increases, with increased loading of GPL.
3. The loading of 0.05% GPL results in the lowest coefficient of friction. As the GPL loading is increased further, the coefficient of friction between two surfaces is observed to increase.

4. The addition of GPL to the canola oil causes cutting forces, cutting temperatures, and surface roughness values to decrease when compared against both dry machining and the use of pure canola oil. The results were seen to hold true for all loadings of 0.05%, 0.1 % and 0.15% of GPL.
5. Cutting forces showed an increase between the 0.10% and 0.15% loadings, which is likely due to GPL clusters and/or the formation of built-up edges. This suggests that an optimal loading for lubrication exists between the tested concentrations.
6. Surface roughness increases with increased GPL content. This is caused by GPL entrapment between the tool and the workpiece.

5. EXTERNAL DELIVERY USING GRAPHENE OXIDE COLLOIDAL SUSPENSIONS AS CUTTING FLUIDS

The research presented in this chapter investigates the external delivery of graphene through the use of semi-synthetic cutting fluids. Specifically, it examines the effect of platelet geometry (i.e., lateral size and thickness) and the extent of oxygen functionalization on the cooling and lubrication performance of graphene oxide colloidal suspensions used as cutting fluids for micro-machining operations. Thermal reduction and ultrasonication techniques were used to fabricate three different types of graphene oxide platelets. The resulting graphene oxide colloidal suspensions were evaluated for their fluid properties and micro-machining performance. The results revealed that the platelet geometry and level of oxygen functionalization both influence the performance of the graphene oxide colloidal suspensions.

The remainder of this chapter is organized as follows: Section 5.1 presents the graphene oxide platelet fabrication process and the characterization of the GOP colloidal suspensions. Section 5.2 details the micro-machining experiments and the performance evaluation of these suspensions in terms of cutting temperature, cutting forces, and workpiece surface roughness. Section 5.3 discusses the micro-machining results in light of the properties of the colloidal suspensions, and finally, Section 5.4 summarizes the specific findings of this chapter.

5.1 Graphene Oxide Platelet Fabrication and Characterization

5.1.1 Graphene Oxide Platelet Fabrication

The approach taken to obtain different sized graphene oxide platelets first involved the production of graphite oxide (GO) as a precursor. The GO was subsequently exfoliated using either a thermal shock or an ultrasonication technique to produce platelets with varied lateral size, thickness, and oxygen functionalization. The thermal shock process resulted in the exfoliation of GO in a powder form, which was then

This chapter previously appeared as: B. Chu, E. Singh, J. Samuel, and N. Koratkar, "Graphene oxide colloidal suspensions as cutting fluids for micromachining—Part I: Fabrication and performance evaluation," *J. Micro Nano-Manuf.*, vol. 3, no. 4, pp. 041002–041002, Aug. 2015.

dispersed in the fluid medium of choice, whereas, the ultrasonication process resulted in direct exfoliation of the GO in the fluid medium.

Figure 5.1 shows the overall process flow for GOP production. The production of graphite oxide from raw graphite was accomplished using two oxidation techniques, *viz.*, 1) the Modified Hummer’s (MH) method [126], which produces heavily oxidized graphite, and 2) the Staudenmaier method [29], which produces lightly oxidized graphite. Figure 5.2 shows the results from the X-Ray diffraction study used to characterize the GO obtained from these two methods. The Modified Hummer’s method completely oxidizes the graphite resulting in a diffraction peak shift from the graphitic $\sim 26^\circ$ to graphite oxide at $\sim 11^\circ$, corresponding to an increase in *d-spacing* from ~ 0.34 nm to ~ 0.81 nm between the individual graphite layers [29,127]. However, with the Staudenmaier method, graphite oxide is produced with a peak observed at $\sim 13^\circ$. This indicates a lower increase in the d-spacing of ~ 0.67 nm, which in turn points to incomplete oxidation. The presence of a residual graphitic peak at 26° also confirms the milder oxidation that is achieved with the Staudenmaier method. This difference between the two types of GO plays a role in how these precursors may be further used for exfoliation to produce graphene oxide platelets [128].

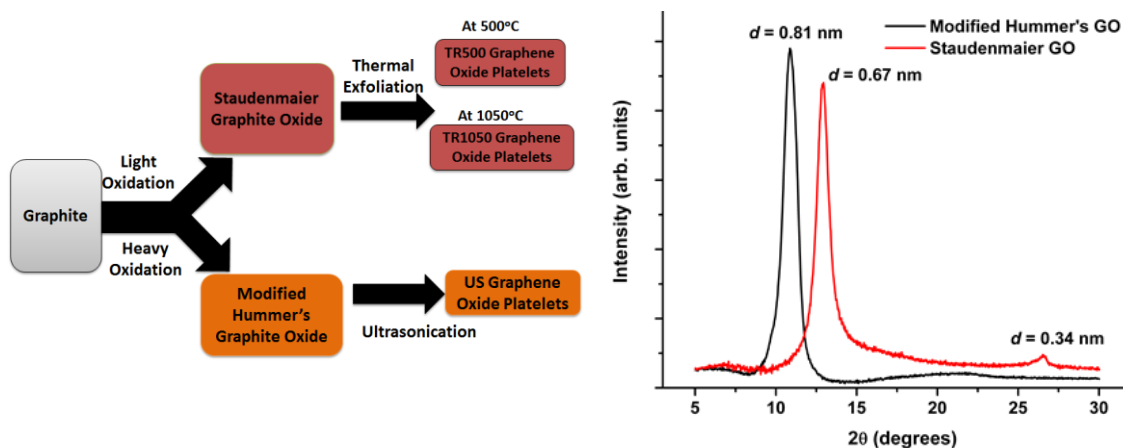


Figure 5.1: Overall process flow for preferred methods of GOP production

Figure 5.2: X-Ray diffraction data of GO

5.1.1.1 Thermal Shock Exfoliation of Graphite Oxide- Powder Processing

The thermal exfoliation technique works by consuming some of the graphite oxide to form carbon dioxide gas, which in-turn induces a tremendous interlayer pressure in the remaining stack-structure of the GO. This pressure causes the graphite oxide to

explode into single or multiple-layer, partially-deoxygenated, thermally-reduced graphene oxide platelets (TR GOP) [29, 127].

The GO produced from the Modified Hummer's method did not exfoliate well in the thermal shock furnace. This is attributed to the high oxygen content in the GO produced using this method. The presence of such high oxygen content causes most of the graphite to get consumed in the production of CO₂ gas during the thermal shock, which in-turn results in a poor yield of TR GOP. In addition to the poor yield, the furnace also showed deposits of a soot-like material that caused the TR GOP to adhere to the walls of the fabrication vessel, thereby increasing the difficulty of extracting the TR GOP.

The GO produced using the Staudenmaier method was observed to be better suited for thermal exfoliation. This is attributed to the limited amounts of oxygen moieties in the GO produced using this method, which results in a lower consumption of graphite during the production of CO₂. Thermal shock was carried out on the Staudenmaier GO at two temperatures, 500°C and 1050°C. The resulting thermally-reduced graphene oxide platelets will be referred to as TR500 and TR1050, respectively, for the remainder of this chapter.

5.1.1.2 Ultrasonication-based Exfoliation of Graphite Oxide- In-solution Processing

In this technique, graphite oxide is exfoliated in-solution using ultrasonication energy. The graphene oxide platelets produced using this method will be referred to as US GOP for the remainder of the chapter. Deionized (DI) water was chosen as the suspension medium since it is used as a diluent for semi-synthetic cutting fluids [25]. The GO obtained using the Modified Hummer's method was seen to be more suitable for this technique as opposed to the one obtained using the Staudenmaier method. This is attributed to the fact that the MH method over-oxidizes the GO with strong acidic groups. Models for graphite oxide produced using the MH method have shown that there exists acidic oxidative debris on the surface of the GO [43, 129]. This oxidative debris acts as a surfactant in aqueous suspensions and renders the GO hydrophilic, allowing it to be easily dispersed in water. Such surfactant groups are absent in the case of the GO obtained from the Staudenmaier method, which impedes their suspension in DI water.

5.1.2 Dimensional Characterization of Graphene Oxide Platelets

Figure 5.3(a)-(c) shows sample scanning electron microscope (SEM) images of the TR500, TR1050, and US graphene oxide platelets used in this study. Even though the lateral size measurements could be estimated using the SEM, this measurement technique has a major limitation. The surfactants present in semi-synthetic cutting fluids affect the colloidal stability of the GOP suspensions, which in-turn influences the agglomeration of GOP in the solution. Therefore, the ex-situ size analysis of the platelets may not be an accurate representation of the effective GOP lateral dimensions that are seen by the tool and the workpiece. With this in mind, alternate techniques that allowed for in-solution measurement of the lateral dimension of the GOP were explored.

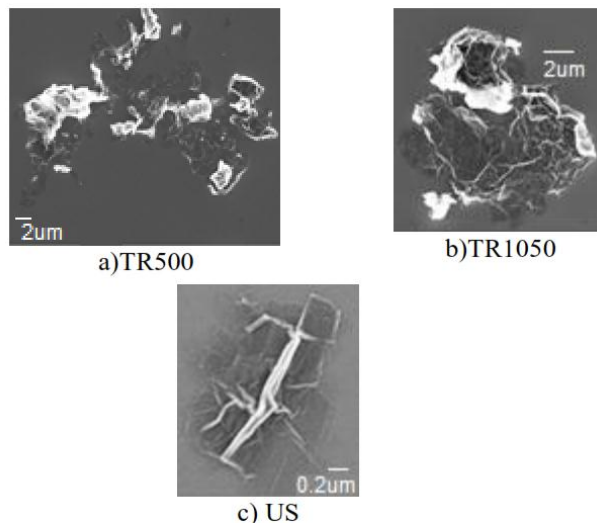


Figure 5.3: SEM images of GOP

5.1.2.1 Dynamic Light Scattering (DLS) for In-Solution Lateral Size Estimation

This technique is used to determine the size distribution of the particles in a solution [130]. It relies on the principle, that when colloidal particles being measured are of the same order of magnitude as the wavelength of the monochromatic laser source being shone on the solution, the particles will scatter the light. This scattering causes constructive and destructive interference, which is recorded by a receiver. Using such a signal, over time, one can calculate a size distribution of the particles by relating the fluctuation in signal intensity to Brownian motion. DLS is typically used for estimating of the hydrodynamic diameter of spherical particles in solution form. When used on a GOP suspension, this method will not provide the absolute value of the lateral

dimensions of the GOP sheets. However, it is able to provide a numerical hydrodynamic diameter value, which better represents the lateral size seen by the tool and the workpiece.

A 1:7 mixture by volume of Castrol Clearedge™ 6519 semi-synthetic cutting fluid in DI water was used in these experiments as the baseline cutting fluid. Figure 5.4(a)-(c) show the DLS analysis of the three different types of graphene oxide suspensions made using this baseline cutting fluid. As seen in the figures, a bi-modal size distribution is apparent where oil droplets with ~50nm hydrodynamic diameter appear in the emulsion along with the hydrodynamic diameters of the GOP clusters. As seen from the DLS data, the hydrodynamic diameter of the US GOP is 120 nm (Figure 5.4(c)). The TR GOP hydrodynamic diameters were seen to be 562 nm and 2781 nm at the reduction temperatures of 500 C and 1050 C, respectively (Figure 5.4 (a)–(b)).

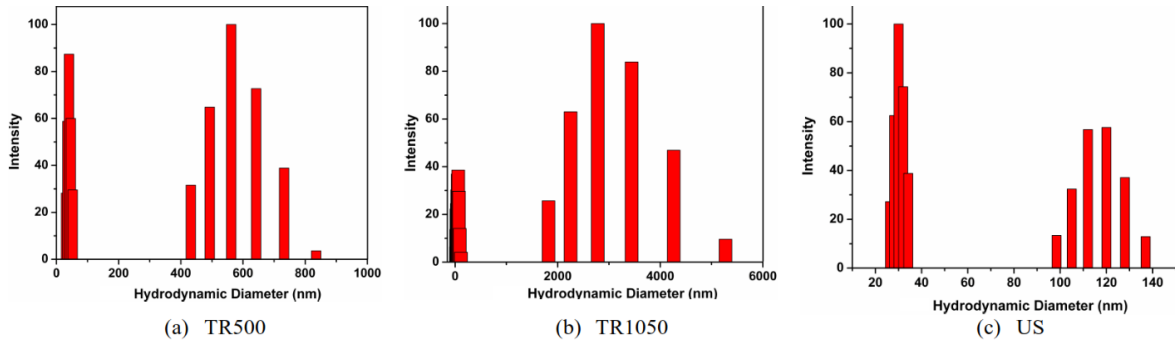


Figure 5.4: DLS data showing the statistical distribution of various GOP sizes

5.1.2.2 Brunauer-Emmett-Teller (BET) Surface Area Measurements for Estimating Relative Thickness

Atomic force microscopy (AFM) is typically used for the measurement of steps-heights, when the feature is mounted carefully on a flat surface like Si or SiO₂. When the GOP dispersions are dried out for an AFM measurement, they tend to agglomerate and create “flowerlike” morphologies that are hard to scan using an AFM. Additionally, since AFM scans are limited in their scan-area per measurement, several data points would have to be collected for any statistical significance. Therefore, the BET surface area measurement technique is used here to provide a more statistically relevant estimate of the number of layers present in the GOP [131].

The BET surface area measurements involve a nitrogen adsorption-desorption cycle as shown in Figure 5.5. All measurements were made with a Quantachrome AS-1™ at a temperature of 77 K, using nitrogen as the adsorbent gas. This measurement relies on the principle that a single sheet of graphene has a theoretical surface area of 2630 m²/g, and as the number of graphene sheets present in a single platelet increases, the effective “exposed” surface area available for nitrogen adsorption reduces [131]. The hysteresis in the nitrogen adsorption-desorption cycle can be used to estimate the effective “exposed” surface area of the graphene oxide platelets. Given the extremely low interlayer spacing (~0.34 nm) for stacked graphene, adsorption on the internal surfaces is much lower as compared to the exposed external surface. Therefore, for this estimation, it was assumed that two layers of graphene stacked together would effectively double the mass while keeping the exposed surface area for gas adsorption constant. Thus, the surface area measurements can be used to estimate the average number of individual graphene layers present in each flake, thereby estimating the overall thickness of the platelet.

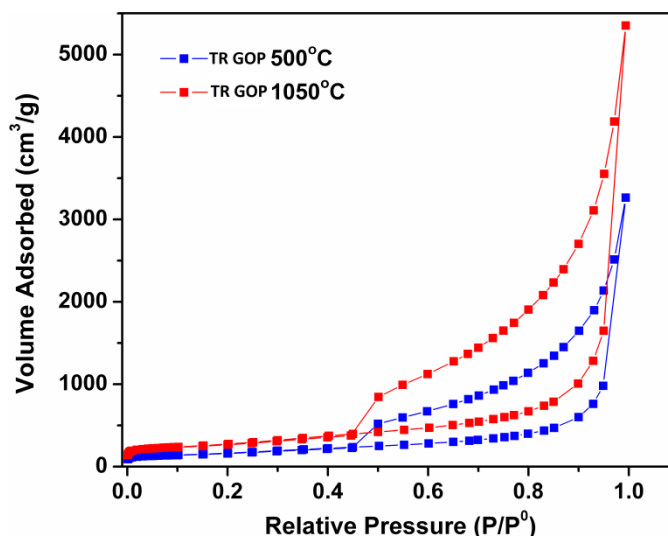


Figure 5.5: BET adsorption-desorption isotherms for TR GOP powders

The BET surface area measurements revealed a surface area of ~612 m²/g and ~369m²/g for the thermally-reduced GOP exfoliated at 1050°C and 500°C, respectively. Using 2630 m²/g as the theoretical value for a single atom thick carbon sheet, an estimate of the number of graphene layers is obtained. The surface area values indicate ~4-5 layers for the TR1050 GOP while the TR500 GOP seems to have ~7-8 layers. A relatively lower surface area for the GOP exfoliated at 500°C indicates that reducing the

temperature of exfoliation decreases the intensity of deoxygenation, thereby resulting in thicker graphene platelets. The thickness of the US GOP could not be estimated using the BET technique since they are not in the dry powder form. Therefore, electron microscopy technique was used to estimate the thickness to be ~2-3 layers.

5.1.2.3 Results and Discussion

Table 5.1 depicts the summary of all the measurements that were made using the DLS and the BET tests. It should be noted that while the DLS data provides the estimated hydrodynamic diameter for a spherical particle, a direct correlation exists between the characteristic length obtained through this measurement and the actual lateral size of the graphene platelet in suspension.

	TR500	TR1050	US
Dynamic light scattering (DLS) measurements: In-solution form	562.41nm	2781.1nm	120.0nm
Characteristic lateral length (hydrodynamic diameter)			
Brunauer-Emmett-Teller (BET) measurements: Dry powder form	368.5m ² /g	612.6	^a
Surface area measurement		m ² /g	
Thickness estimate ^b	7-8 layers	4-5 layers	2-3 layers ^c

^a Could not be estimated using the BET technique since they are not in the dry powder form.

^b The number of layers estimate is based on 2630 m²/g being the theoretical surface area for single atomic layer of carbon

^c Measured indirectly using electronic microscopy

The BET measurements indicate that the TR500 GOP is thicker (7-8 layers) than the TR1050 GOP (4-5 layers). This is to be expected, considering a higher intensity of thermal shock would result in rapid deoxygenation and thus better exfoliation of individual graphene sheets [48]. One would expect that the higher the extent of exfoliation, the smaller the lateral size of the graphene platelets in-solution. However, the DLS data contradicts this assumption. It was found that TR1050, which should be smaller and thinner based on BET measurements, actually formed larger flakes than TR500 in-solution. The higher temperature of thermal shock thus produced larger sized (~2781 nm) GOP in-solution, whereas the lower temperature of thermal shock produced smaller-sized sheets (~562 nm) in-solution.

The discrepancy between the BET and DLS data, though counterintuitive at first, makes more sense when the role played by the oxygen functional groups is examined carefully. The polar oxygen functional groups present on graphite oxide are removed

violently during the thermal shock process, as carbon from the graphite reacts with the oxygen to form carbon oxides that generate extremely high interlayer pressures. This results in the rapid exfoliation of graphite oxide into reduced graphene oxide flakes. Higher temperatures do produce flakes with higher surface area, but have much lesser oxygen content [132]. Residual oxygen functional groups play a crucial role in reducing agglomeration through electrostatic repulsion between individual platelets when dispersed in an aqueous environment. For the TR GOP, there is a greater loss of oxygen moieties when the platelets are exfoliated at 1050°C than when the exfoliation is conducted at 500°C. The lower surface energy of highly-reduced graphene oxide platelets (that are formed by exfoliation at 1050°C) is responsible for their hydrophobicity and resultant agglomeration. This is evident from the observable hydrodynamic diameters that are much larger for TR1050 as compared to TR500. A Gaussian distribution exists for the measured hydrodynamic diameter, with TR500 exhibiting a high probability for values ~562 nm, while the TR1050 shows much larger agglomerates with a mean diameter of ~2781 nm. This difference is significant and indicates that TR500 is better dispersed in aqueous solvents. The presence of oxygen groups also explains why US GOP suspensions exhibit the smallest hydrodynamic diameter of 120 nm, as the polar groups interact with water molecules enabling better dispersibility.

5.1.3 Cutting Fluid Fabrication

A 1:7 mixture by volume of Castrol Clearedge™ 6519 semi-synthetic cutting fluid in DI water was used in these experiments as the baseline cutting fluid. The three different GOP types produced from the methods outlined in Section 5.1 were dispersed in this baseline cutting fluid. Four solutions were made for each type of GOP at concentrations of 0.1%, 0.2%, 0.5%, and 1% GOP by weight. These liquids were characterized for their dynamic viscosity and thermal conductivity values.

The dynamic viscosities of the fluids were measured using a Brookfield DVII+™ viscometer. Results are shown in Table 5.2. The results show that the addition of GOP increases the viscosity in all cases. For all concentrations < 0.5 wt%, the increase in dynamic viscosity for the GOP-laden fluids is less than ~22%, when compared to that of

the baseline cutting fluid. For concentrations > 0.5 wt% the viscosities of the US GOP fluids increase sharply, with a $\sim 75\%$ and $\sim 830\%$ increase for the 0.5 wt% and 1 wt% solutions, respectively. By contrast, the thermally-reduced GOP fluids with loadings ≥ 0.5 wt% show only a nominal increase of $\sim 20\%$ to $\sim 35\%$ in dynamic viscosity.

Thermal conductivity values were measured using a KD 2 ProTM Thermal Properties Analyzer and are likewise listed in Table 5.2. For all concentrations < 0.5 wt%, the increase in thermal conductivity for all GOP fluids is ~ 8 - 16% , when compared to that of the baseline cutting fluid. At the 0.5 wt% concentration, the thermally-reduced GOP fluids reach a maximum in thermal conductivity, with a $\sim 34\%$ and $\sim 20\%$ increase over the baseline cutting fluid for the TR500 and TR1050 fluids, respectively. At the 1 wt% concentration, the thermal conductivity drops back to the range of ~ 8 - 16% increase over that of the baseline cutting fluid. The thermal conductivity of the US GOP solutions shows a peak at 0.2 wt% loading (12% increase over the baseline cutting fluid). These values for the US GOP solutions are then seen to drop to a 2% and 4% increase over the baseline fluid, at loadings of 0.5 wt% and 1 wt%, respectively. This decrease in the thermal conductivity of the solutions at higher loadings is likely due to clumping of the GOP, which has been seen to modify the thermal conductivity of nanofluids [133].

5.2 Micro-machining Performance Evaluation Experiments

5.2.1 Experimental Setup

A Mikrottools DT-110TM hybrid micro-machining center was used to carry out the performance evaluation tests for the GOP cutting fluids. This testbed is equipped with an 80,000 RPM NSK electric spindle and with linear stages having a ± 1 μm positional accuracy. A cubic boron nitride turning tool (J&M Diamond CBN AR6) with a 400 μm nose radius and an 8 μm edge radius was used to perform the machining experiments. 12L14 steel cylindrical rods of 3 mm diameter were used as the workpiece. The cutting fluids were evaluated at a cutting speed, chip load, and radial depth-of-cut of ~ 300 m/min, 6 $\mu\text{m}/\text{rev}$, and 100 μm , respectively. During the machining operation, the cutting fluids were supplied by using a Nordson 2000XL electronic fluid dispensing unit operated at a dispensing pressure of 60 psi. Figure 5.6 depicts the overall layout of the experimental setup.

Table 5.2: Properties of graphene oxide suspensions in semi-synthetic cutting fluid

	GOP type	Baseling cutting fluid	GOP concentration				
			0.1 wt% GOP	0.2 wt% GOP	0.5 wt% GOP	1 wt% GOP	
Dynamic viscosity (cP)	TR 500	1.800	2.100	2.000	2.200	2.350	
		%diff	+16.67%	+11.11%	+22.22%	+30.56%	
	TR 1050	1.800	1.950	2.000	2.150	2.450	
		%diff	+8.33%	+11.11%	+19.44%	+36.11%	
	US	1.800	1.850	2.200	3.150	16.70	
		%diff	+2.78%	+22.22%	+75.00%	+827.78%	
Thermal conductivity (W/m K)	TR 500	0.531±0.010	0.590±0.012	0.614±0.024	0.715±0.052	0.310±0.014	
		%diff	+11.15%	+15.71%	+34.01%	+14.80%	
	TR 1050	0.531±0.010	0.613±0.003	0.581±0.011	0.635±0.018	0.572±0.011	
		%diff	+15.52%	+9.45%	+19.55%	+7.68%	
	US	0.531±0.010	0.575±0.010	0.596±0.014	0.514±0.007	0.554±0.002	
		%diff	+8.29%	+12.32%	+1.96%	+4.37%	

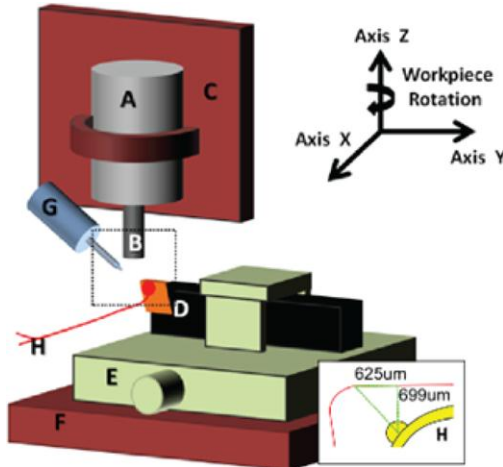


Figure 5.6: Experimental setup with inset showing thermocouple bead location [25]. (A) high-speed spindle, (B) workpiece, (C) Y-Z stage of machine, (D) CBN tool, (E) dynamometer, (F) X stage of machine, (G) cutting fluid dispensing syringe, and (H) thermocouple

Cutting forces, cutting temperature, and surface roughness were used as the measures to evaluate the performance of the cutting fluids. Cutting forces were measured using a Kistler 9256C1 multi-component dynamometer and cutting temperatures were measured using a surface-mounted, J-type bead thermocouple attached to the turning tool. The signal from the thermocouple was amplified by a National Instruments SCXI-1112 8-Channel Thermocouple Input Module. Both the cutting force and the temperature signals were sampled at 30 kHz. Table 5.3 presents a summary of the micro-machining conditions.

Table 5.3: Turning conditions using graphene-enhanced semi-synthetic cutting fluid

Workpiece	12L14 Steel
Surface Speed	300 m/min
Chip Load	6 $\mu\text{m}/\text{rev}$
Depth of Cut	100 μm
Turning Tool	Manufacturer: J&M Diamond (# CBN AR6) Cubic Boron Nitride; 400 μm nose radius; 8 μm edge radius; 0° Rake angle, 10° Clearance angle
Cutting fluid dispensing pressure	60 psi

5.2.2 Cutting Temperature and Cutting Force

In order to ensure an effective comparison of the cooling performance of the cutting fluids, it is critical that the same tool-thermocouple combination be used to compare all the liquids. This is because the temperature measurement varies significantly based on the positioning of the thermocouple with respect to the cutting edge [25, 56, 98-99, 134-138]. Preliminary tests revealed that attaching the thermocouple too close to the cutting

edge caused the chip formation process to destroy the thermocouple before the testing of all the cutting fluids could be completed. A mounting distance of 625 μm away and 699 μm below the nose of the cutting tool was found to be essential to ensure that the thermocouple bead could survive all the cutting tests (Figure 5.6). While the measured cutting temperature at this distance will be significantly lower than that inside the cutting zone (which, for steel is typically in the hundreds of centigrade range [137]), the relative difference between the temperatures seen for the cutting fluids can still be used to compare their cooling performance [25, 56, 98-99, 134-137].

Figure 5.7(a)-(b) depict the cutting temperature and cutting force data obtained from the micro-machining experiments. The horizontal line in these figures represents the data obtained for the baseline cutting fluid. In Figure 5.7(a) the maximum temperatures measured for the GOP colloidal suspensions are presented as a percentage of the maximum temperature value measured for the baseline cutting fluid. A negative percentage value in Figure 5.7(a) indicates a lower temperature rise, i.e., a better cooling performance than that seen for the baseline cutting fluid, whereas a positive value indicates a greater temperature rise, i.e., a poorer cooling performance than that seen for the baseline cutting fluid.

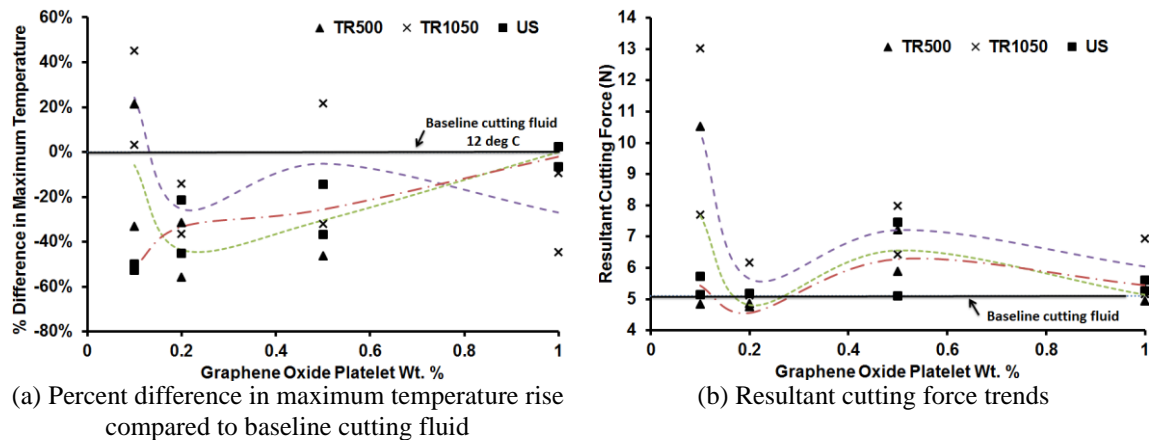


Figure 5.7: Cutting temperature and force trends seen for the GOP colloidal solutions. (note: thermocouple measurements have a repeatability of 60.1 C and dry cutting conditions gave a temperature rise of 35 C)

In general, for all concentrations except for 0.1wt%, all GOP colloidal solutions are seen to have a better cooling performance than the baseline cutting fluid, with the recorded temperatures being 20-60% lower than those for the baseline cutting fluid (Figure 5.7(a)). There are a few cases for which the GOP fluids perform worse than the

baseline cutting fluid. This deterioration in the cooling performance is caused by the corresponding increase in the cutting forces observed for these same conditions (Figure 5.7(b)). For the two thermally-reduced GOP fluids, the relationship between cutting temperature and weight percentage loading closely follows the corresponding trend seen in the cutting forces (Figure 5.7(b)). At 0.1 wt%, the TR500 and TR1050 solutions perform significantly worse than at the other concentrations. For the thermally-reduced GOP, the best cooling performance appears to be at 0.2 wt% concentration, with higher concentrations having less significant an impact on the cooling performance.

The US GOP solutions, on the other hand, perform quite differently. Even at the lowest 0.1 wt% concentration, it provides the best cooling performance amongst all the other GOP types. At 0.2 wt% it is more effective than the thermally reduced GOP in reducing both the cutting temperatures and the cutting forces. However, at concentrations ≥ 0.5 wt% the cooling performance of US GOP is seen to worsen, with the highest loading of 1wt% yielding the same performance as the baseline cutting fluid.

The data from the cutting force trends (Figure 5.7(b)) reveals that the US GOP solutions deliver a lubrication performance that is comparable to the baseline cutting fluid, whereas for the most part, the TR GOP solutions result in cutting forces that are greater than the baseline cutting fluid. At concentrations < 0.5 wt%, all GOP types demonstrate a comparable trend in the cutting force as a function of the concentration, with 0.1 wt% resulting in the highest force and the 0.2 wt% resulting in the lowest force. It can also be seen that at 0.1 wt%, the variation in the cutting forces for the thermally-reduced GOP solutions is very large. The cutting forces are again seen to increase at 0.5 wt% and then appear to level off at 1 wt% (Figure 5.7(b)). In terms of cutting force performance, it appears that the US GOP performs the same or better than both the thermally reduced GOP at all concentrations.

5.2.3 Surface Roughness

In order to characterize the surface roughness of the part, the machined workpieces were first cleaned by ultrasonication in acetone and then scanned using a Zeta20 optical profilometer. Scans were taken over several $191\mu\text{m} \times 143\mu\text{m}$ areas sampled at locations approximately halfway into the cut. Figure 5.8 shows the trends seen in area surface

roughness values (S_a). Except for the two outliers of TR500 GOP at 0.2 wt% and US GOP at 0.5 wt% loadings, the use of GOP-laden cutting fluids is seen to reduce the surface roughness of the machined workpiece, when compared to that obtained by the baseline cutting fluid. At 0.1 wt%, the US and TR500 GOP result in the lowest S_a values followed by TR1050. At other loadings, there appears to be no clear winner between the three GOP types.

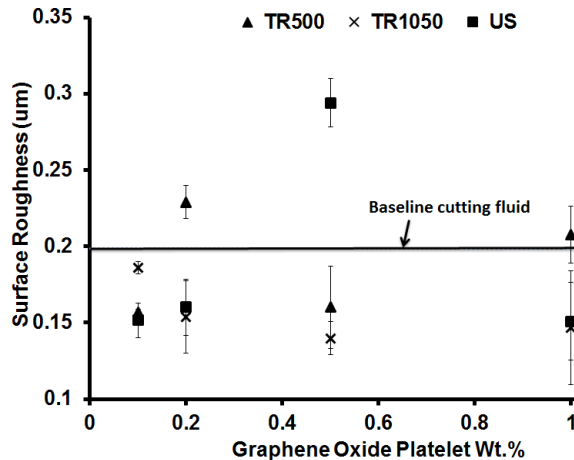


Figure 5.8: Surface roughness trends seen for GOP colloidal solutions

5.3 Discussion

In general, the thinner and smaller GOP produced by ultrasonic exfoliation appears to be best suited for micro-machining applications. Even at the lowest loading of 0.1 wt%, they appear to provide excellent cooling and surface roughness results while still maintaining the cutting forces at a level comparable to that of the baseline cutting fluid. This is in spite of the fact that both the thermal conductivity and the dynamic viscosity of 0.1% US GOP solutions are lower than the corresponding values for the thermally-reduced GOP liquids (refer Table 5.2). There appears to be no clear winner between the TR500 and TR1050 GOP in terms of the machining performance of their colloidal solutions. For these larger and thicker GOP types, a concentration of 0.2 wt% appears to be ideal. However, even at this concentration, the US GOP is more effective than the thermally-reduced GOP in reducing both the cutting temperatures and the cutting forces.

The machining results also reveal that concentrations >0.5 wt% do not provide any machining benefits for any of the GOP colloidal solutions. This is again in spite of the

fact that the thermal conductivity and the dynamic viscosity of the bulk liquids are seen to improve at concentrations > 0.5 wt%. The above findings reveal that the differences seen between the colloidal suspensions in terms of their droplet spreading, evaporation and the subsequent GOP film-formation characteristics may be better indicators of their machining performance, as opposed to their bulk fluid properties. These mechanisms are investigated in Chapter 6.

5.4 Summary

The following specific conclusions can be drawn from this study:

1. Thermal and ultrasonic exfoliation techniques were developed to fabricate graphene oxide platelets (GOP) of varying lateral dimensions, thickness and oxygen functionalization that could serve as additives for semi-synthetic cutting fluids. The thermal reduction technique was seen to result in a thicker GOP with 4-8 graphene layers, (depending on the processing temperatures), whereas the ultrasonic exfoliation resulted in a thinner GOP with 2-3 graphene layers.
2. The extent of oxygen functionalization of the GOP was seen to be a key factor affecting the agglomeration of the platelets in the colloidal suspension. Low levels of oxygen functionalization (using thermal exfoliation) resulted in relatively larger in-solution characteristic lateral lengths of 562 -2780 nm, whereas the higher level of oxygen functionalization (using ultrasonic exfoliation) was seen to result in the lowest in-solution characteristic lateral length of 120 nm.
3. In general, the addition of GOP is seen to increase both the dynamic viscosity as well as the thermal conductivity of the cutting fluids.
 - At concentrations < 0.5 wt%, the increase in the dynamic viscosity for all GOP-laden fluids is less than 22% when compared to that of the baseline cutting fluid. However, at concentrations > 0.5 wt%, sharp increases of 75-830% are seen in the dynamic viscosities for the ultrasonically exfoliated GOP solutions.
 - At concentrations < 0.5 wt%, the increase in thermal conductivity for all GOP-laden fluids is 8-16% when compared to that of the baseline cutting fluid. The thermally-reduced and ultrasonically-exfoliated GOP solutions

show a peak in their thermal conductivity at 0.5 wt% and 0.2 wt%, respectively.

4. The micro-machining tests reveal that the GOP colloidal suspensions are capable of improving the performance of the baseline cutting fluid by significantly reducing the cutting temperatures and surface roughness encountered during the machining process. However, the cutting forces are generally noticed to be higher for these solutions.

- The ultrasonically-exfoliated GOP appears to be the most favorable for micro-machining applications. Even at the lowest concentration of 0.1 wt%, they are capable of providing a ~51% reduction in the cutting temperatures and a 25% reduction in the surface roughness values over those of the baseline cutting fluid. The 0.2 wt% loading provides the optimal combination of both low cutting forces as well as cutting temperatures.
- For the thermally-reduced GOP solutions, the 0.2 wt% appears to be ideal since it results in the lowest cutting temperatures (25-43% reduction over the baseline cutting fluid) and cutting forces that are comparable to the baseline cutting fluid. However, even at this concentration, the US GOP is seen to outperform the TR GOP.

5. The micro-machining tests reveal that the bulk properties of the colloidal suspensions are weakly correlated to the machining performance of the fluids. This suggests that that the differences seen between the colloidal suspensions in terms of their droplet spreading, evaporation, and the subsequent GOP film-formation characteristics may be better indicators of their machining performance, as opposed to their bulk properties.

6. DROPLET DYNAMICS AND FILM FORMATION MECHANISMS OF GRAPHENE OXIDE COLLOIDAL SUSPENSIONS

This chapter is focused on understanding the cooling and lubrication performance of the oxide platelet (GOP) colloidal solutions benchmarked in Chapter 5. This was done by investigating the droplet spreading and subsequent evaporation characteristics of the solutions. First, a high-speed imaging investigation was conducted to study the impingement dynamics of the GOP solutions on a heated substrate. The spreading and evaporation characteristics of the fluids were then correlated with the corresponding temperature profiles and the subsequent formation of the graphene oxide film on the substrate. The results obtained from these investigations shed light on the possible mechanisms responsible for the cooling and lubrication performance of these GOP colloidal solutions.

The remainder of this chapter is organized as follows: Section 6.1 presents the details of the experimental setup used for the single-droplet impingement study. Section 6.2 discusses results of these experiments in terms of the droplet temperature profiles, droplet evaporation behavior, and characterization of the residual graphene oxide film deposited on the substrate. This is followed by Section 6.3, which connects the results from the single-droplet impingement study to the cooling and lubrication performance of the colloidal solutions seen in Chapter 5. Finally, Section 6.4 summarizes the specific conclusions that can be drawn from this work

6.1 Experimental Setup for the Single-droplet Impingement Study

The use of cutting fluids in micro-machining processes involves their delivery into a high-temperature zone [137]. The work of Ghai *et al.* [98] showed that for semi-synthetic cutting fluids, the spreading and evaporation characteristics of the droplets affect the cooling and lubrication performance of the cutting fluid. For the case of GOP colloidal solutions, this mechanism is further complicated by the presence of the platelets, which are expected to affect the spreading/evaporation characteristics of the

This chapter previously appeared as: B. Chu and J. Samuel, "Graphene oxide colloidal suspensions as cutting fluids for micromachining—Part II: Droplet dynamics and film formation," *J. Micro Nano-Manuf.*, vol. 3, no. 4, pp. 041003–041003, Aug. 2015.

droplet, as well as the characteristics of the graphene oxide film that is left behind. This film is a critical component of the performance of these fluids since it is likely to deposit at the interface between the tool and the workpiece and will therefore influence both the temperature and the cutting forces encountered in machining. Therefore, a single-droplet impingement study was designed to investigate these mechanisms specific to the use of GOP colloidal suspensions as cutting fluids.

Figure 6.1 depicts the overall setup of the impingement experiment, which consists of an electronic fluid delivery (EFD) nozzle mounted over a heated glass substrate with a built-in thermocouple. The EFD used in this study is the same unit that was used to deliver the cutting fluid for the micro-machining study reported in Part 1. This ensures that the droplet volumes are comparable between the two studies. A Phantom V7.3TM high-speed camera was focused on the droplet impact zone to capture the physical evolution of the droplets. The front and top views of the droplet (Figure 6.1(b)-(c)) were obtained by aligning the camera axis at 90° and 30°, respectively, to the axis of the EFD nozzle (Figure 6.1(a)). A Prior Lumen 200TM high-intensity light source was used to provide the illumination for the high-speed camera.

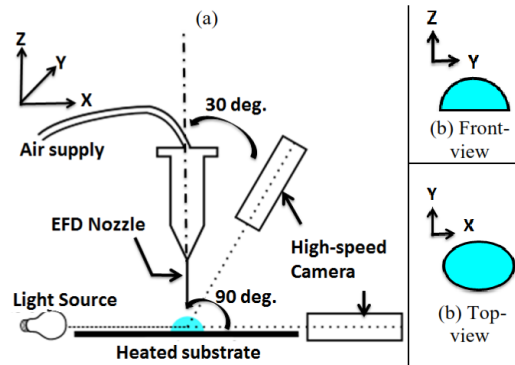


Figure 6.1: Experimental setup for single-droplet impingement study

The glass substrate was maintained at a steady state temperature of $\sim 100^{\circ}\text{C}$ for this study. While the temperatures encountered within the micro-machining environments are several hundreds of degree centigrade [137], this lower temperature-level was chosen to ensure that the time-scales of droplet spreading, evaporation, and film-formation allowed for a sufficient amount of data to be collected by the high-speed camera and the thermocouple. Since the time-scale of droplet dynamics on heated substrates is known to scale exponentially with the substrate temperature [138], it can be expected that for the

higher temperatures encountered in micro-machining, the droplet behaviors seen in these experiments would occur at significantly smaller time-scales than those seen in this study. Table 6.1 summarizes the overall experimental conditions maintained for this study. For the droplet temperature profile and evaporation regime studies, a total of ten droplets were deposited for each of the colloidal solutions, with the substrate being cleaned between each droplet deposition using acetone. For the characterization of the residual graphene oxide film, a separate set of five droplets were deposited for each of the colloidal solutions.

Table 6.1: Experimental conditions for droplet impingement study

Colloidal Solutions	<ul style="list-style-type: none"> • Baseline cutting fluid (CF) • 0.1%, 0.2%, 0.5%, and 1% by weight solutions of: <ul style="list-style-type: none"> ○ TR500 GOP + baseline cutting fluid ○ TR1050 GOP + baseline cutting fluid ○ US GOP + baseline cutting fluid
Substrate	<ul style="list-style-type: none"> • Material: Gold-plated glass slide • Temperature: 100°C
EFD	<ul style="list-style-type: none"> • Back pressure: 60psi • Pulse duration 0.005s
Sampling Rate	<ul style="list-style-type: none"> • Thermocouple – 5000 samples/sec • High-speed camera- 5000 samples/sec
Imaging Duration	<ul style="list-style-type: none"> • ~14s

6.2 Experimental Findings

The experimental findings can be classified under three categories *viz.*, 1) Droplet temperature profiles, 2) Droplet evaporation behavior, and 3) Residual graphene oxide film characterization. This section presents the results from each of these three categories of findings.

6.2.1 Droplet Temperature Profile

Figure 6.2 depicts the temperature profile seen for the 0.2 wt% TR500 colloidal solution, after a droplet impacts the heated substrate. This profile is representative of that seen for most of the colloidal solutions. Analysis of the temperature profiles and the corresponding high-speed images of the droplet shape evolution reveal three distinct regimes of droplet behavior for all the GOP solutions, *viz.*, 1) the *spreading regime* (Region A-B-C in Figure 6.2), where the droplet is deposited on the surface; 2) the *pinning regime* (Region C-D in Figure 6.2), where convection heating causes some loss

of droplet volume; and finally 3) the *receding regime* (Region D-E in Figure 6.2), where the droplet is seen to evaporate completely.

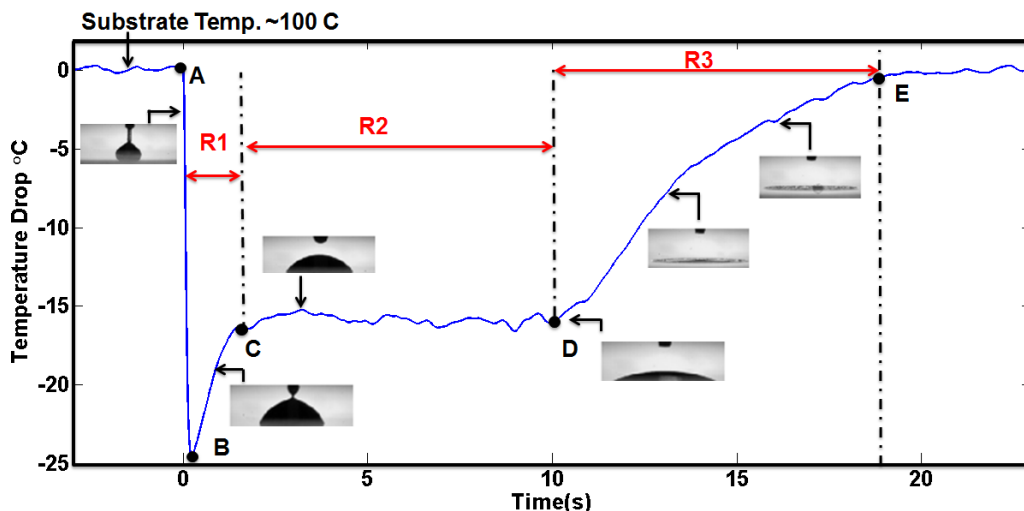


Figure 6.2: Characteristic temperature profile of a 0.2 wt% TR500 droplet with insets showing droplet shape. (Note: R1= Spreading regime, R2= Pinning regime and R3 = Receding regime)

In the *spreading regime* (Region A-B-C in Figure 6.2), the droplet is being deposited by the EFD, and as a result, it grows in volume on the substrate. During this phase, the temperature is seen to rapidly drop as room temperature fluid is introduced onto the heated substrate. The evaporative losses are observed to be negligible in this regime. Toward the end of this regime, the droplet shape oscillates for a short period after the jet ceases to deliver the liquid. After these initial oscillations, the droplet enters the *pinning regime* (Region C-D in Figure 6.2) where the contact area of the droplet is pinned. The droplet height and contact angle are seen to reduce with time, due to evaporation. In this regime, it is also observed that convection quickly brings the temperature to an equilibrium level that is $\sim 10^{\circ}\text{C}$ higher than the lowest temperature seen in the spreading Region A-B-C at point B (Figure 6.2).

Finally, at the beginning of the *receding regime* (Region D-E in Figure 6.2), the droplet reaches its minimum contact angle with the substrate. At this stage, the droplet boundary unpins and begins to recede rapidly due to further evaporation of the carrier liquid. During this phase, boiling phenomenon can also be observed for some of the fluids. The rapid decrease in the droplet volume results in a return to the original substrate temperature of $\sim 100^{\circ}\text{C}$ (Figure 6.2). As the fluid recedes, a thin film of graphene oxide residue is left behind on the substrate.

In order to effectively compare the temperature profiles between the different fluids, three different numerical metrics were used, *viz.*, 1) the average temperature drop seen in the droplet pinning regime (Region C-D in Figure 6.2); 2) the absolute minimum temperature drop seen at Point B in Figure 6.2; and 3) the time duration of each of the three droplet regimes. Figure 6.3(a) depicts the trends seen in the two temperature-related metrics for each of the colloidal solutions. The average temperature seen in the pinning regime (Region C-D in Figure 6.2) appears to be more or less the same for all the liquids at all concentrations. There also appears to be no clear trends in the absolute minimum temperature drop seen between the solutions. These results for the temperature-related metrics are not surprising because the single-droplet impingement study only measures the temperature drop caused by the evaporative cooling of the colloidal solutions, whereas the temperatures encountered during machining are a combination of the evaporative cooling and the lubrication provided by the graphene oxide film.

The differences between the solutions become more apparent in the trends seen in the time-duration of each of the three regimes (Figure 6.3(b)). In Figure 6.3(b), the total height of the bar-chart denotes the overall duration of the liquid droplet, *i.e.*, the time between points A and E in Figure 6.2. The time-duration of the three regimes is denoted using varying colors within the bar-chart. As seen, the time-duration of the spreading regime is more or less the same for all the liquids. However, the differences between the liquids start showing up in the duration of their pinning and receding regimes.

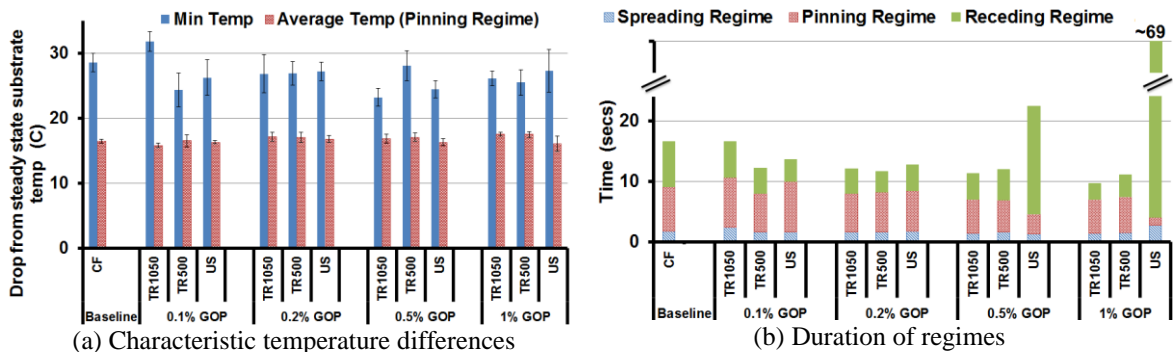


Figure 6.3: Numerical metrics for comparing temperature profiles

For GOP concentrations < 0.5 wt%, all the GOP colloidal solutions are seen to have a shorter overall droplet lifetime when compared to the baseline cutting fluid. The

droplet lifetime is also seen to decrease with an increase in concentration of the GOP. At 0.1 wt%, the TR500 and the US GOP solutions have droplet lifetimes that are lower than those of the TR1050 GOP solution. This indicates that at this low concentration of 0.1wt%, the platelets with lower lateral areas and thickness result in faster evaporation of the liquid. These differences between the TR GOP types appears to level off at 0.2 wt% concentration, although, even at this higher concentration, the TR GOP colloidal solutions are seen to have a shorter overall droplet lifetime when compared to the baseline cutting fluid.

At concentrations > 0.5 wt%, the data in Figure 6.3(b) shows that the overall droplet lifetime for the thermally-reduced GOP solutions is seen to continue to decrease with increasing concentration. However, the US GOP solutions have a distinctly different behavior. They are seen to have the longest overall droplet lifetime, with their pinning regime being the shortest and their receding regime being the longest amongst all the other solutions. Figure 6.4 depicts this behavior in the characteristic temperature profile seen for the 1 wt% US GOP solution. Unlike the profile in Figure 6.2, for the US GOP solutions at concentrations > 0.5 wt%, the transition between the pinning regime (C-D in Figure 6.2) and the receding regime (D-E in Figure 6.4) appears to be less distinct. In the pinning regime, the temperature appears to be increasing, unlike the relatively steady temperature seen in this region for the other fluids (Figure 6.2). The reasons for this behavior are discussed later in Section 6.2.3. The fact that the time-durations of the various droplet regimes are distinctly different, points to the fact that different types of GOP affect the convection, evaporation, and the subsequent film formation process.

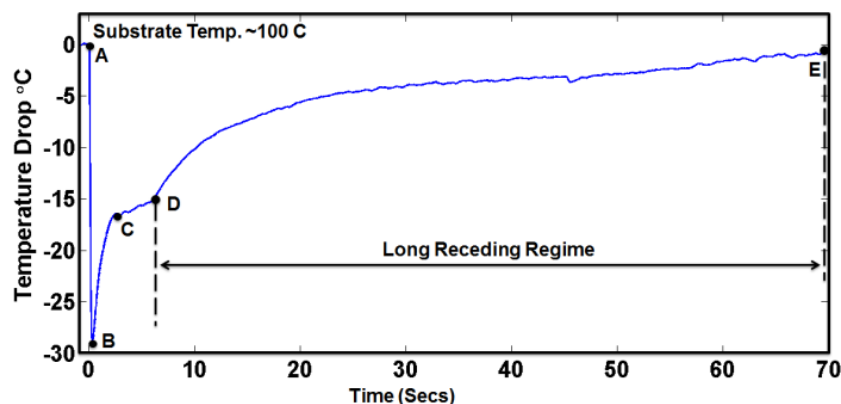


Figure 6.4: Characteristic temperature profile of a 1.0 wt% US GOP solution

6.2.2 Droplet Evaporation: Pinning Regime

Given the differences observed in the time-durations of the pinning and receding regimes of the droplets, the high-speed imaging data from these experiments was analyzed to shed light on the influence of the platelets on these two regimes. In the pinning regime, the droplets were mostly seen to maintain a circular shape in the top-view (Figure 6.1(a)), due to the pinned diameter. Therefore, only the front-view of the droplet was analyzed to study the time-variation in the contact angle and the height of the droplet, resulting from evaporation.

A digital image-analysis algorithm was developed to extract the droplet height and contact angle from every frame captured by the high-speed camera. Figure 6.5(a)-(b) shows the characteristic trends seen in the droplet height and contact angle measurements during the pinning regime of a 0.5 wt% TR500 GOP solution. The regions A, C, and D marked in Figure 6.5 (a)-(b) correspond to the similarly marked regions in Figure 6.2. The data shows transient behavior in the spreading regime A-C since in this region the EFD has not yet fully deposited the droplet. The data for the pinning regime C-D is well-defined and appears to follow a power law of the form:

$$h(t) = \alpha_h t^{-\beta_h} \quad (1)$$

and,

$$\theta(t) = \alpha_\theta t^{-\beta_\theta} \quad (2)$$

where $h(t)$ and $\theta(t)$ denote the height and the contact angle at the time t measured relative to the start of the pinning regime; the multiplicative coefficients, α_h and α_θ , are measures that correlate to the initial values of $h(t)$ and $\theta(t)$, at the beginning of the pinning phase; and the exponential coefficients, β_h and β_θ , are related to the decay rate of $h(t)$ and $\theta(t)$, respectively.

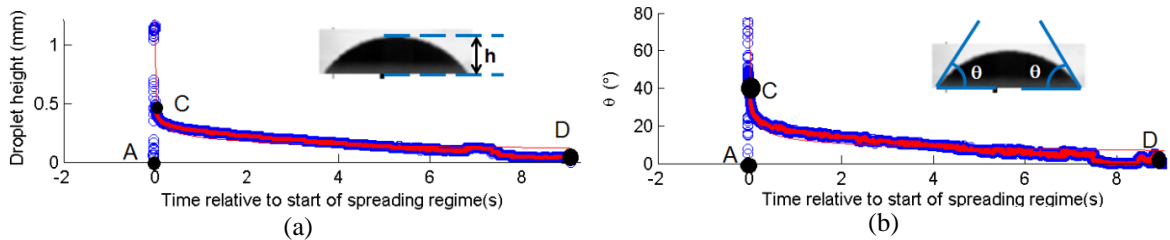


Figure 6.5: Droplet height and contact angle during the pinning regime of a 0.5 wt% TR500 GOP solution

Figure 6.6(a)-(b) show the trends seen in the multiplicative coefficients, α_h and α_0 , for each of the GOP solutions, as a function of their weight concentration. The trends seen in these parameters show that, when deposited on a heated substrate, the GOP fluids have a greater initial height and contact angle compared to the baseline cutting fluid (Figure 6.5(a)). Furthermore, as the concentration increases, the initial height of the droplet stays relatively constant, whereas the initial contact angle increases. This suggests that the GOP modifies the behavior at the gas/liquid/solid interface of the droplet, leading to a decrease in the wettability of the fluid. This behavior of the GOP colloidal solutions on a heated substrate differs from that seen at room temperature where the addition of graphene platelets has been observed to increase the wettability of the liquid [56]. The US GOP is seen to have the greatest effect on the interfacial behavior as compared to the TR500 and TR1050 GOP.

Figure 6.7(a)-(b) show the trends seen in the exponential coefficients β_h and β_0 , for each type of GOP, as a function of their weight concentration. The trends seen in these parameters show that, when deposited on a heated substrate, the GOP fluids have a slower decay rate compared to the baseline cutting fluid (Figure 6.7(a)-(b)). Furthermore, an increase in the concentration of GOP is seen to reduce the rate of decay of the height and the contact angle of the droplet. In all cases, the US GOP fluids evaporate slower than the TR GOP fluids at the same concentration, substantially so at the 1 wt% concentration. This trend mimics the trend seen in the dynamic viscosity of the solutions measured in Part 1[139]. The two TR GOP fluids do not behave substantially differently from one another in this aspect.

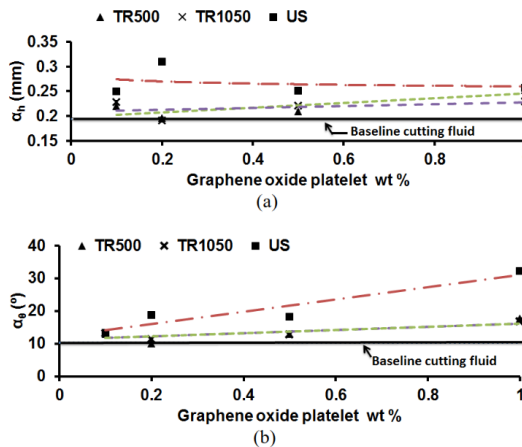


Figure 6.6: Trends for multiplicative coefficients, α_h and α_0

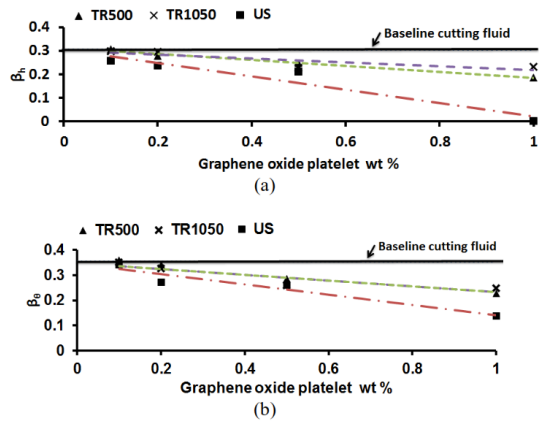


Figure 6.7: Trends for multiplicative coefficients, β_h and β_0

6.2.3 Droplet Evaporation: Receding Regime

Figure 6.8(a)-(x) depict the differences in the droplet evaporation behavior encountered by the different liquids during the receding regime. The evaporation characteristics reveal that there are distinct differences between thermally reduced GOP and US GOP. There are also differences in droplet behavior between low GOP concentration solutions (<0.5 wt%) and high GOP concentration solutions (≥ 0.5 wt%). This section will discuss the results seen for these four categories. It should be noted here that, for all solutions except for the US GOP solutions at concentrations ≥ 0.5 wt%, the last column of images in Figure 6.8 depicts the end of the droplet receding regime.

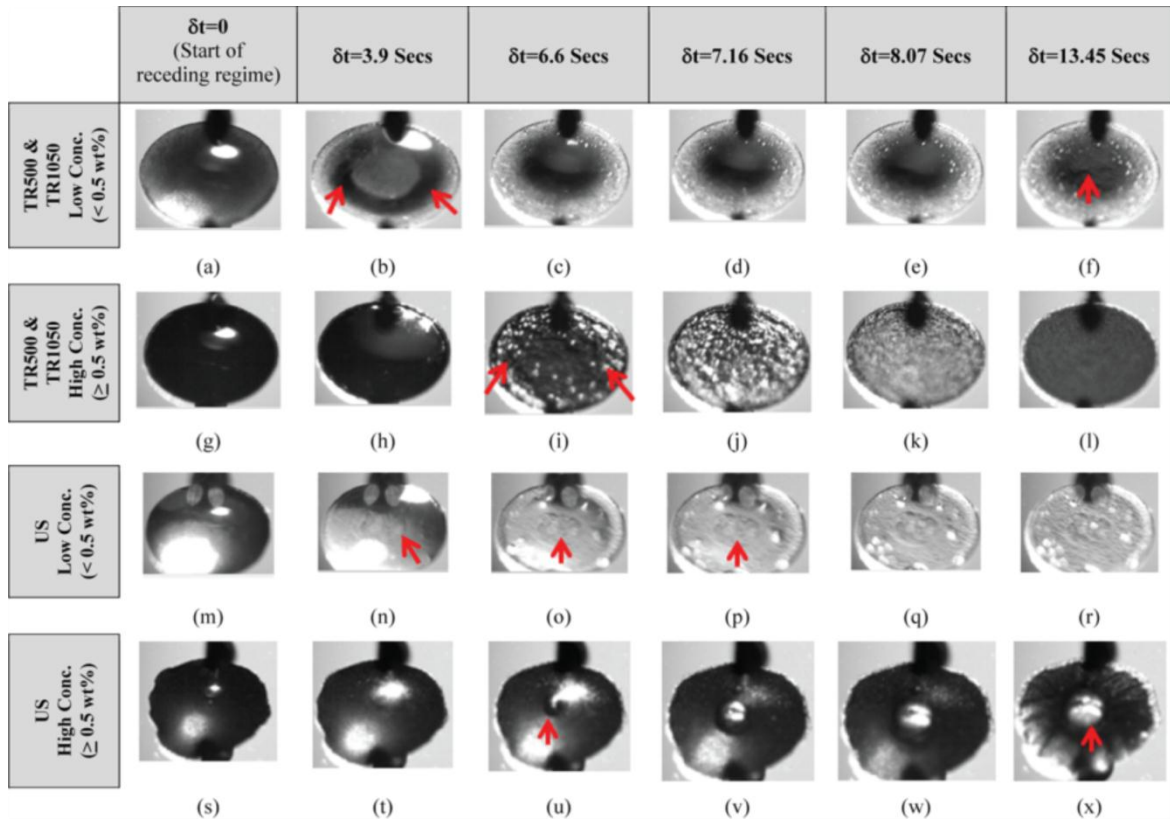


Figure 6.8: Droplet evaporation behavior in the receding regime (top-view)

6.2.3.1 TR GOP at Concentrations < 0.5 wt%

At concentrations < 0.5 wt%, both TR500 and TR1050 GOP solutions exhibit similar evaporation characteristics in their receding regimes (Figure 6.8(a)-(f)). As seen in Figure 6.8(a), the platelets appear to remain relatively well dispersed in the fluid at the beginning of the receding regime. As the droplet evaporates, a small region of high convection is noticeable along the boundary of the droplet (denoted by arrows in Figure

6.8(b)) due to the movement of the suspended platelets. As the droplet recedes, the fluid dynamics within the droplet concentrates the platelets into an annulus that appears to contract with the vaporization of the carrier solution (Figure 6.8(c)-(f)). Ultimately, this phenomenon is seen to result in the formation of a film with radially varying density of GOP (Figure 6.8(f)). The highest concentration of GOP in the film is seen at the center of the droplet.

6.2.3.2 TR GOP at Concentrations ≥ 0.5 wt%

At concentrations > 0.5 wt%, both TR500 and TR1050 GOP solutions continue to exhibit similar evaporation characteristics in the receding regime (Figure 6.8(g)-(l)). The high concentration of GOP is seen to make the droplet too opaque to identify the behavior of the platelets within the fluid (Figure 6.8(g)-(h)). However, as Figure 6.8(i)-(l) reveal, the mechanism of film formation is quite different at these high loadings. While it appears that the formation of the convective annulus does happen along the boundary, the presence of a heavy concentration of GOP is seen to result in a distributed micro-boiling phenomenon (denoted by arrows in Figure 6.8(i)). Although this results in a fairly uniform film (Figure 6.8(l)), the surface of this film is seen to show fissures that are formed by escaping fluid vapors (discussed in Section 6.2.4).

6.2.3.3 Ultrasonically Exfoliated GOP at Concentrations < 0.5 wt%

Figure 6.8(m)-(r) depict the evaporation characteristics seen for US GOP solutions at concentrations < 0.5 wt%. Given the smaller size and the better dispersion of the US GOP, these solutions appear to be more optically transparent than the thermally-reduced GOP solutions at the same loadings (Figure 6.8(a)-(b)). These thinner and smaller platelets also appear to have a different mechanism of film-formation from the TR GOP fluids. As depicted by the arrows in Figure 6.8(n)-(p), it appears that there is a nucleation phenomenon that happens early on in the receding regime, which causes the platelets to form a film on the heated substrate. Over time, the liquid evaporates and leaves behind a very uniform and thin film (Figure 6.8(r)).

6.2.3.4 Ultrasonically Exfoliated GOP at Concentrations ≥ 0.5 wt%

Figure 6.8(s)-(x) depict the evaporation characteristics seen for US GOP at concentrations > 0.5 wt%. In this case, the large time duration of the receding regime (Figure 6.3(b)) makes it difficult to capture high-speed images over the entire lifetime of the droplet. Therefore, it should be noted that Figure 6.8(x) is not the final image of the GOP film left behind on the substrate, but is rather the final frame captured by the camera as the film is being formed.

Figure 6.8(s) shows that these droplets have a jagged boundary line. As seen in Figure 6.6-Figure 6.7, at these high concentrations, the wetting capability of the liquid is drastically altered by the presence of the US GOP. Localized variations in the GOP dispersion within the droplet could explain the jagged boundary line. Figure 6.8(u)-(x) show that as the droplet recedes, vaporized fluid gets trapped inside the droplet (denoted by the arrow in Figure 6.8(u)). This is likely due to the formation of a thin GOP film, at the liquid/gas boundary, similar to the film formed at the liquid/solid boundary at concentrations < 0.5 wt% (Figure 6.8(o)). This vapor trapping, could explain the longer lifetime of the droplet. The final film is seen to be a thick residue that shows evidence of burst vapor bubbles throughout (discussed in Section 6.2.4).

6.2.4 Residual Graphene Oxide Film Characterization

The residual graphene oxide films left behind on the substrate were analyzed using a Zeta-20TM optical 3D profiler to quantify the thickness distribution of the GOP within the film. Given the circular geometry of the film, the scans were restricted to one quadrant of the film. A series of ~ 50 overlapping high-resolution scans were stitched together to compile the thickness-distribution data for each of the four categories of films discussed in Section 6.2.3. A representative sample of this data is shown in Figure 6.9(a)-(d). Subsequently, the scans of the films were used to construct relative-frequency curves for their thickness distribution. This data is shown in Figure 6.10 on a logarithmic relative-frequency scale. In these graphs, a higher relative-frequency value for a given thickness implies that a larger area of the residue film exists at that particular thickness. Data below a relative-frequency of 10 is not shown due to the asymptotic nature of the scale. While data below this threshold exists, it is insignificant compared to the features

that appear above this threshold. Overall, the GOP residue thickness and distribution patterns conform to the same four categories seen in Section 6.2.3.

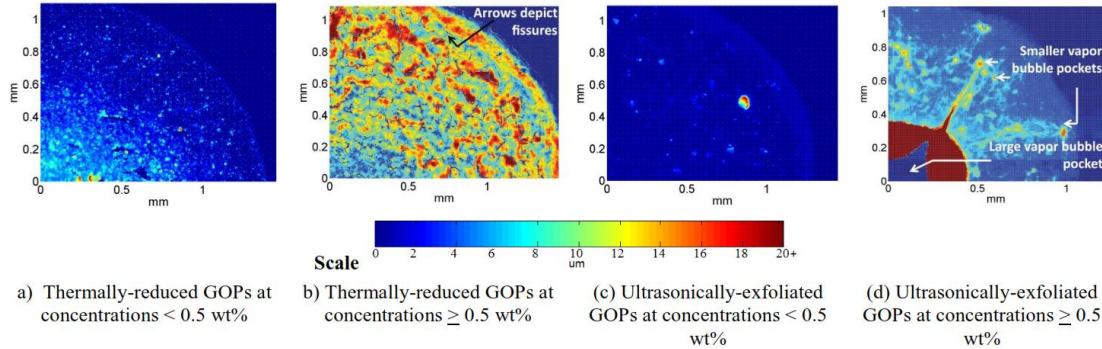


Figure 6.9: Representative graphene oxide film profile scans. (Note: The origin is the center of the circular residue patch)

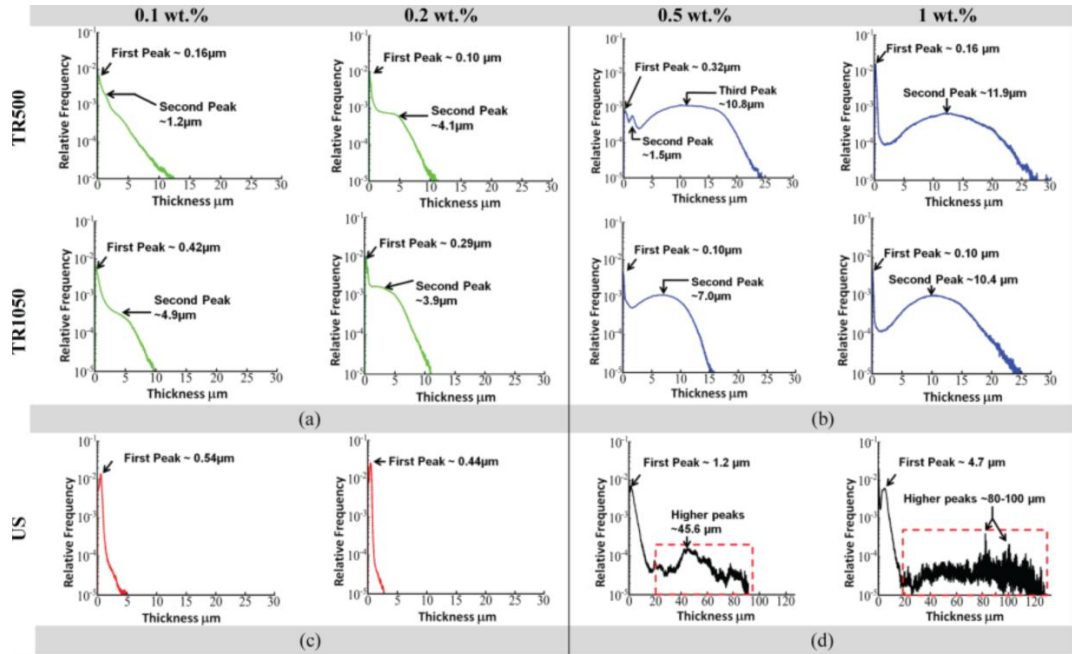


Figure 6.10: Relative-frequency curves for thickness distribution. (Note: The x-axis in (d) is longer than the others)

6.2.4.1 TR GOP at Concentrations < 0.5 wt%

The data seen in Figure 6.9(a) shows that, for this category of solutions, the thickness distribution of the GOP film is non-uniform. The average thickness of the GOP residue decreases with distance from the center of the film, which may be a consequence of the convection-induced movement of the platelets within the droplet (Figure 6.8(b)-(f)). Towards the outer edges of the film, the GOP residue is seen to be relatively thin and patchy in nature, with regions that are not covered by any residue. For

this category, the relative frequency curves for the thickness appear to be a combination of two different distributions (Figure 6.10(a)). The highest peak is observed for thicknesses in the $\sim 0.1\text{-}0.4\ \mu\text{m}$ range, which indicates a predominantly thinner GOP residue that is likely located along the periphery of the film. The second dominant distribution has a lower peak for thicknesses in the $\sim 1\text{-}5\ \mu\text{m}$ range. This represents the smaller levels of GOP agglomerations that are located at the center of the film.

6.2.4.2 Thermally-Reduced GOP at Concentrations $\geq 0.5\ \text{wt}\%$

The data in Figure 6.9(b) shows that, in this category, the average thickness of the GOP residue increases with distance from the center of the film. This is interesting to note particularly because the film in Figure 6.8(l) looks fairly uniform in its area coverage. Furthermore, this trend is the opposite of the behavior seen in the low concentration films (Figure 6.9(a)). This data reveals that the increase in concentration of the TR GOP appears to reduce the convection-induced migration of platelets to the center of the film. The data also shows the presence of fissures in the film possibly formed by the escape of vaporized fluid (Figure 6.9(b)). The relative-frequency curves for the thickness data in this category also appear to be the combination of two distributions. However, the values of the peaks of these distributions are far enough apart to produce a bi-modal curve (Figure 6.10(b)). The first peak is observed at thicknesses in the $\sim 0.1\text{-}0.3\ \mu\text{m}$ range. The second peak, observed at thicknesses in the $\sim 7\text{-}12\ \mu\text{m}$ range, suggests that the GOP agglomerations involve larger amounts of platelets.

6.2.4.3 Ultrasonically Exfoliated GOP at Concentrations $< 0.5\ \text{wt}\%$

Figure 6.9(c) shows that the residue is both fairly uniform and thin. Except for some tiny agglomerations, the film is virtually indistinguishable from the substrate, at the scale chosen in the scans. The relative frequency curves for the thickness data in this category (Figure 6.10(c)) are characterized by the presence of only a single peak corresponding to a film thickness of $\sim 0.4\text{-}0.5\ \mu\text{m}$.

6.2.4.4 Ultrasonically Exfoliated GOP at Concentrations $\geq 0.5\ \text{wt}\%$

The relative-frequency curves for this category show a peak for film thicknesses in the $1\text{-}5\ \mu\text{m}$ range (Figure 6.10(d)). Not only does this first peak represent a significantly

higher thickness when compared to the other categories, the shape of the curve indicates that significant portions of these films exist at thicknesses in the range of 20-120 μm . These large thicknesses likely correspond to features such as the thicker residues near the center of the droplet due to the vapor bubble pocket (Figure 6.9(d)). There is also evidence of smaller vapor bubble pockets elsewhere in the residue.

6.3 Discussion

Since the GOP colloidal solutions were all seen to have comparable evaporative cooling characteristics (Figure 6.3(a)), the tribological nature of the GOP film at the tool-workpiece interface is not only expected to influence the cutting forces, but it is also expected to be the primary reason for the trends seen in the cutting temperatures. This reality combined with the knowledge obtained from the single-droplet impingement study can be used to identify the potential mechanisms responsible for the machining results. For the purposes of clarity, the cutting force and cutting temperature trends seen for the GOP solutions in Part 1 are summarized in Table 6.2 [139]. Table 6.2 presents the performance of the GOP solutions in terms of their percentage difference relative to the baseline cutting fluid. A positive percentage value in Table 6.2 indicates that the GOP solution has a higher cutting force/temperature than the baseline cutting fluid, whereas a negative percentage value implies the opposite to be the case.

6.3.1 Film-Formation Hypothesis

Figure 6.11(a)-(d) depict the possible nature of the GOP films formed at the tool-workpiece interface for each of the four categories of liquids identified in Sections 6.2.3 and 6.2.4. The films depicted in Figure 6.11 are pictorial representations of the film characteristics observed in Figure 6.9 and Figure 6.10. As seen in Figure 6.11(a), for thermally-reduced GOP at concentrations < 0.5 wt%, the GOP film is non-uniform, which leaves some portions of the tool exposed. These regions correspond to the periphery of the droplet in Figure 6.9(a). The thickness of the film also shows slight variation where the thinner portions (0.1-0.4 μm) and thicker portions (1-5 μm) of the film correspond to the periphery and center of the film in Figure 6.9(a), respectively.

Table 6.2: Lubrication and cooling performance of graphene oxide platelet solutions expressed as a percentage difference relative to the baseline cutting fluid

	Baseling cutting fluid	GOP type	GOP concentration				
			0.1 wt% GOP	0.2 wt% GOP	0.5 wt% GOP	1 wt% GOP	
Average cutting force (N)	5.112±1.229	TR500	50.31%	-5.90%	28.31%	0.48%	
		TR1050	102.77%	10.49%	44.04%	18.22%	
		US	6.29%	-10.80%	22.92%	6.47%	
Average cutting temperature (°C)	11.98±0.95	TR500	-5.82%	-43.61%	-30.41%	^a	
		TR1050	-24.26%	-25.36%	-5.18%	-26.97%	
		US	-51.38%	-33.30%	-25.57%	-2.03%	

^a Data could not be obtained due to destruction of the thermocouple
Data is based on Table 5.2 [139]

This non-uniformity and variation in film thickness is suspected to be the reason behind the high magnitude and variation seen in the cutting forces, especially at 0.1 wt% concentration. At 0.2 wt%, this same film is likely becoming more uniform resulting in a decrease in the cutting force. The cutting temperatures for thermally-reduced GOP at concentrations < 0.5 wt% are seen to track the trends seen in the cutting forces, with 0.2 wt% being the optimal loading.

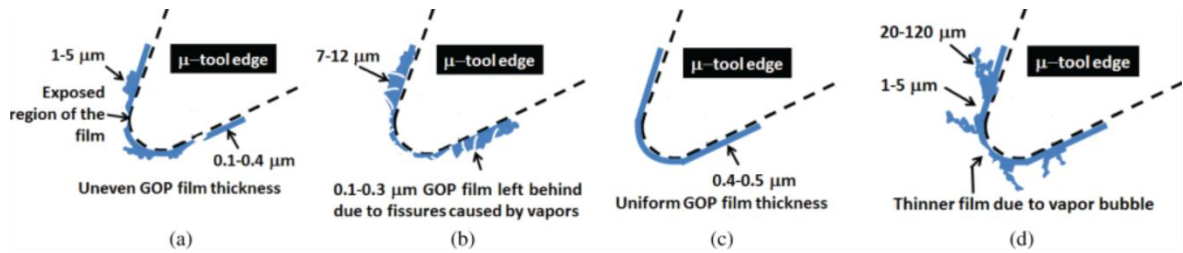


Figure 6.11: Hypothesized GOP film deposition at the tool-workpiece interface. (a) TR GOP at concentrations < 0.5 wt%, (b) TR GOP at concentrations ≥ 0.5 wt%, (c) ultrasonically exfoliated GOP at concentrations < 0.5 wt%, and (d) ultrasonically exfoliated GOP at concentrations ≥ 0.5 wt%

TR GOP at concentrations ≥ 0.5 wt% result in a thicker film (7–12 μm), which also show the presence of fissures due to the escaping of the vapors during evaporation (Figure 6.8(b), Figure 6.9(b), and Figure 6.10(b)). These films are expected to be thicker at regions that are near the periphery of the droplet, as seen in the data in Figure 6.8(b). This could imply that platelets will likely accumulate on the clearance face of a micro-scale tool, which will cause increased rubbing with the machined surface. This could explain the higher forces seen at concentrations ≥ 0.5 wt% for these fluids (Table 6.2). At these concentrations, while the cutting temperatures are still lower than that seen for the baseline cutting fluid, the cooling performance is worse than that seen by the TR GOP at 0.2 wt% loading. This is attributed to the rise in the cutting forces.

The machining results from Part 1 show that the ultrasonically exfoliated platelets at concentrations < 0.5 wt% outperformed all the other solutions, both in cutting temperature and cutting force performance (Table 6.2). Given the trends seen in Figure 6.8(c) and Figure 6.9(c), the GOP film formed at the tool-workpiece is expected to be only 0.4–0.5 μm thick and also uniform in nature. This would imply that the film is likely to wrap around the cutting edge as shown in Figure 6.10 (c) and this thin, uniform film could be the reason for the low cutting forces and temperatures observed with this solution.

The machining benefits of ultrasonically exfoliated GOP is seen to disappear at concentrations ≥ 0.5 wt%. At those loadings, the film is characterized by the presence of relatively thin and extremely thick regions due to boiling of the liquid (Figure 6.8 (a)). The bursting of vapor bubbles exposes the underlying film which is 1–5 μm thick, but also leaves large craters that have thicknesses of up to 120 μm . This sort of a non-uniform film with widely varying thickness could be the reason for the increased cutting forces. In addition, the fact that vapor is trapped by the graphene film makes it likely that the escaping vapor is superheated. This combined with the increased cutting forces is probably responsible for the higher cutting temperature seen with these fluids.

6.3.2 Experimental Validation

The hypotheses presented in Figure 6.11(a)-(d) regarding the nature of the film formed on the cutting tool are based on the film-formation behaviors seen in the single-droplet experiments performed on a heated flat substrate (Figure 6.8 and Figure 6.9). It should be noted here that experimental validation of these inferences is limited by the fact that in-situ observation of the film formation is not possible during the machining tests. Furthermore, observing the cutting edge after the completion of the cut is futile since the platelet film is usually destroyed by that time. The next best option is to deliver the GOP solutions on a heated cutting tool edge and to observe the subsequent film formed.

The EFD setup in Figure 6.1 was used to jet the four categories of the GOP solutions identified in Figure 6.11(a)-(d), on to a tool edge heated to 100°C. Figure 6.12(a)-(e) present the digital images of the clearance face and rake face of the turning tool, as seen at the end of the experiment. In these images, the cutting edge is seen at the intersection of the clearance and the rake face. Figure 6.12 (a) depicts the baseline image of the dry tool, whereas Figure 6.12 (b)-(e) depict the tool images in the presence of the GOP films. In Figure 6.12(b)-(e), the presence of the GOP film is indicated by the black gradation that is overlaid on the baseline of the dry tool seen in Figure 6.12 (a).

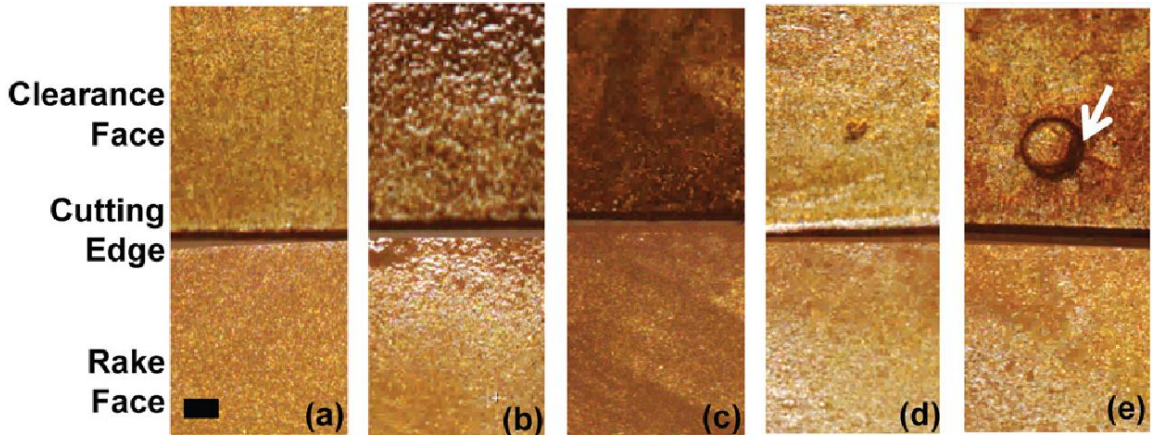


Figure 6.12: Digital images of the turning tool showing GOP film formation at 100°C (scale bar = 120 μm): (a) dry tool—no cutting fluid, (b)TRGOP < 0.5 wt%, (c)TR GOP \geq 0.5 wt%, (d)USGOP < 0.5 wt%, and (e)USGOP \geq 0.5 wt%

The TR GOP at concentration <0.5 wt% are seen to form an uneven film as indicated by the black gradation in Figure 6.12 (b). At concentrations \geq 0.5 wt%, the films formed by TR GOP are more thick and uniform on both faces of the tool (Figure 6.12 (c)). The US GOP at concentrations <0.5 wt% appear to form the thinnest and most uniform film among all the cases (Figure 6.12 (d)). This is evidenced by the fact that the GOP film is barely distinguishable when compared to the image of the dry tool (Figure 6.12 (a)). Finally, the US GOP at concentrations \geq 0.5 wt% show evidence of vapor bubble-related thicker films (denoted by an arrow in Figure 6.12 (e)). These differences seen in the nature of the GOP films closely mirror the hypotheses presented in Figure 6.11. While this experiment does not account for the extreme contact pressures encountered in machining, it provides some preliminary insight into the formation of the GOP film on the cutting tool. It should also be noted here that the processing chemistry (in terms of functional chemical groups attached on the GOP) and geometrical attributes (shape and size) of the platelets are critical factors that affect the nature of the films that are generated. These factors are also expected to influence the critical transition seen at concentrations \geq 0.5 wt% (Figure 6.8 and Figure 6.9). The development of a multiscale computational fluid dynamics model that accounts for the chemistry/geometry of the platelets and its interaction with the cutting fluid suspensions under high pressure and temperature conditions is likely to shed more light on these specific mechanisms.

6.4 Summary

The following specific conclusions can be drawn from the results of this single-droplet impingement study of graphene oxide colloidal solutions:

1. The temperature profiles and the high-speed images of the graphene oxide colloidal droplets show three distinct regimes, *viz.*, the spreading regime where the droplet is deposited, the pinning regime where convection heating causes the loss of droplet volume, and the receding regime where the droplet evaporates completely.
2. The absolute minimum temperature drop seen in the spreading regime and the average temperature seen in the pinning regime are similar for all GOP solutions, indicating that the evaporative cooling characteristics are similar across the liquids.
3. At concentrations <0.5 wt%, all GOP solutions have a shorter total lifetime when compared to the baseline liquid. At concentrations ≥ 0.5 wt%, the ultrasonically exfoliated GOP has the longest overall droplet lifetime with their receding phase having the longest duration.
4. The data from the pinning regime show that, when deposited on a heated substrate, the GOP solutions demonstrate a reduced wettability, with the ultrasonically exfoliated GOP solutions being the most hydrophobic. The presence of the GOP is also seen to reduce the evaporation-induced decay rate of the droplet height and contact angle.
5. For TR GOP at concentrations <0.5 wt%, as the droplet evaporates in the receding regime, a small region of high convection is noticeable at the droplet boundary. This results in increased film thickness at the center of the droplet (1–5 μm) compared to the periphery (0.1–0.3 μm). This type of the film is hypothesized to be the reason for the higher magnitudes and variation in the cutting forces and temperatures.
6. For TR GOP at concentrations ≥ 0.5 wt%, the higher concentration of GOP is seen to result in distributed micro-boiling within the droplet. This ultimately forms a 7–12 μm thick film with fissures formed by escaping vapor. These thicker films are

hypothesized to the reason behind the increase in the cutting force, possibly due to the rubbing along the clearance face.

7. Ultrasonically exfoliated GOP at concentrations <0.5 wt% show evidence of nucleation-induced formation of the GOP film on the substrate. The film is not only uniform but is also the thinnest ($0.4\text{--}0.5$ μm) among all the GOP solutions. These thin and uniform films are hypothesized to be responsible for the superior machining performance of these colloidal solutions.
8. At concentrations ≥ 0.5 wt%, the ultrasonically exfoliated GOP solutions are seen to lose their advantage. The GOP film left behind on the substrate is characterized by the bursting of vapor bubbles. The film around these regions is significantly thicker ($20\text{--}120$ μm) than the remaining portion of the film ($1\text{--}5$ μm). This thick and uneven film is hypothesized to be responsible for the deterioration of the cutting fluid performance.
9. Rather than the bulk properties (*viz.*, thermal conductivity and dynamic viscosity) of the GOP colloidal suspensions, a more important criterion dictating the machining performance of the GOP colloidal solutions appears to be its ability to form submicron thick, uniform graphene oxide films upon evaporation of the carrier fluid. The findings of this study reveal that the characterization of the residual graphene oxide film left behind on a heated substrate may be an efficient technique to evaluate different graphene oxide colloidal solutions for cutting fluids applications in micro-machining.

7. CHEMICAL WEAR MITIGATION MECHANISMS OF GRAPHENE DURING DIAMOND CUTTING OF STEEL

The research presented in this chapter used molecular dynamics (MD) simulations to investigate the wear mitigation mechanisms that are active during the diamond cutting of steel in the presence of graphene platelets. A modified embedded atom method (MEAM) force field was first evaluated for its ability to accurately satisfy three qualifying criteria, *viz.*, 1) the structural parameters of iron, diamond and graphite; 2) temperature-driven graphitization of diamond; and 3) catalyzed graphitization of diamond in the presence of iron. This force field was then used to simulate nanometric diamond cutting of steel in the presence of graphene platelets. The tool wear trends predicted by the simulations were found to be comparable to the findings of Smith *et al.* [25]. The graphene platelets were seen to serve as a physical barrier, protecting the tool cutting edge, and also as a sacrificial source for carbon transfer into the workpiece. Other mechanisms, such as platelet cleaving and interlayer sliding, were also observed.

The remainder of this chapter is organized as follows: Section 7.1 summarizes the experimental work of Smith *et al.* [25], which prompted this MD investigation. Section 7.2 provides the rationale for choosing an appropriate interatomic force field and discusses the results from calibration tests evaluating the choice. It also describes the frame work for the cutting simulations. Section 7.3 presents the results from the cutting simulations. Section 7.4 compares the simulation findings to the experimental results of Smith *et al.* [25] and also presents a discussion on the wear mitigation mechanisms. Finally, Section 7.5 summarizes the specific findings of this work.

7.1 Review of Experimental Findings

This section briefly reviews the key findings from the experimental study of Smith *et al.* [25], where graphene platelets were introduced into the workzone during the diamond cutting of low-carbon steel. Table 7.1 provides a summary of the micro-scale cutting conditions and tool geometry used for their experiments. In this study, the

This chapter has been submitted to: B. Chu, Y. Shi, and J. Samuel, "Mitigation of chemical wear by graphene platelets during diamond cutting of steel," *Carbon*.

platelets were delivered in the form of a colloidal dispersion in Castrol Clearedge 6519 semi-synthetic cutting fluid.

Table 7.1: Summary of machining conditions in Smith *et al.* [25]

Workpiece	3mm diameter, AISI 12L14 low-carbon steel rod
Tool	<ul style="list-style-type: none"> • Manufacturer: Sumitomo Inc. • Tool insert #: NF-CCGA21.50.5 • Material: polycrystalline diamond (PCD) • Geometry details: right-hand, 7° relief angle, 55° nose angle, 0.0075in nose radius
Cutting velocity	3m/s
Depth-of-cut	<ul style="list-style-type: none"> • 100µm(radial) • 5µm/revolution (axial)
Cutting Conditions	<ol style="list-style-type: none"> 1. Dry- no cutting fluid 2. Baseline cutting fluid: Castrol Clearedge 6519 semi-synthetic (12.5% dilution) 3. Baseline cutting fluid + 0.2 wt% graphene oxide platelets

Two measures were used to determine the extent of the diamond tool wear. The first was optical profilometry of the tool surface after the completion of the cut. This data was used to construct height maps of the worn tools, shown in Figure 7.1(a)-(c). These

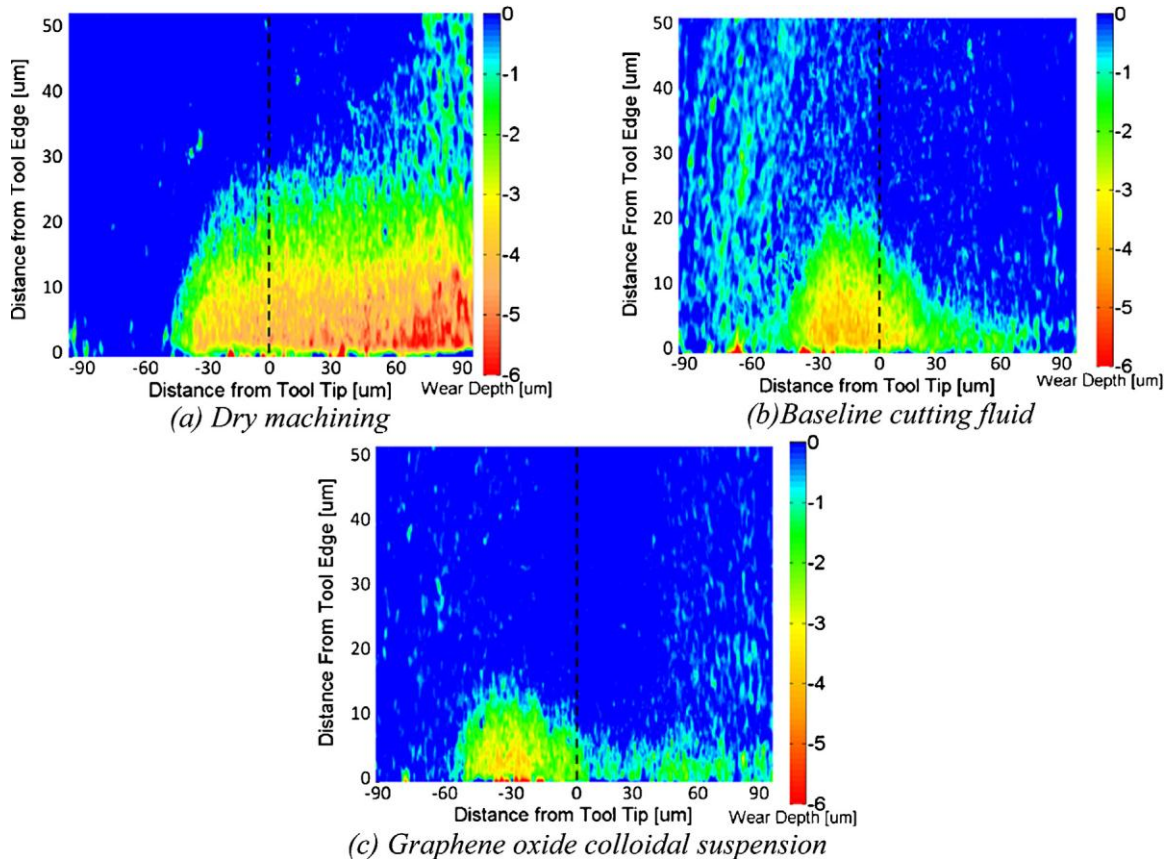


Figure 7.1: Volumetric tool wear patterns seen in region A-B-C-D. (Note: the dotted line corresponds to the centerline of the tool and the region to the left and right of the centerline are the leading and trailing zones, respectively)

results showed that the presence of graphene platelets led to a ~74 % reduction in wear compared to the dry cut and ~32% reduction compared to the cut using the baseline cutting fluid. The second measure involved X-ray photoelectron spectroscopy of the workpiece (XPS) to reveal peaks in the binding energy distribution curve corresponding to the iron-carbon bond involved in carbidization. The percentage contribution of the carbide peak was seen to be 13%, 9% and 6% for the dry machining, baseline cutting fluid and graphene colloidal suspensions, respectively. The lower formation of carbides was correlated to the trends seen in the tool wear under the same conditions.

The cutting temperature and cutting force measurements for the baseline cutting fluid were found to be comparable to those for the graphene colloidal suspensions. This meant that the wear reduction in the presence of graphene could not be attributed to lower cutting temperatures or lower cutting forces. Therefore, two alternate mechanisms were hypothesized to explain the tool wear trend. The first was that the graphene platelets potentially serve as a physical barrier around the cutting edge, and the second was that the carbon in the platelet was affecting the chemical reaction rate. However, these specific mechanisms have not yet been confirmed.

7.2 Interatomic Force Fields and Molecular Dynamics Simulations

This section will first discuss the selection and evaluation of an appropriate interatomic force field to capture the tool wear mitigation phenomenon during diamond machining of steel, followed by the details of the MD nanometric cutting simulation.

7.2.1 Selection of Interatomic Force Field

In order to accurately model the dynamics of the cutting zone, the interatomic force field must satisfy three specific criteria. First, it must be able to model metallic elements (iron), non-metallic elements (carbon in graphite and diamond allotropes), as well as compounds/alloys (more specifically steel, which is comprised of interstitial carbon in iron, and iron carbides). Second, the force field must be able to describe the temperature-driven graphitization of diamond and third, the potential must be capable of capturing the catalyzed graphitization of diamond in the presence of iron. With these criteria in mind, a MEAM force field was chosen [140-141].

In MEAM force fields, the total energy of the system (E) is given by:

$$E = \sum_i \left\{ F_i(\bar{\rho}_i) + \frac{1}{2} \sum_{i \neq j} \phi_{ij}(\mathbf{R}_{ij}) \right\} \quad (1)$$

where F_i is the energy needed to embed atom i into the background electron density, $\bar{\rho}_i$, and ϕ_{ij} is the pair interaction term between atoms separated by the vector \mathbf{R}_{ij} . The electron density and pair interaction calculation are subject to a three-body screening function. For more details, see Refs. [140-142].

The specific parameters for the MEAM force fields used in this study were presented in Liyanage *et al.* [143] and are archived at the National Institute of Standards and Technology (NIST) Interatomic Potentials Repository Project website [144]. These parameters describe only iron (Fe) and carbon (C) and are able to predict the single element structures of these two elements fairly well. An exception is the interlayer spacing of C in the graphite allotrope due to the inability of MEAM to describe vdW forces. It is also capable of reproducing the properties of both cementite (Fe₃C) and interstitial C in body centered cubic (BCC) iron. For the remainder of this chapter, the force field parameters used here will be referred to as the Liyanage parameters.

7.2.2 Force Field Evaluation

The MD simulations performed for this study were carried out using the Large-scale Atomic/Molecular Massively Parallel Simulator* (LAMMPS) maintained by Sandia National Labs [145]. Analysis and visualization was performed in part with the OVITO† software [146]. Simulations were performed on an in-house Beowulf cluster with Intel CPUs. In order to confirm that the Liyanage parameters are capable of meeting the criteria provided in Section 3.1, three sets of benchmarking simulations were performed. The first was to confirm that the structural parameters of the materials being simulated matched the results reported in literature. The second was to confirm that temperature-driven diamond graphitization can be simulated and finally, the third set was to examine the catalytic effect of iron on the graphitization of diamond. The canonical (NVT) ensemble was used for simulating all the benchmarking simulations.

* Can be found at <http://lammmps.sandia.gov>

† Can be found at <http://ovito.org/>

7.2.2.1 Structural Parameters

Equilibration simulations were performed using the Liyanage parameters on infinite bulks of diamond, graphite, and BCC iron at 300K. These simulations were conducted to determine the equilibrium lattice constants and to confirm the cohesive energy values. The results from these structure evaluation simulations are contrasted against the published values of Liyanage *et al.* [143] in Table 7.2. The negligible differences between the simulated values in this study and the values from Liyanage *et al.* [143] can be attributed to differences in computational hardware. A special mention has to be made here for the results of carbon in the graphite allotrope, whose commonly accepted values for its lattice constants c and a are 2.46\AA and 6.709\AA , respectively. It can be seen from Table 7.2 that while the simulated values for graphite match those of Liyanage *et al.* [143], the Liyanage parameters are unable to accurately capture the vdW interactions present in graphite. Despite this shortcoming, it is safe to proceed with the Liyanage parameters since the weak vdW interactions in graphite are not expected to play a significant role under the high contact pressure conditions that exist between the cutting tool and the workpiece.

Table 7.2: Equilibration simulation results compared to published values

Variable	Iron (BCC)	Diamond	Graphite
Simulated cohesive energy, E_c (eV/atom)	4.28	7.32	7.33
Published cohesive energy, E_c (eV/atom) *	4.28	7.37	7.37
Simulated lattice constant, a (\AA)	2.851	3.582	2.558
Published lattice constant, a (\AA) *	2.86	3.567	2.53
Simulated lattice constant, c (\AA)			8.333
Published lattice constant, c (\AA) *			8.476

*Published values from Liyanage *et al.*[143]

7.2.2.2 Temperature-driven Graphitization

A second set of evaluation simulations was performed to confirm the capability of the force field to capture temperature-driven graphitization of diamond. In this scenario, two spherical diamond nano-particles, with radii of ~ 2.5 nm, were simulated. One particle was held at room temperature (300K) for ~ 1 ns. The second particle was heated from 300K to 2000K over a time period of 10ps. It was then held at 2000K for 1ns and subsequently cooled back down to 300K in 10ps. The nano-particle was allowed to relax

at room temperature again for 4ps. Images of cross-sectional slices of these two cases are shown for both the initial (Figure 7.2(a)) and final configurations (Figure 7.2(b)-(c)).

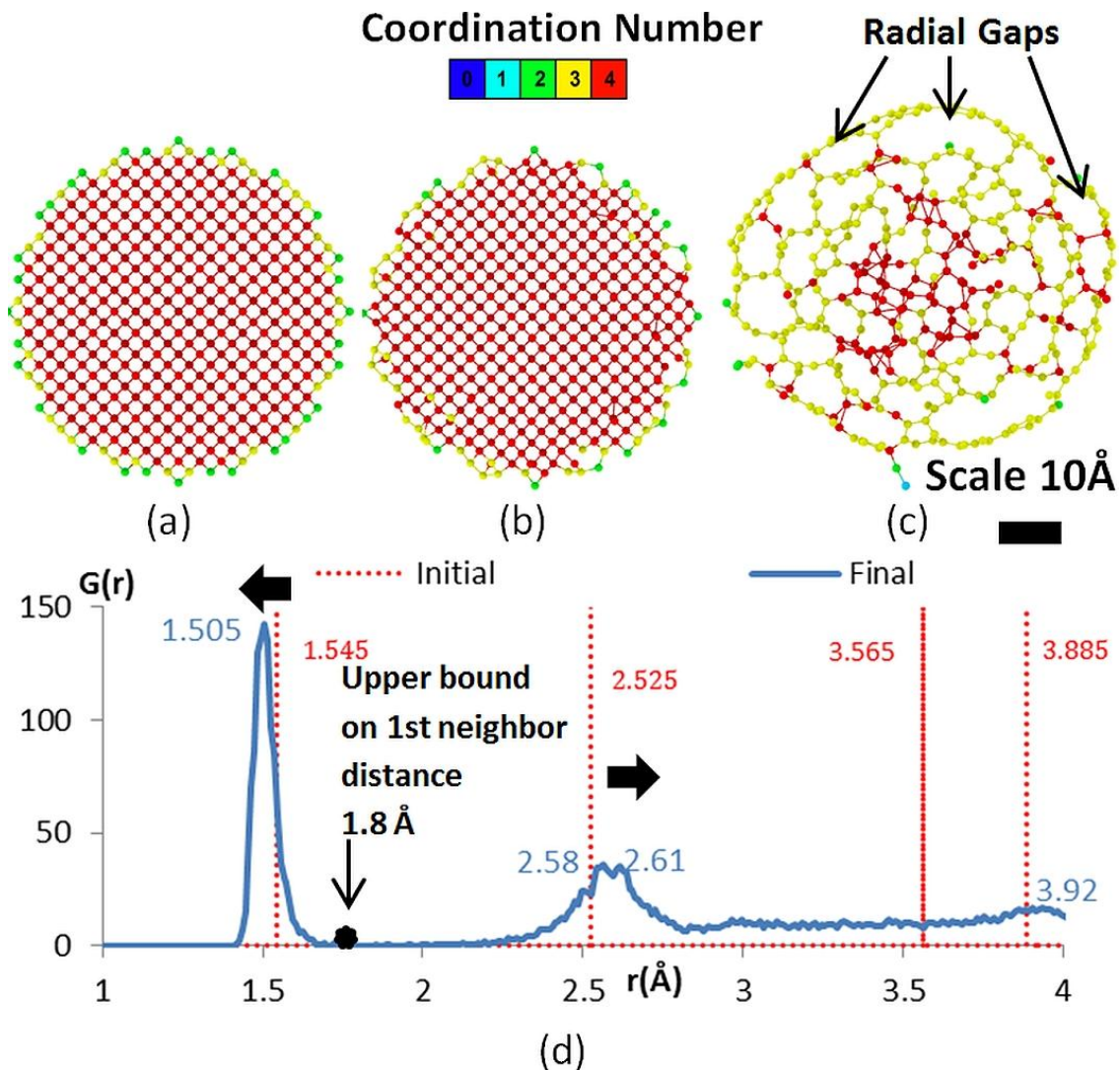


Figure 7.2: Results of temperature-driven graphitization benchmarking simulation (a) Initial cross-sectional slice (2\AA thickness) of diamond nano-particle in both cases (b) Final cross-sectional slice of diamond nano-particle maintained at 300K. (c) Final cross sectional slice of diamond nano-particle heated to 2000K. (Note: Atom radius in (a)-(c) is $\frac{1}{2}$ the atomic radius of carbon). (d) Radial distribution function for diamond nano-particle heated to 2000K. The red dotted line represents the initial configuration from (a) and the four nearest neighbor distances in the diamond lattice. The blue line represents the final configuration of the particle after heating at 2000K scenario in (c). Coordination and bond cutoff is 1.8\AA , indicated by the black dot in (d)

In Figure 7.2(a)-(c), the atoms are colored according to their coordination number. Here the coordination number of any given atom is defined as the count of other atoms within a cutoff distance of 1.8\AA , which is the upper bound for the first neighbor distance for carbon, as shown in Figure 7.2(d). In diamond, carbon atoms are positioned in a

tetrahedral arrangement (sp^3 hybridization), with four neighbors, so their coordination number is 4. In graphite, the carbon atoms are bonded to three others (sp^2 hybridization), resulting in a coordination number of 3. Surface atoms have coordination numbers ≤ 3 . For both the initial cross-section (Figure 7.2(a)) and the final cross-section of the diamond nano-particle held at the room temperature of 300K (Figure 7.2(b)), the atoms are mostly 4-coordinated. On the other hand, the final cross-section of the diamond nano-particle heated to 2000K is mostly 3-coordinated atoms (Figure 7.2(c)). This clearly indicates graphitization [87]. Furthermore, the radial gaps present in Figure 7.2(c) also suggest the occurrence of graphitization, since these are characteristic of graphite nano-onions formed during the graphitization of diamond nano-particles [147].

Evidence of the graphitization can also be seen in the radial distribution function (Figure 7.2(d)), which shows the distribution of neighbor distances. In Figure 7.2(a), the dotted red line shows the distribution of the ideal diamond lattice with peaks at the first four nearest neighbors. From left to right, these peaks correspond to $\sqrt{3}/4, \sqrt{2}/2, 1,$ and $\sqrt{19}/4$ times the diamond lattice constant, 3.567\AA [148]. As the nano-particle graphitizes, the peaks shift towards the solid blue line distribution (indicated by the arrows), which corresponds to a graphitic structure. The first two peaks, at 1.505\AA and $\sim 2.6\text{\AA}$, represent the 1st nearest neighbor and 2nd nearest neighbor separation distances in the simulated graphite lattice.

7.2.2.3 Catalytic Effect of Iron on Graphitization

Further evaluation of the force field was performed by examining the catalyzing effect of iron on the sp^3 - sp^2 transition. For this test, first, the diamond nano-particle heating scenario described in Section 7.2.2.2 was repeated but now at a maximum temperature of 1000K (Figure 7.3(a)). This was contrasted against a similar diamond nano-particle heating scenario (1000K), but with an iron wall enveloping one hemisphere of the particle (Figure 7.3(b)). This iron wall was placed with its (100) surface facing outwards and with an initial radial separation of 3\AA between the iron wall and the outer surface of the diamond nano-particle. The iron was simulated at 300K with a layer of fixed atoms on the edges of the simulation box. Other than the presence of the

iron wall, the simulation with the iron wall proceeded in the same way as that without the iron wall.

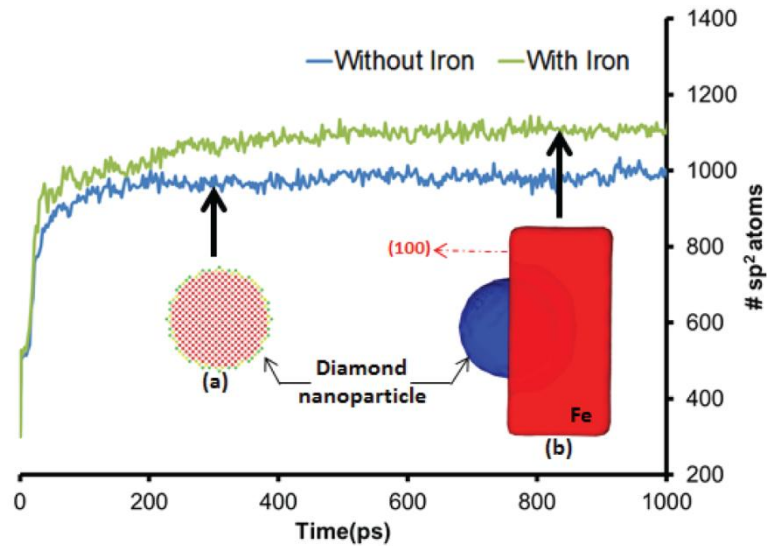


Figure 7.3: Number of sp^2 hybridized atoms in the nano-particles heated to 1000K showing catalytic effect of iron. Blue line comes from the scenario shown in inset (a). Green line shows data from scenario with particle half immersed in iron, shown in inset (b)

The plot in Figure 7.3 shows the number of sp^2 hybridized atoms in the diamond nano-particle over the duration of the two simulations. As expected, the count of sp^2 atoms increases from ~ 300 at the beginning of the simulations to >1000 at the end of the simulations, signifying the transformation of the carbon atoms from 4-coordinated to 3-coordinated at elevated temperature. The final sp^2 count for the case without the iron wall (Figure 7.3(a)) and in the presence of the iron wall (Figure 7.3(b)) is 1004 and 1104, respectively. The $\sim 10\%$ increase seen in the final sp^2 count in the presence of iron indicates the presence of a catalytic effect.

Given the successful benchmarking of the Liyanage parameters, it can now be used to perform the nanometric cutting simulations.

7.2.3 Nanometric Cutting Simulation

The nanometric cutting simulations presented in this chapter make the following simplifications:

Simplification 1: Recent experiments by Chu *et al.* [149] have shown that the carrier fluid evaporates upon contact with the cutting zone, leaving

behind a film of graphene on the tool. During the cutting operation, this graphene film was seen to have a much larger impact on the cooling and lubrication performance than the carrier fluid. Based on this finding it is assumed that the fluid primarily serves to deliver graphene platelets into the cutting zone and has negligible effects on the specific chemical wear mitigation mechanisms triggered by the platelets themselves. Hence, the cutting fluid is not explicitly modeled in the MD simulations. Instead, its effects are captured by the formation of a uniform graphene layer wrapped around the cutting edge of the tool.

Simplification 2: Given the computationally intensive nature of MD simulations, the cutting parameters, i.e., depth of cut, tool geometry, cutting velocity, and length of the cut, are scaled to ensure a reasonable computational time. This is a common practice for MD simulation models for cutting [86].

Simplification 3: Without extensive treatment, trace impurities are typically present in the bulks and surfaces of workpiece and tool materials. The edges of the graphene sheets can also contain impurities such as carboxyl and hydroxyl groups [29], thereby imparting them the chemical signature of graphene oxide platelets (as was the case in Smith *et al.* [25]). However, given the limitations of the MEAM force field, all materials in the MD simulations are modeled without impurities, i.e., 1) non-carbon alloying elements in steel are not modeled; 2) the hydrogen/oxygen elements are not modeled for the platelets; and 3) a single crystal diamond tool as opposed to the polycrystalline diamond tool in Smith *et al.* [25]. The consequences of this simplification may include prediction inaccuracies in the formation of local corrosion products, such as iron oxides, the formation of metal-carbon-oxygen complexes [104], and the modification of the local material properties of steel by its alloying materials, all of which can have an impact on the graphitization reaction.

Given these simplifications, the model differs from the experimental conditions of Smith *et al.* [25] outline in Table 7.1. Therefore, while the model is expected to provide insight into the chemical wear mitigation mechanisms, it is best to only qualitatively compare the simulation results to the tool wear trends reported by Smith *et al.* [25]. Using qualitative comparisons to experimental results is a common practice to validate MD simulations [86].

The geometric and cutting parameters used in the simulations are listed in Table 7.3 and also presented in a schematic view in Figure 7.4. The cutting simulation is orthogonal, single point, and periodic in the Z-direction. The workpiece is simulated as iron in a BCC lattice. Carbon is randomly seeded in the iron workpiece, as shown in Figure 7.4, at 0.1% concentration by mass. The system is then subjected to an energy-minimization process. After minimization, the carbon tends to occupy the octahedral interstitial sites. The tool is carbon in a diamond lattice. The rake face of the tool is chosen to be the {100} plane of the diamond, which is a common choice in single crystal diamond tooling [150].

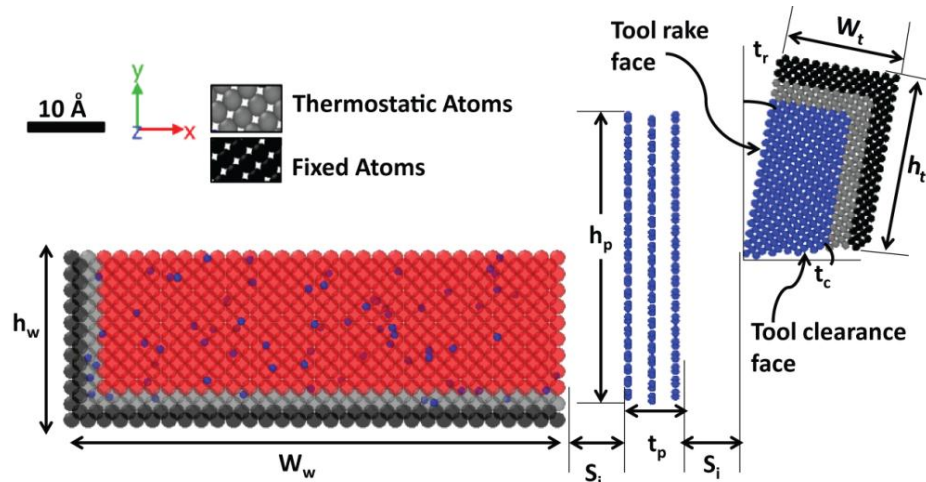


Figure 7.4: Initial configuration of workpiece, tool, and platelet in MD simulation (when present). Workpiece iron atoms are semi-transparent to show carbon seeding

Three simulations were performed with platelets of 0, 1, and 3 layer thickness. The graphite in the multi-layer platelet case was in the alpha phase. In the initial configuration, the platelet is placed such that its center of mass is collinear with the top surface of the workpiece. It is also oriented such that the in-plane direction is normal to the cutting velocity vector. This initial configuration of the platelets, coupled with the

Table 7.3: Geometric and cutting parameters for molecular dynamics simulations

Variable	Description	Value
w_w	length of workpiece	85.53 Å
h_w	height of workpiece	28.51 Å
w_t	width of tool	24.49 Å
h_t	height of tool	35.82 Å
h_p	height of platelet	51.16 Å
t_p	thickness of platelet	0 Å (no platelet), 4.17 Å (1 layer), 12.50 Å (3 layers)
s_i	initial spacing	10 Å
t_r	rake angle	10°
t_c	clearance angle	5°
	depth of cut	10 Å
	cutting speed	0.25 Å/ps
	workpiece carbon concentration	0.1wt%
	Timestep	0.1fs
	thermostat atom temperature	300K

geometry of the tool (Table 7.3), ensures the formation of a uniform film of the platelet around the tool edge, during the cutting simulation (Refer Section 7.3 for details).

The cut proceeds along the $\langle 100 \rangle$ direction of the workpiece at a cutting speed of 0.25 Å/ps (25m/s), which is approximately five times the maximum recommended speed when cutting steel with carbide tools [151]. This is a common strategy in molecular dynamics to cut down on computational time, but has the added benefit of inducing aggressive wear. Under conventional experimental machining conditions, the wear rates may be expected to be lower than that predicted by the simulation.

In order to fix the workpiece in place during the simulation, a layer of fixed atoms, which is one lattice unit thick, is defined at the edges of the workpiece and tool, as shown in black in Figure 7.4. Another layer adjacent to the fixed layer, also one lattice unit thick, is set as thermostat atoms (shown in grey in Figure 7.4). The thermostat atoms are needed to dissipate heat generated during cutting [86]. They are simulated using the canonical ensemble (NVT) at 300K with a damping period of 100 timesteps. All atoms not in the fixed or thermostat layers are considered bulk. Table 7.4 presents the simulation details from each of the three scenarios. Each simulation followed the sequence of steps listed below:

Step 1: The force and velocity values for fixed atoms are set to 0.

Step 2: Positions of atoms are optimized using the iterative energy minimization method built into LAMMPS.

Step 3: Bulk and thermostat atoms are relaxed at 300K using the NVT ensemble for 2 picoseconds (20,000 timesteps).

Step 4: The tool and platelet are rigidly moved closer to the workpiece to a 5Å separation distance. This is done to cut down on simulation steps before contact.

Step 5: Bulk atoms are set to use the micro-canonical ensemble (NVE) and the fixed boundary atoms of the tool are prescribed to translate at 0.25 Å/ps into the workpiece. This continues for eight days of computation time, after which the analysis is performed.

Table 7.4: Molecular dynamics cutting simulation details

Description	0 layer	1 layer	3layers
Simulated Frames	2,400,000	2,567,000	2,900,000
Cut Duration (ps)	200	200	200
Cut Length (Å)	50	50	50
Total Iron Atoms	16,100	16,100	16,100
Total Tool Atoms	8,920	8,960	8,920
Total Platelet Atoms	0	1,288	3,864

7.3 Simulation Results

Figure 7.5(a)-(f) show snapshots of the three simulations taken at both the middle and at the end of the cut. The platelet is primarily seen to act as a built-up edge (BUE) [152], significantly altering the shape of the cutting edge at the simulated length scale. This leads to a change in the effective cutting depth, which increases from the specified 10Å value in the absence of a platelet (Figure 7.5(b)) to 16Å, for the 3-layered platelet scenario (Figure 7.5(f)). The effective rake angle of the tool also changes from a value of +10° in the absence of a platelet (Figure 7.5(b)) to -4° for the 3-layered platelet scenario (Figure 7.5(f)). The surface roughness (R_a) of the resulting machined surface was measured digitally to be 0.933Å, 2.000Å, and 2.423Å, respectively, for the 0, 1, and 3 layer scenarios.

Table 7.5 presents the average cutting conditions experienced by the tool atoms over the last 50ps of the simulation. Here, the cutting and thrust forces were obtained by summing the forces acting on each atom in the tool. Temperature was similarly found by calculating the mean kinetic energy of atoms in the tool and relating it to temperature. As expected, the cutting conditions change significantly between the three scenarios due

to the large relative size of the platelet BUE. The increase in cutting temperatures across the three simulations correlates well with the corresponding increase in the volume of material removed due to the larger effective cutting depth. The changes in cutting forces are more complicated. Adding a single layered platelet increases both the cutting and

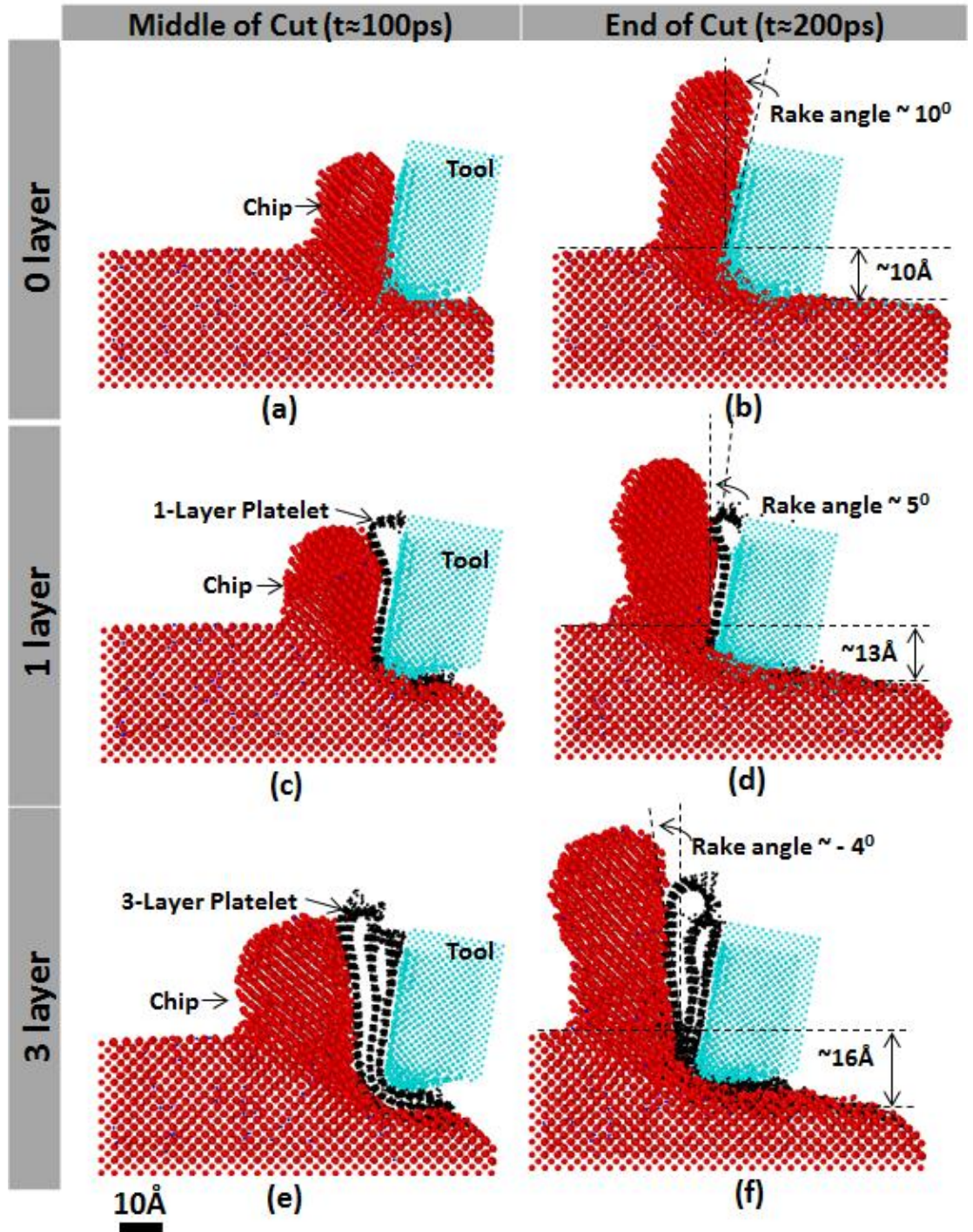


Figure 7.5: Screenshots of simulation progress showing workpiece (red), tool (light blue), and graphene platelet (black). (Note: Atomic radius is drawn at $\frac{1}{2}$ scale)

thrust forces, which can also be attributed to the increase in the effective material removal volume. The reduction in the effective rake angle from $+10^\circ$ in the absence of a platelet (Figure 7.5(b)) to $+5^\circ$ (Figure 7.5(d)) is also a contributing factor to this trend. Between the 1 and 3 layer scenarios, the thrust force is seen to decrease slightly despite the increase in the effective depth of cut from 13 \AA to 16 \AA . This trend in the thrust force can be explained by a decrease in friction due to the phenomenon of interlayer sliding in the graphene platelets, (discussed ahead in Section 7.4.2.3).

Table 7.5: Cutting conditions measured and averaged on the tool over $150\text{ps} < t \leq 200\text{ps}$

Description	0 layer	1 layer	3layers
Cutting Force (eV/Å)	95 ± 31	113 ± 45	114 ± 52
Thrust Force (eV/Å)	93 ± 37	147 ± 41	138 ± 38
Temperature (K)	732 ± 31	858 ± 36	926 ± 41

7.3.1 Wear and Graphitization Analysis

Upon completion of the simulation runs, a coordination analysis, similar to that discussed in Section 7.2.2, was conducted on the carbon atoms. Figure 7.6(a)-(c) depict the results from this analysis for each of the three scenarios. As seen in the figures, the graphitization of the outer edge of the cutting tool is common to all the three cases, illustrated by the regions of yellow and green colored atoms around the edge of the tool (Figure 7.6(a)-(c)). Another commonality between the three scenarios is the presence of 1-coordinated atoms on the clearance face of the tool. These atoms are present on the rake face only in the no platelet scenario (Figure 7.6(a)), but absent when a platelet is present (Figure 7.6(b)-(c)). This suggests that the platelet creates a physical barrier on the rake face, effectively reducing graphitization. Compared to the other scenarios, the extent of 1-coordinated carbon atoms on the clearance face of the tool in the 3-layer scenario is much smaller (Figure 7.6(c)).

The discernible change in the edge radius of the tools across Figure 7.6(a)-(c), provides a quick visual estimate of the amount of wear experienced by the tool in each scenario. It should be noted here that in Figure 7.6(a)-(c), although bonds are drawn between the platelet and tool, these bonds are not counted in the above sets of tool atoms. For a more quantitative time-varying characterization, coordination analysis is performed on the tool and the following sets of atoms are identified:

- T_0 : Total number of tool atoms at time $t=0$
- D_0 : Total number of 4-coordinated (sp^3) tool carbon atoms at time $t=0$
- $S_0 = T_0 - D_0$: Total number of tool surface atoms at time $t=0$
- $D(t)$: Total number of 4-coordinated (sp^3) tool carbon atoms at time t . These atoms represent the ungraphitized tool and are located at the core of the tool, away from the cutting surface (Figure 7.6(a)-(c))
- $SG(t)$: Total carbon atoms that are either on the tool surface or have been graphitized at time t . This set is comprised of the tool atoms that are connected directly to the atoms in $D(t)$ through bonds, as defined by the presence of an atom within the cut off distance of 1.8 \AA .
- $T(t) = D(t) + SG(t)$: Total number of unworn tool atoms at time t

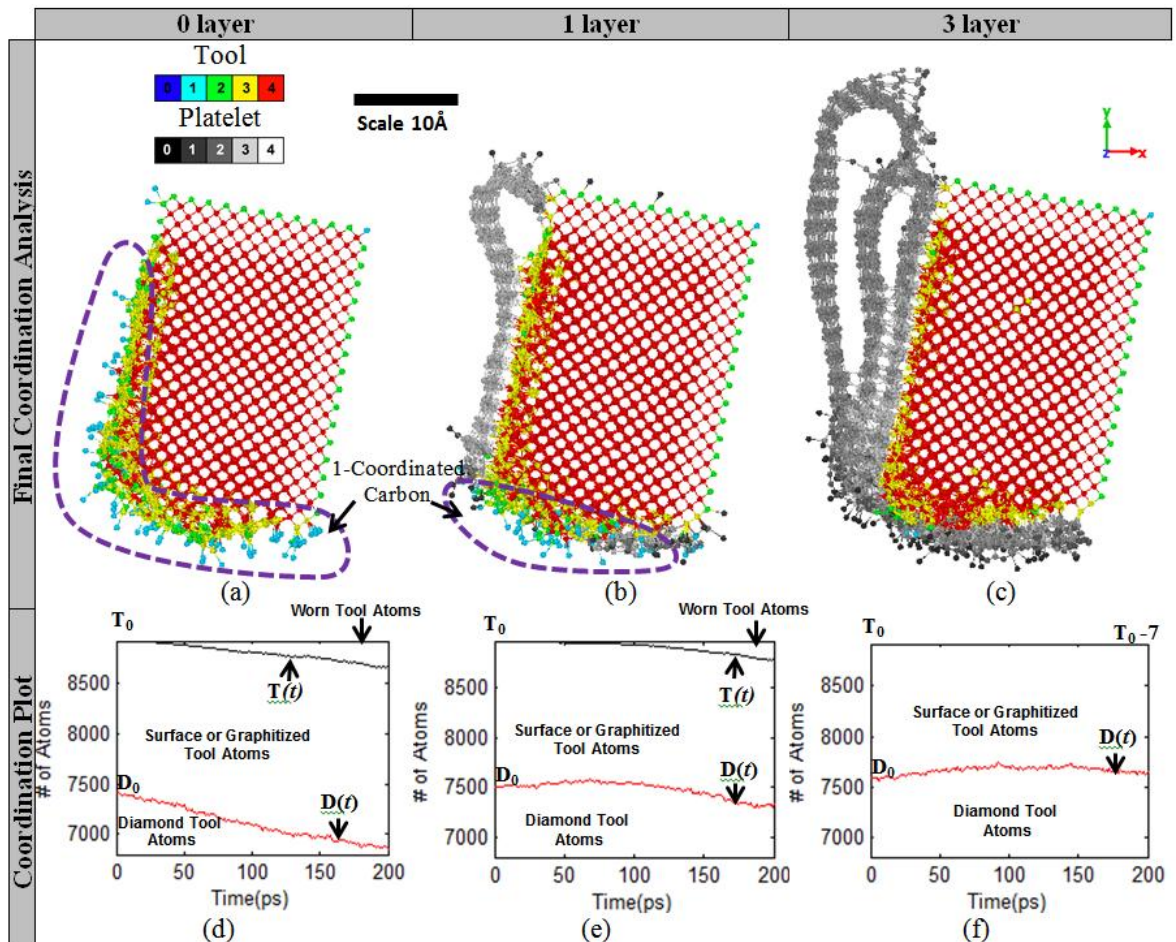


Figure 7.6: Final unworn tool and platelet configurations with coordination analysis. (a-c): Monochrome atoms were originally part of the platelet. Brightly-colored atoms were originally part of the tool. Bonds are drawn between carbon atoms with a cutoff distance of 1.8 \AA . Although bonds are drawn between the platelet and tool, these bonds are not counted in calculating wear and graphitization of the tool. (d-f): Time- dependent variation in the number of worn tool atoms

The time-dependent variation in the number of worn tool atoms can now be computed as $\mathbf{T}_0 - \mathbf{T}(t)$ and is plotted in Figure 7.6(d)-(f). The tool wear values at the end of the simulations ($t=200$ ps) are seen to be 263 atoms, 173 atoms and 7 atoms, respectively, for the cases with 0, 1 and 3 layers of graphene platelets (Figure 7.6(d)-(f)). Even with the presence of a single layer of graphene, the tool wear is reduced by $\sim 34\%$. This matches well with the $\sim 30\%$ reduction in tool wear seen in the experiments performed by Smith *et al.* [25]. In the case of 3 layers of graphene, the wear reduction is $\sim 96\%$ and one sees no discernible change in the wear line in Figure 7.6(f).

Since the coordination analysis makes no distinction between surface atoms and graphitized atoms, the extent of graphitization must be inferred. The number of surface atoms in the tool can be assumed to stay relatively constant at $\sim \mathbf{S}_0$ throughout the duration of the simulation. Therefore, the extent of graphitized atoms can be estimated as $\mathbf{SG}(t) - \mathbf{S}_0$. Using this metric, the number of graphitized atoms in the case of the 0 and 1 platelet scenario are estimated to be 271 atoms and 31 atoms, respectively, at time $t=200$ ps. This represents a $\sim 88\%$ decrease in the extent of tool graphitization at the end of the simulation. As discussed ahead in 7.4, this trend can be explained by the fact that the platelet serves as a physical barrier to the catalyzed graphitization process, leading to lower graphitization, mostly on the rake face.

Interestingly, for the single platelet case at $t < 50$ ps, and for the three platelet case at time $t=200$ ps, the data shows that $\mathbf{SG}(t) < \mathbf{S}_0$. This decrease in $\mathbf{SG}(t)$ is correlated with a corresponding increase in $\mathbf{D}(t)$ at those times, which suggests that surface tool atoms are being forced into higher hybridization states by the high pressure contact of the cutting process, without the direct influence of the iron. These findings show that not only does the presence of the platelet barrier mitigate the graphitization tendency, but it may also be enabling the reversal of the process. This effect is more pronounced in the multilayer scenario since the graphene remains intact for a longer time, especially on the clearance face of the tool. It is currently unclear whether this effect is temporary or if it represents a lasting change at the surface of the tool.

7.3.2 Carbon Transfer Analysis

During the cutting process, the worn carbon atoms from both the tool and platelet end up transferring into the workpiece. Figure 7.7(a)-(c) depict the final locations of the carbon atoms in the workpiece, for each of the three cases, 0, 1 and 3 layered graphene platelets, respectively. In these figures, the carbon atoms originating from the tool are colored in blue while those originating from the platelet are colored black. As seen in Figure 7.7(a)-(c), carbon atoms from both sources become embedded both in the machined surface and in the chip being removed from the workpiece. In Figure 7.7(a), depicting the case without a platelet, there is evidence that wear begins right at the contact of the tool with the workpiece since there are worn tool atoms embedded in the entry region. In the scenario with 1-layer platelet, it can be seen that the carbon atoms transferred to the workpiece are primarily from the platelet, at least during the beginning of the cut (Figure 7.7(b)). For the 3-layer platelet case (Figure 7.7(c)) the atoms from the tool are only a negligible fraction of the total carbon atoms transferred into the workpiece. Both these cases suggest that the carbon from the platelet is serving as a sacrificial source for carbon transfer.

Figure 7d plots the quantitative data associated with Figure 7.7(a)-(c), with both the total number of transferred carbon atoms as well as their originating source (tool or platelet) being plotted against the length of cut. Unlike the no platelet case, where carbon transfer to the workpiece is initiated right at the entry of the cut (Figure 7.7(a)), in the presence of platelets, transferred carbon atoms do not show up until 5\AA into the cut (Figure 7.7(b)-(c)). The sacrificial role of the carbon from the platelet is corroborated by the fact that the worn tool atoms do not appear until $\sim 10\text{\AA}$ and $\sim 45\text{\AA}$ into the cut for the 1 layer and 3 layer scenarios, respectively. The data in Figure 7.7(d) also shows that the total amount of carbon atoms transferred to the workpiece, increases as the number of platelet layers increases. This can be caused by two reasons. First, the atoms in the platelet are more susceptible to being worn since they are initially sp^2 hybridized. Secondly, since the platelet appears to be acting as a BUE, it will bear most of the more intense cutting conditions described in Table 7.5. The total carbon transfer rate is strongly correlated with cutting temperature, which is plausible since the reaction rate increases with an increase in temperature.

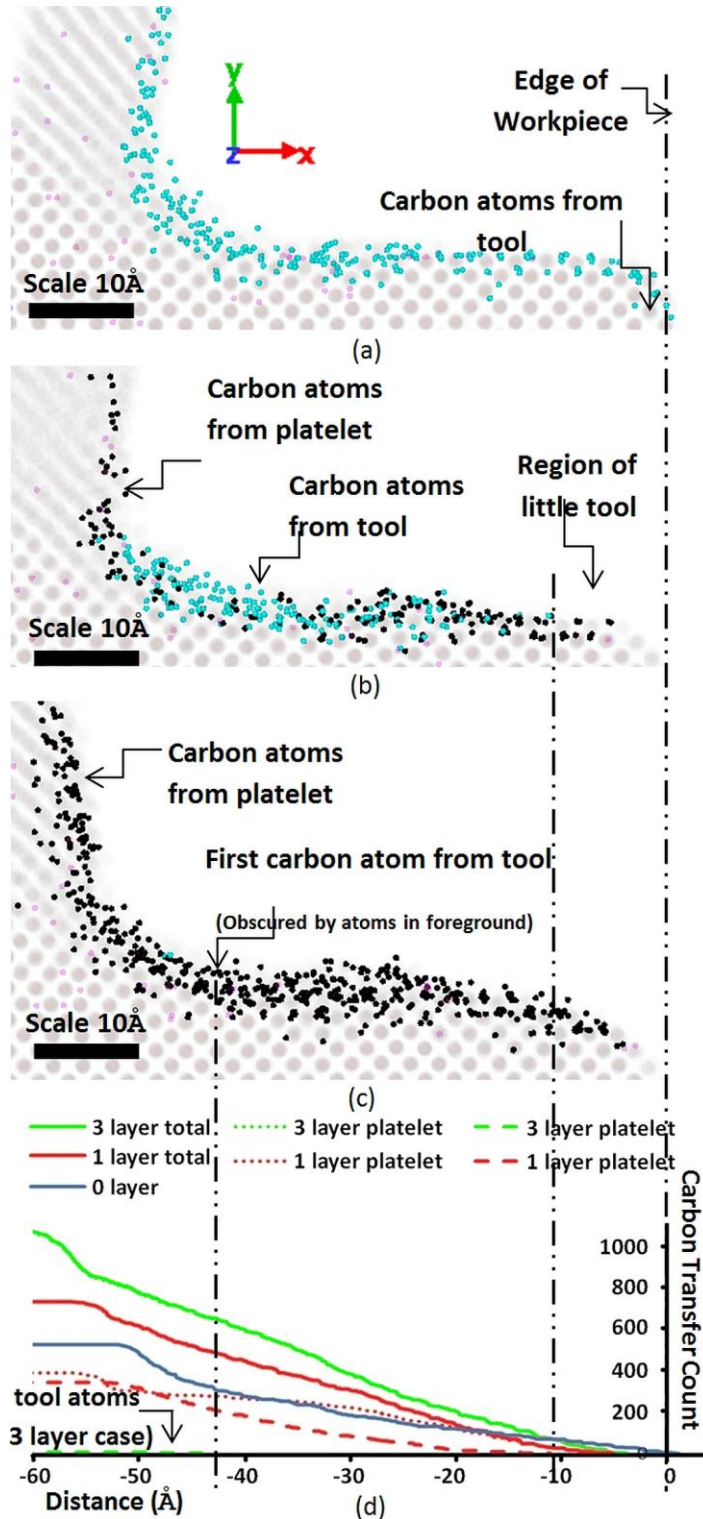


Figure 7.7: Analysis of carbon transfer from platelet(black) and tool (blue) into steel workpiece (iron: grey, carbon: purple) in the final configuration. (a-c): Vertical line on the right side of each image corresponds to the edge of the workpiece (a) no platelet (b) 1 layer platelet (c) 3 layer platelet. (d) Cumulative transferred carbon trends with source-specific contributions

7.4 Discussion

7.4.1 Comparison to Experimental Results

The results of the simulations confirm the most important conclusion of the experimental studies performed by Smith *et al.* [25], *viz.*, the presence of graphene platelets in the cutting environment drastically reduces the diamond tool wear. However, their XPS data of the machined surface showed a significant decrease in carbon transfer to the workpiece in the presence of the graphene-laden cutting fluids, whereas the simulation results (Figure 7.7) show an increase in the amount of carbon transfer. It is important to note here that the MD simulations account for carbon atoms transferred *both to the chip as well as the machined surface*, whereas the experimental study only performed XPS on the machined workpiece surface (and not the chip). In addition to this issue, the discrepancy between the experimental and the simulated results can be attributed to the following differences between the MD simulation and the experimental conditions.

First, there is a difference in the length scale of the experiment and the MD simulation, with the experiments being at the micro-scale while the MD simulations are at the atomic scale. Given the low depth of cut used in the model, the BUE formed by the graphene platelet significantly modifies the effective geometry of the cut, as shown in Figure 7.5. This subsequently has a large effect on the cutting responses (Table 7.5). However, in the experimental studies, it was found that the presence of the graphene platelets had negligible effect on the cutting forces and cutting temperatures. This is because the relative size of the tool versus the platelet differs by three orders of magnitude, so that the effective geometry of the tool is essentially unchanged even if multiple layers of graphene build up on the tool. This coupled with the fact that the MD simulations use cutting velocities significantly higher than the experimental conditions, could account for some of the discrepancy in the amount of carbon transfer.

Secondly, the effect of the cutting fluid is not explored in the simulation. Smith *et al.* [25] saw that the use of the cutting fluid lowers the cutting temperature compared to the dry machining case. It is likely that at those lower cutting temperatures, the rate of carbon graphitization and transfer is decreased. Finally, the cutting tool was modeled as a single crystal diamond whereas a polycrystalline diamond tool was used in the

experiments. The presence of multiple crystals and the binder material in the polycrystalline tool could also reduce the extent of carbon transfer into the workpiece.

7.4.2 Observed Mechanisms

A number of chemical and physical phenomena were observed from the MD simulations. These help explain the wear and graphitization behavior described in Section 7.4. While some of these mechanisms were hypothesized in the previous works of Smith *et al.* [25], Samuel *et al.* [56], and Chu *et al.* [150], some are new.

7.4.2.1 Cutting Tool Graphitization

As discussed in Section 7.4, the atoms close to the surface of the cutting tool undergo graphitization. Figure 7.8 shows a view of the rake face of the tool showing different modes of graphitization of the cutting tool, in the case without the presence of a graphene platelet. On the rake face of the tool (against which the chip glides), this graphitization is seen to be in-plane, whereas on the clearance face, which is closer to the machined surface, the graphitized bonds are seen to dangle off the face of the tool. It is unclear whether the different graphitization modes are caused by the differing machining conditions experienced by the different tool surfaces, the differing crystallography of the surfaces, or some combination of the two. Either way, it appears that this difference

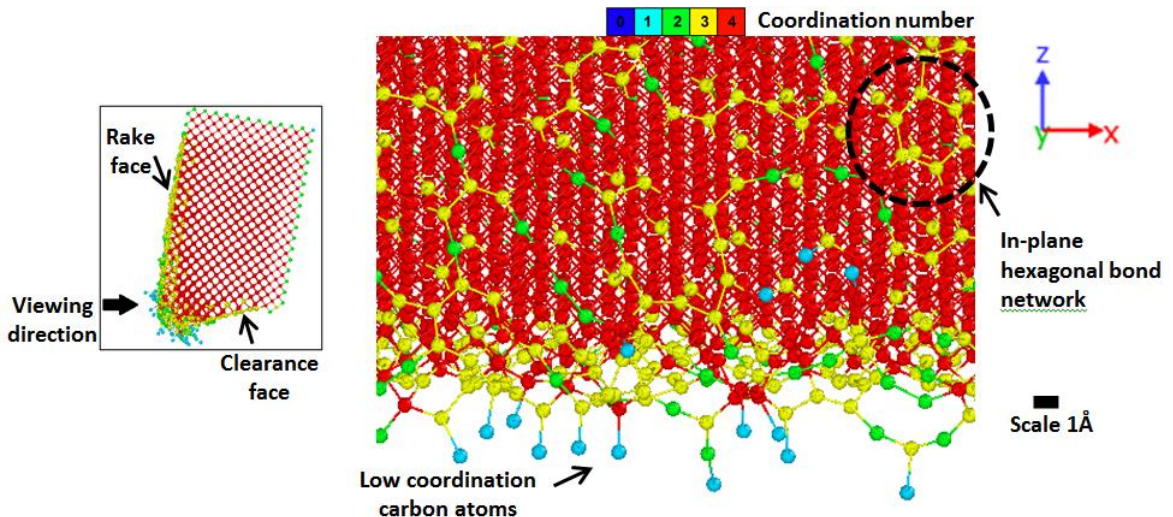


Figure 7.8: Head-on view of the rake face of tool (no platelet scenario, frame 1552, $t = 37.55$ ps.) Arrow in the inset shows viewing direction. Bonds are drawn between carbon atoms with a cutoff distance of 1.8\AA . Atoms on rake face show in-plane hexagonal bond networks representative of graphitization (black circle). 1, 2, and 3-coordinated bonds on clearance face also show graphitic bond angles

results in the wear and graphitization being more prevalent on the clearance face. This graphitization is a precursor to tool wear [107] due to fewer bonds holding the carbon atom, as confirmed by the experimental results of Smith *et al.* [25] (Figure 7.1(a)). Similar modes of graphitization of the tool are seen to occur in the scenarios with a platelet, although to a lesser extent. The lower graphitization rate in this case may be attributable to the barrier between the tool atoms and the workpiece provided by the platelet.

7.4.2.2 Platelet Cleaving

As shown in Section 7.4, the wear and graphitization of the cutting tool are delayed by the presence of a platelet. It was found that this delay is caused by the platelet acting as a physical barrier and as a sacrificial source for carbon transfer into the workpiece. Tool wear only begins when the cutting tool is able to break this physical barrier. One way this occurs is by cleaving the platelet. Figure 7.9(a) shows a thin slice of the nose of the tool just as the cleaving of the platelet begins to happen in the single platelet scenario. As seen, the tool separates the platelet into two parts and tool atoms become

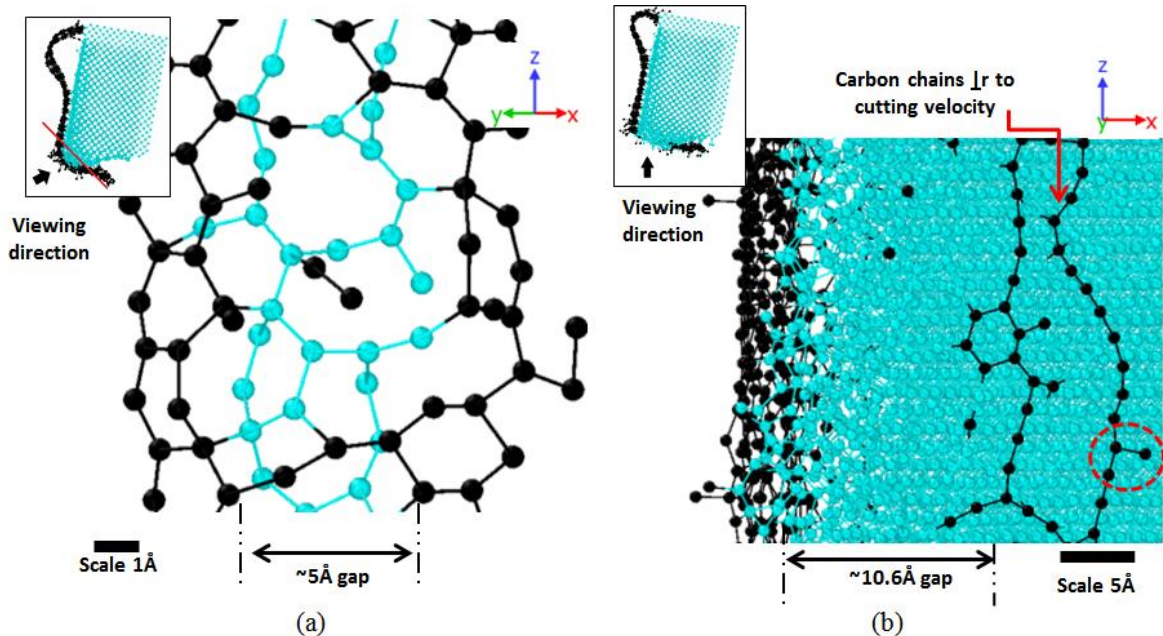


Figure 7.9: Platelet cleaving mechanism (a) View of thin slice of tool nose during cut (1 layer case, frame 2273, $t=56.88\text{ps.}$). Inset shows viewing direction and slicing plane along red line.(b) Head-on view of the clearance face of tool during the cut (single layer, frame 3875, $t=136.78\text{ps.}$). Inset shows viewing direction. Blue atoms are part of the tool. Black atoms are part of the platelet Bonds are drawn between carbon atoms with a cutoff distance of 1.8Å

part of the graphite lattice linking them. This process was seen to also push carbon atoms from the platelet into the workpiece.

As the cut progresses after platelet cleaving has started, friction on the clearance face and pressure at the tool edge increases the distance between the two parts of the cleaved platelet. The friction drags the portion of the platelet on the clearance face away from the cutting edge, enlarging the gap from $\sim 5\text{\AA}$ atom wide as seen in Figure 7.9(a) to $\sim 11\text{\AA}$ as seen in Figure 7.9(b). This dragging breaks bonds parallel to the direction of the cut, creating long chains perpendicular to the cutting direction (Figure 7.9(b)). When bonds in these chains break, they form 1-coordinated carbon atoms (circled atoms in Figure 7.9(b)) that are easily worn. At the same time, a larger amount of the tool is subjected to the cutting zone, allowing more wear to occur.

7.4.2.3 Interlayer Sliding

For the 3-layer scenario, in addition to platelet cleaving, the mechanism of interlayer sliding also appears to be involved in removing the physical platelet barrier protecting the tool. Figure 7.10 shows this phenomenon *via* tracer carbon atoms that track the relative position of the graphene sheets throughout the cut. It should be noted here that the cleaving of the platelet only happens at the atomically-sharp edge of the cutting tool where the out-of-plane force on the graphene layer is high enough to break bonds. The interlayer sliding mechanism, on the other hand, only requires the breaking of weaker non-covalent interactions, such as van der Waals forces, and as such, this mechanism depends on the ratio of the tangential force to the normal force, acting on the graphene layer. A higher value for the ratio of the tangential force to the normal force acting on a particular layer would imply a greater propensity to slide. In the three layer scenario, this ratio was the highest (0.3911) for the layer closest to the workpiece and the lowest (0.0840) for the layer closest to the tool. The middle layer had an intermediate value of 0.2113. The trend in these values correlates to the relative position of the trace carbon atoms seen in Figure 7.10(a)-(b).

As seen in Figure 7.10(b), the graphene layer closest to the workpiece experiences the maximum displacement due to sliding, whereas the layer closest to the tool surface slides the least. An analysis of the platelets at the end of the simulation reveals that a

combination of platelet cleaving and interlayer sliding occurs before the initiation of tool wear. The layer closest to the workpiece is seen to slide completely away from the cutting zone (Figure 7.10(a)-(b)). The graphene layer closest to the tool gets entirely cleaved whereas the middle layer undergoes some sliding before eventually getting cleaved. This interlayer sliding mechanism explains the decrease in thrust force seen in Table 7.5. The combined mechanism of sliding and cleaving could also explain the significant delay to the onset of tool wear (~45 ps). While the magnitude of this effect may be subject to some error due to the strength of the vdW forces, (refer Section 7.2.1), evidence of interlayer sliding has been seen in previous experimental investigations of graphene platelets in cutting processes [139].



Figure 7.10: Interlayer sliding mechanism (a) Initial configuration (b) Final configuration (Tracer atoms, shown in orange locations marked 1-3)

7.5 Summary

Molecular dynamics simulations have been successfully used to shed light on the underlying mechanisms responsible for the mitigation of chemical wear seen during the diamond cutting of steel in the presence of graphene platelets. The simulations predict tool wear reductions that match the experimental trends reported in literature. The graphene platelets are observed to act as a built up edge by wrapping around the cutting edge of the tool. In this configuration, the platelet is seen to mitigate the wear of the diamond tool by acting both as a physical barrier and as a sacrificial source for carbon transfer into the steel workpiece. The tool wear is seen to begin only after the platelet is removed from the cutting zone, either by platelet cleaving or interlayer sliding. Given the underlying mechanisms that have been identified, it is clear that the biggest challenge to overcome is that of ensuring the formation of a continuous layer of platelets around the tool cutting edge.

8. CONCLUSIONS AND RECOMMENDATIONS

The overall objective of this research was to *study the cooling and lubrication performance of graphene platelets in micro-machining environments*. The specific tasks that were performed to achieve this objective were grouped under three thrust areas, namely:

Thrust 1- Embedded Delivery: Studies in this thrust area investigated the performance of GPL introduced into microstructured materials with a particular focus on how this impacts its micro-machining responses. Specifically, machining studies on a three-phase hierarchical composite containing graphene, glass fiber, and epoxy were undertaken. The metrics measured included chip morphology, tool wear, cutting forces, cutting temperatures, and surface roughness.

Thrust 2- External Delivery: Investigations in this thrust involved enhancing the performance of both environmentally-benign and semi-synthetic cutting fluids using GPL additives. Experiments were conducted to understand the effects of the addition of GPL on lubricity and cooling. Machining responses that were measured in these studies included cutting forces, cutting temperatures, and surface roughness. In addition, key cutting fluid properties, such as viscosity and thermal conductivity, were measured.

Thrust 3- Cooling and Lubrication Mechanisms: The studies in this thrust first focused on single droplet impingement experiments to study the fundamental behaviors of the cutting fluids developed under Thrust 2. Specifically, the heat capacity, spreading behavior, and graphene film formation mechanisms were examined. This thrust also used MD techniques to investigate the mechanisms responsible for the mitigation of chemical diamond tool wear when machining transition metals.

8.1 Conclusions

In this thesis, the behavior of graphene platelets in various micro-machining environments has been studied. Both embedded and external delivery techniques were explored. Extensive investigation into fundamental cooling and lubrication mechanisms

were performed using single droplet impingement studies and molecular dynamics techniques. The specific conclusions that can be drawn from each portion of this work are given as follows.

8.1.1 Embedded Delivery Using Hierarchical Graphene Composites

The machinability of a hierarchical composite enhanced with graphene was investigated and contrasted to a glass fiber reinforced composite baseline. Micro-milling tests were conducted to compare the tool wear, cutting forces, cutting temperature, and chip morphology between the two materials. The following conclusions can be drawn from this study:

1. A manufacturing process for the making of hierarchical graphene composites involving glass fiber weaves and epoxy has been established. It uses the process used to manufacture graphene epoxy composites in conjunction with a hand lay-up and vacuum bagging process.
2. The micro-milling tests reveal that in general the tool wear, cutting forces and surface roughness are lower for the hierarchical graphene composite when compared to the baseline glass fiber composite thereby implying better machinability, while still improving the mechanical properties of the composite.
3. The primary mechanisms responsible for better machinability of the hierarchical composite include:
 - Graphene platelets improve the thermal conductivity of the epoxy matrix and also provide lubrication at the tool-chip interface. Both of these factors reduce the extent of polymer debris attachment on the tool and subsequent tool-wear.
 - Superior interface strength between the graphene-laden epoxy and the glass fibers allows for shorter effective lengths of failure for the glass fibers. This also results in a shear loading on the fibers in the case of the hierarchical composites as opposed to a bending load seen in the baseline composite.
4. Increase in the cutting velocity is seen to reduce the surface roughness in both materials. The cutting forces reveal that for the base-line composite it is preferable

to machine at higher cutting speeds at all FPT values, whereas for the hierarchical composites, a higher cutting speed is seen to increase the cutting forces especially while machining at FPT values higher than the critical fiber size.

5. The negative debonding trends seen on the surface of the slot are not conclusive because of the sub-surface damage caused by the rough milling operation. However, the side-walls of the slots reveal that the hierarchical composite has lower extent of debonding when compared to the base composite.

8.1.2 External Delivery Using Graphene-Enhanced Environmentally-Benign Cutting Fluids

This study aimed to create stable suspensions of graphene platelets in plant-based oils, specifically canola oil, and to then characterize its performance as a cutting oil for micro-machining applications. The following specific conclusions can be drawn from this study:

1. Graphene platelets are difficult to disperse in canola oil. Functionalizing the graphene with carboxyl groups increases its dispersion and allows loadings of up to 0.15% by weight to be created. Loadings $> 0.15\%$ result in visible clumps of undispersed graphene.
2. When compared to the baseline canola oil, both the thermal conductivity and the kinematic viscosity of the cutting oil increases, with increased loading of GPL.
3. The loading of 0.05% GPL results in the lowest coefficient of friction. As the GPL loading is increased further, the coefficient of friction between two surfaces is observed to increase.
4. The addition of GPL to the canola oil causes cutting forces, cutting temperatures, and surface roughness values to decrease when compared against both dry machining and the use of pure canola oil. The results were seen to hold true for all loadings of 0.05%, 0.1 % and 0.15% of GPL.
5. Cutting forces showed an increase between the 0.10% and 0.15% loadings, which is likely due to GPL clusters and/or the formation of built-up edges. This suggests that an optimal loading for lubrication exists between the tested concentrations.
6. Surface roughness increases with increased GPL content. This is caused by GPL entrapment between the tool and the workpiece.

8.1.3 External Delivery Using Graphene Oxide Colloidal Suspensions as Cutting Fluids

The fabrication of graphene platelets with varying sizes and chemical functionalization was accomplished by varying the oxidation and exfoliation steps in the fabrication pipeline. Solutions of these graphene platelets dispersed in a semi-synthetic cutting fluid were fabricated, characterized, and used in micro-turning studies. Comparisons of the performance of these fluids were made on the basis of cutting temperature, cutting force, and surface roughness. The following specific conclusions can be drawn from this study:

1. Thermal and ultrasonic exfoliation techniques were developed to fabricate graphene oxide platelets (GOP) of varying lateral dimensions, thickness and oxygen functionalization that could serve as additives for semi-synthetic cutting fluids. The thermal reduction technique was seen to result in a thicker GOP with 4-8 graphene layers, (depending on the processing temperatures), whereas the ultrasonic exfoliation resulted in a thinner GOP with 2-3 graphene layers.
2. The extent of oxygen functionalization of the GOP was seen to be a key factor affecting the agglomeration of the platelets in the colloidal suspension. Low levels of oxygen functionalization (using thermal exfoliation) resulted in relatively larger in-solution characteristic lateral lengths of 562 -2780 nm, whereas the higher level of oxygen functionalization (using ultrasonic exfoliation) was seen to result in the lowest in-solution characteristic lateral length of 120 nm.
3. In general, the addition of GOP is seen to increase both the dynamic viscosity as well as the thermal conductivity of the cutting fluids.
 - At concentrations < 0.5 wt%, the increase in the dynamic viscosity for all GOP-laden fluids is less than 22% when compared to that of the baseline cutting fluid. However, at concentrations > 0.5 wt%, sharp increases of 75-830% are seen in the dynamic viscosities for the ultrasonically exfoliated GOP solutions.
 - At concentrations < 0.5 wt%, the increase in thermal conductivity for all GOP-laden fluids is 8-16% when compared to that of the baseline cutting fluid. The thermally-reduced and ultrasonically-exfoliated GOP solutions

show a peak in their thermal conductivity at 0.5 wt% and 0.2 wt%, respectively.

4. The micro-machining tests reveal that the GOP colloidal suspensions are capable of improving the performance of the baseline cutting fluid by significantly reducing the cutting temperatures and surface roughness encountered during the machining process. However, the cutting forces are generally noticed to be higher for these solutions.

- The ultrasonically-exfoliated GOP appears to be the most favorable for micro-machining applications. Even at the lowest concentration of 0.1 wt%, they are capable of providing a ~51% reduction in the cutting temperatures and a 25% reduction in the surface roughness values over those of the baseline cutting fluid. The 0.2 wt% loading provides the optimal combination of both low cutting forces as well as cutting temperatures.
- For the thermally-reduced GOP solutions, the 0.2 wt% appears to be ideal since it results in the lowest cutting temperatures (25-43% reduction over the baseline cutting fluid) and cutting forces that are comparable to the baseline cutting fluid. However, even at this concentration, the US GOP is seen to outperform the TR GOP.

5. The micro-machining tests reveal that the bulk properties of the colloidal suspensions are weakly correlated to the machining performance of the fluids. This suggests that that the differences seen between the colloidal suspensions in terms of their droplet spreading, evaporation, and the subsequent GOP film-formation characteristics may be better indicators of their machining performance, as opposed to their bulk properties.

8.1.4 Droplet Dynamics and Film Formation Mechanisms of Graphene Oxide Colloidal Suspensions

The graphene-enhanced fluids outlined in Chapter 5 were used to perform single-droplet impingement studies on a heated substrate. The evaporation dynamics of the solutions were analyzed by comparing temperature profiles and the evolution of droplet shapes *via* high-speed imaging. The residual graphene film deposited on the substrate

was analyzed through optical microscopy. Different groups of droplet spreading and film formation behaviors were identified and these behaviors correlated with the performance of the fluids in the machining studies performed in Chapter 5. The following specific conclusions can be drawn from the results of this single-droplet impingement study of graphene oxide colloidal solutions:

1. The temperature profiles and the high-speed images of the graphene oxide colloidal droplets show three distinct regimes, *viz.*, the spreading regime where the droplet is deposited, the pinning regime where convection heating causes the loss of droplet volume, and the receding regime where the droplet evaporates completely.
2. The absolute minimum temperature drop seen in the spreading regime and the average temperature seen in the pinning regime are similar for all GOP solutions, indicating that the evaporative cooling characteristics are similar across the liquids.
3. At concentrations <0.5 wt%, all GOP solutions have a shorter total lifetime when compared to the baseline liquid. At concentrations ≥ 0.5 wt%, the ultrasonically exfoliated GOP has the longest overall droplet lifetime with their receding phase having the longest duration.
4. The data from the pinning regime show that, when deposited on a heated substrate, the GOP solutions demonstrate a reduced wettability, with the ultrasonically exfoliated GOP solutions being the most hydrophobic. The presence of the GOP is also seen to reduce the evaporation-induced decay rate of the droplet height and contact angle.
5. For TR GOP at concentrations <0.5 wt%, as the droplet evaporates in the receding regime, a small region of high convection is noticeable at the droplet boundary. This results in increased film thickness at the center of the droplet (1–5 μm) compared to the periphery (0.1–0.3 μm). This type of the film is hypothesized to be the reason for the higher magnitudes and variation in the cutting forces and temperatures.
6. For TR GOP at concentrations ≥ 0.5 wt%, the higher concentration of GOP is seen to result in distributed micro-boiling within the droplet. This ultimately forms a 7–

12 μm thick film with fissures formed by escaping vapor. These thicker films are hypothesized to be the reason behind the increase in the cutting force, possibly due to the rubbing along the clearance face.

7. Ultrasonically exfoliated GOP at concentrations <0.5 wt% show evidence of nucleation-induced formation of the GOP film on the substrate. The film is not only uniform but is also the thinnest (0.4–0.5 μm) among all the GOP solutions. These thin and uniform films are hypothesized to be responsible for the superior machining performance of these colloidal solutions.
8. At concentrations ≥ 0.5 wt%, the ultrasonically exfoliated GOP solutions are seen to lose their advantage. The GOP film left behind on the substrate is characterized by the bursting of vapor bubbles. The film around these regions is significantly thicker (20–120 μm) than the remaining portion of the film (1–5 μm). This thick and uneven film is hypothesized to be responsible for the deterioration of the cutting fluid performance.
9. Rather than the bulk properties (*viz.*, thermal conductivity and dynamic viscosity) of the GOP colloidal suspensions, a more important criterion dictating the machining performance of the GOP colloidal solutions appears to be its ability to form submicron thick, uniform graphene oxide films upon evaporation of the carrier fluid. The findings of this study reveal that the characterization of the residual graphene oxide film left behind on a heated substrate may be an efficient technique to evaluate different graphene oxide colloidal solutions for cutting fluids applications in micro-machining.

8.1.5 Chemical Wear Mitigation Mechanisms of Graphene During Diamond Cutting of Steel

Molecular dynamics simulations have been successfully used to shed light on the underlying mechanisms responsible for the mitigation of chemical wear seen during the diamond cutting of steel in the presence of graphene platelets. The simulations predict tool wear reductions that match the experimental trends reported in literature. The graphene platelets are observed to act as a built up edge by wrapping around the cutting edge of the tool. In this configuration, the platelet is seen to mitigate the wear of the diamond tool by acting both as a physical barrier and as a sacrificial source for carbon

transfer into the steel workpiece. The tool wear is seen to begin only after the platelet is removed from the cutting zone, either by platelet cleaving or interlayer sliding. Given the underlying mechanisms that have been identified, it is clear that the biggest challenge to overcome is that of ensuring the formation of a continuous layer of platelets around the tool cutting edge.

8.2 Recommendations for Future Work

This research has identified a great deal regarding the behavior of graphene platelets in micro-machining applications, proving them provide effective lubrication, cooling, and wear mitigation, as well as illustrating some of the fundamental mechanisms responsible for their performance. Based on the findings of this thesis, some desirable areas of future investigations have been identified below.

8.2.1 Experimental Studies

1. In each study presented in this thesis, the concentration of graphene in the relevant carrier media was limited to at most four different levels. As shown in Chapter 5, the behavior of the graphene platelet is very likely dependent on concentration. Studies with more granular concentration, between 0.2 and 0.5 wt%, will help identify the exact location of the transition between low concentration and high concentration behavior and may suggest reasons for the differing behaviors.
2. There are many avenues of work outside of the scope of this thesis in both embedded and external delivery methods. For embedded delivery methods, other matrix materials such as ceramics and metals can be explored. While the processing routes for these new materials have already been established, the effect of the GPL-reinforcement on the machinability of these materials is unknown and will likely differ from the behavior of the hierarchical graphene composite tested in this research.
3. For external delivery, other mechanisms such as MQL and flood cooling can be studied. A critical need identified in this research is the continuous replenishment of graphene in the cutting zone. Solving this problem could involve surface and/or

chemical modification of tools to promote effective adhesion of graphene in the cutting zone.

4. The variability in size and chemical functionalization of the graphene platelets fabricated in this research were a consequence of the specific processing steps. Alternate GPL production routes that enable independent control over the size and chemical functionalizations of the platelets would allow for a more thorough investigation into their influence on machining outcomes. This could also form the basis of investigations involving targeted functionalization of the graphene platelet in order to achieve desired properties, such as proper dispersion behavior in various carrier fluids.
5. The development of new techniques for data gathering like pyrometry-based temperature measurement [153-154] may enable data collection in the high-pressure, micro-scale cutting zone. This coupled with efforts to scale down the size of the cutting experiments, perhaps down to the nano-scale, can close the gap between the molecular dynamics modeling work and the micro-scale machining experiments. This may involve using non-standard machining techniques such as ultramicrotome cutting [155].
6. Since this research effort started in 2011, the field of 2D nano-materials has exploded. Much like graphene, 2D forms of other bulk solid lubricants have been synthesized, such as hexagonal boron nitride, molybdenum disulfide, and tungsten disulfide [156]. These new 2D materials also show promise as lubricants in micro-machining applications. While the geometry of these materials is similar to graphene, their different chemical natures may make certain ones more favorable with certain workpiece and tool material combinations and should be investigated.

8.2.2 Modeling Studies

1. The molecular dynamics study presented in this thesis can be extended by performing a parametric study investigating the effects of the cutting speed, depth of cut, cutting tool geometry, graphene platelet orientation, and carbon concentration of the steel on the wear mitigation phenomena. A well designed

parametric study using this model may reveal new behaviors that were not seen in the work presented in Chapter 7.

2. The size-scale of the simulations can be expanded to micro-scale cutting in order to obtain more realistic MD results. The added complexity of this expanded model will likely necessitate the development of new algorithms. In addition, the effects of the liquid phase, omitted in the current studies, may be included by coupling the results of MD simulations to finite element models at larger scales.
3. The development of new force field potentials for MD simulation is another rich avenue for future research. In the actual cutting experiments, atmospheric gases, the molecules of the cutting fluid, and even the alloying materials or impurities of the workpiece and/or tool can all have an effect on the chemical wear process. Current MD potentials very rarely describe more than two chemical species at a time. This is a huge gap in the state of knowledge which, if filled, can increase the fidelity of MD simulations.

References

- [1] K.F. Ehmann *et al.*, *Micromanufacturing: International Research and Development*. Dordrecht, The Netherlands: Springer, 2007.
- [2] X. Liu, R.E. DeVor, S.G. Kapoor, and K.F. Ehmann, “The mechanics of machining at the microscale: Assessment of the current state of the science,” *J. Manuf. Sci. Eng.*, vol. 126, no. 4, pp. 666–678, Feb. 2005.
- [3] A.E. Honegger *et al.*, “Development of an automated microfactory: Part 1 – microfactory architecture and sub-systems development,” *Trans. NAMRI/SME*, vol. 34, pp. 333-340, May 2006.
- [4] A.E. Honegger *et al.*, “Development of an automated microfactory: Part 2— experimentation and analysis,” *Trans. NAMRI/SME*, vol. 34 pp. 341–348, May 2006.
- [5] G.J. Ellicott, R.E. DeVor, and S.G. Kapoor, “Machinability investigation of micro-scale hard turning of 52100 steel,” *Trans. NAMRI/SME*, vol. 37, pp. 143–150, May 2009.
- [6] Z. Lu, H. Hu, Y. Sun, and Q. Sun, “Study on residual stresses in ultrasonic torsional vibration assisted micro-milling,” in *5th Int. Symp. Advanced Optical Manufacturing and Testing Technologies*, Dalian, China, 2010, pp. 76571F–76571F.
- [7] B. Wang, Y.C. Liang, Y. Zhao, and S. Dong, “Measurement of the residual stress in the micro milled thin-walled Structures,” in *Journal of Physics: Conference Series*, Harbin, China, 2006, vol. 48, pp. 1127.
- [8] X. Liu, R.E. DeVor, and S.G. Kapoor, “An analytical model for the prediction of minimum chip thickness in micro-machining,” *J. Manuf. Sci. Eng.*, vol. 128, no. 2, pp. 474–481, Sep. 2005.
- [9] M. Jun, R.E. DeVor, S.G. Kapoor, and F. Englert, “Experimental investigation of machinability and tool wear in micro-endmilling,” *Trans. NAMRI/SME*, vol. 36, pp. 201–208, May 2008.
- [10] H. Watanabe, H. Tsuzaka, and M. Masuda, “High-speed micro drilling on printed circuit boards- Influence of PCB Composite Material on Drill Breakage,” *J. Jpn. Soc. Precis. Eng.*, vol. 75, no. 12, pp. 1428–1433, Dec. 2009.

- [11] K. Liu and S.N. Melkote, "Effect of plastic side flow on surface roughness in micro-turning process," *Int. J. Mach. Tools Manu.*, vol. 46, no. 14, pp. 1778–1785, Nov. 2006.
- [12] J. Samuel, S. Sood, S.G. Kapoor, and R.E. DeVor, "Micro-scale machining of bulk metallic glass," presented at the 5th Int. Conf. Micro-Manufacturing, Madison, WI, 2010.
- [13] R. M'Saoubi, J.C. Outeiro, H. Chandrasekaran, O.W. Dillon Jr., and I.S. Jawahir, "A review of surface integrity in machining and its impact on functional performance and life of machined products," *Int. J. Sust. Manuf.*, vol. 1, no. 1–2, pp. 203–236, 2008.
- [14] I.N. Tansel *et al.*, "Tool wear estimation in micro-machining.: Part I: tool usage–cutting force relationship," *Int. J. Mach. Tools Manu.*, vol. 40, no. 4, pp. 599–608, Mar. 2000.
- [15] C.D. Torres, *et al.*, "Analyzing the performance of diamond-coated micro end mills," *Int. J. Mach. Tools Manu.*, vol. 49, no. 7, pp. 599–612, June 2009.
- [16] S. Park and R.S. Ruoff, "Chemical methods for the production of graphenes," *Nat. Nanotechnol.*, vol. 4, no. 4, pp. 217–224, Mar. 2009.
- [17] A.K. Geim and K.S. Novoselov, "The rise of graphene," *Nat. Mater.*, vol. 6, no. 3, pp. 183–191, Mar. 2007.
- [18] C. Lee, X. Wei, J.W. Kysar, and K. Hone, "Measurement of the elastic properties and intrinsic strength of monolayer graphene," *Science*, vol. 321, no. 5887, pp. 385–388, July 2008.
- [19] J. Van den Brink, "Graphene: from strength to strength," *Nat. Nanotechnol.*, vol. 2, no. 4, pp. 199–201, Apr. 2007.
- [20] D. Li and R.B. Kaner, "Graphene-based materials," *Nat. Nanotechnol.*, vol. 3, pp. 101, May 2008.
- [21] I. Arora, J. Samuel, and N. Koratkar, "Experimental investigation of the machinability of epoxy reinforced with graphene platelets," *J. Manuf. Sci. Eng.*, vol. 135, no. 4, pp. 041007, July 2013.

- [22] F. Yavari, M.A. Rafiee, J. Rafiee, Z.Z. Yu, and N. Koratkar, “Dramatic increase in fatigue life in hierarchical graphene composites,” *ACS Appl. Mater. Interfaces*, vol. 2, no. 10, pp. 2738–2743, Sep. 2010.
- [23] K.H. Park, K. Shantanu, P. Kown, L.T. Drazl, and I. Do, “Minimum quantity lubrication (MQL) with nanographene-enhanced lubricates: Ballmilling experiment,” *Trans. NAMRI/SME*, vol. 38, pp. 81–88, July 2010.
- [24] M. Alberts, K. Kalaitzidou, and S. Melkote, “An investigation of graphite nanoplatelets as lubricant in grinding,” *Int. J. Mach. Tools Manu.*, vol. 49, no. 12, pp. 966–970, Oct. 2009.
- [25] P.J. Smith *et al.*, “Graphene oxide colloidal suspensions mitigate carbon diffusion during diamond turning of steel,” *J. Manuf. Process.*, vol. 17, pp. 41–47, Jan. 2015.
- [26] J.C. Slonczewski and P.R. Weiss, “Band structure of graphite,” *Phys. Rev.*, vol. 109, no. 2, pp. 272, Jan. 1958.
- [27] E. Fradkin, “Critical behavior of disordered degenerate semiconductors. I. Models, symmetries, and formalism,” *Phys. Rev. B*, vol. 33, no. 5, pp. 3257, Mar. 1986.
- [28] K.S. Novoselov *et al.*, “Electric field effect in atomically thin carbon films,” *Science*, vol. 306, no. 5696, pp. 666–669, Oct. 2004.
- [29] D.R. Dreyer, S. Park, C.W. Bielawski, and R.S. Ruoff, “The chemistry of graphene oxide,” *Chem. Soc. Rev.*, vol. 39, no. 1, pp. 228–240, Nov. 2009.
- [30] G. Van Lier, C. Van Alsenoy, V. Van Doren, and P. Geerlings, “Ab initio study of the elastic properties of single-walled carbon nanotubes and graphene,” *Chem. Phys. Lett.*, vol. 326, no. 1, pp. 181–185, Aug. 2000.
- [31] S. Berber, Y.K. Kown, and D. Tománek, “Unusually high thermal conductivity of carbon nanotubes,” *Phys. Rev. Lett.*, vol. 84, no. 20, pp. 4613, May 2000.
- [32] M.S. Dresselhaus, G. Dresselhaus, and P.C Eklund, *Science of Fullerenes and Carbon Nanotubes: Their Properties and Applications*. San Diego, CA: Academic Press, 1996.
- [33] A.A. Balandin *et al.*, “Superior thermal conductivity of single-layer graphene,” *Nano Lett.*, vol. 8, no. 3, pp. 902–907, Mar. 2008.

- [34] V. Georgakilas, *et al.*, “Functionalization of graphene: covalent and non-covalent approaches, derivatives and applications,” *Chem. Rev.*, vol. 112, no. 11, pp. 6156–6214, Nov. 2012.
- [35] C. Nethravathi and M. Rajamathi, “Chemically modified graphene sheets produced by the solvothermal reduction of colloidal dispersions of graphite oxide,” *Carbon*, vol. 46, no. 14, pp. 1994–1998, Nov. 2008.
- [36] Z. Zhang, H. Huang, X. Yang, and L. Zang, “Tailoring electronic properties of graphene by π - π stacking with aromatic molecules,” *J. Phys. Chem. Lett.*, vol. 2, no. 22, pp. 2897–2905, Nov. 2011.
- [37] Z.-B. Liu *et al.*, “Porphyrin and fullerene covalently functionalized graphene hybrid materials with large nonlinear optical properties,” *J. Phys. Chem. B*, vol. 113, no. 29, pp. 9681–9686, July 2009.
- [38] D. Li, M.B. Mueller, S. Gilje, R.B. Kaner, and G.G. Wallace, “Processable aqueous dispersions of graphene nanosheets,” *Nat. Nanotechnol.*, vol. 3, no. 2, pp. 101–105, Feb. 2008.
- [39] Y. Zhu *et al.*, “Exfoliation of graphite oxide in propylene carbonate and thermal reduction of the resulting graphene oxide platelets,” *ACS Nano*, vol. 4, no. 2, pp. 1227–1233, Feb. 2010.
- [40] K.M. F. Shahil and A.A. Balandin, “Thermal properties of graphene and multilayer graphene: Applications in thermal interface materials,” *Solid State Commun.*, vol. 152, no. 15, pp. 1331–1340, Aug. 2012.
- [41] S.H. Song *et al.*, “Enhanced thermal conductivity of epoxy–graphene composites by using non-oxidized graphene flakes with non-covalent functionalization,” *Adv. Mater.*, vol. 25, no. 5, pp. 732–737, Feb. 2013.
- [42] X. Feng, S. Kwon, J.Y. Park, and M. Salmeron, “Superlubric sliding of graphene nanoflakes on graphene,” *ACS Nano*, vol. 7, no. 2, pp. 1718–1724, Feb. 2013.
- [43] S. Stankovich *et al.*, “Synthesis of graphene-based nanosheets *via* chemical reduction of exfoliated graphite oxide,” *Carbon*, vol. 45, no. 7, pp. 1558–1565, June 2007.

- [44] A.V. Eletsii, I.M. Iskandarova, A.A. Knizhink, and D.N. Krasikov, "Graphene: fabrication methods and thermophysical properties," *Phys. Usp.*, vol. 54, no. 3, pp. 227–258, Mar. 2011.
- [45] M.A. Rafiee, J. Rafiee, Z.Z. Yu, and N. Koratkar., "Buckling resistant graphene nanocomposites," *Appl. Physics Lett.*, vol. 95, no. 22, pp. 223103, Nov. 2009.
- [46] L. Shahriary and A.A. Athawale, "Graphene oxide synthesized by using modified hummers approach," *IJREEE*, vol. 2, no. 1, pp. 58–63, Jan. 2014.
- [47] H.L. Poh *et al.*, "Graphenes prepared by Staudenmaier, Hofmann and Hummers methods with consequent thermal exfoliation exhibit very different electrochemical properties," *Nanoscale*, vol. 4, no. 11, pp. 3515, Apr. 2012.
- [48] H.C. Schniepp *et al.*, "Functionalized single graphene sheets derived from splitting graphite oxide," *J. Phys. Chem. B*, vol. 110, no. 17, pp. 8535–8539, May 2006.
- [49] Y. Hernandez *et al.*, "High-yield production of graphene by liquid-phase exfoliation of graphite," *Nat. Nano*, vol. 3, no. 9, pp. 563–568, Sep. 2008.
- [50] S.M. Notley, "Highly concentrated aqueous suspensions of graphene through ultrasonic exfoliation with continuous surfactant addition," *Langmuir*, vol. 28, no. 40, pp. 14110–14113, Oct. 2012.
- [51] A.V. Gopal and P.V. Rao, "Performance improvement of grinding of SiC using graphite as a solid lubricant," *Mater. Manuf. Process.*, vol. 19, no. 2, pp. 177–186, Dec. 2004.
- [52] P.V. Krishna and D.N. Rao, "Performance evaluation of solid lubricants in terms of machining parameters in turning," *Int. J. Mach. Tools Manu.*, vol. 48, no. 10, pp. 1131–1137, Aug. 2008.
- [53] N.S.K. Reddy and P.V. Rao, "Experimental investigation to study the effect of solid lubricants on cutting forces and surface quality in end milling," *Int. J. Mach. Tools Manu.*, vol. 46, no. 2, pp. 189–198, Feb. 2006.
- [54] A. Marcon, S. Melkote, K. Kalaitzidou, and D. DeBra, "An experimental evaluation of graphite nanoplatelet based lubricant in micro-milling," *CIRP Ann.-Manuf. Techn.*, vol. 59, no. 1, pp. 141–144, 2010.

- [55] H.D. Huang, J.P. Tu, L.P. Gan, and C.Z. Li, “An investigation on tribological properties of graphite nanosheets as oil additive,” *Wear*, vol. 261, no. 2, pp. 140–144, July 2006.
- [56] J. Samuel, J. Rafiee, P. Dhiman, Z.Z. Yu, and N. Koratkar, “Graphene colloidal suspensions as high performance semi-synthetic metal-working fluids,” *J. Phys. Chem. C*, vol. 115, no. 8, pp. 3410–3415, Feb. 2011.
- [57] X. Huang, X. Qi, F. Boey, and H. Zhang, “Graphene-based composites,” *Chem. Soc. Rev.*, vol. 41, no. 2, pp. 666–686, Jan. 2012.
- [58] S. Stankovich *et al.*, “Graphene-based composite materials,” *Nature*, vol. 442, no. 7100, pp. 282–286, July 2006.
- [59] T. Kuilla *et al.*, “Recent advances in graphene based polymer composites,” *Prog. Polym. Sci.*, vol. 35, no. 11, pp. 1350–1375, Nov. 2010.
- [60] J.R. Potts, D.R. Dreyer, C.W. Bielawski, and R.S. Ruoff, “Graphene-based polymer nanocomposites,” *Polymer*, vol. 52, no. 1, pp. 5–25, Jan. 2011.
- [61] M.A. Rafiee *et al.*, “Enhanced mechanical properties of nanocomposites at low graphene content,” *ACS Nano*, vol. 3, no. 12, pp. 3884–3890, Dec. 2009.
- [62] L.-Y. Chen *et al.*, “Novel nanoprocessing route for bulk graphene nanoplatelets reinforced metal matrix nanocomposites,” *Scripta Mater.*, vol. 67, no. 1, pp. 29–32, July 2012.
- [63] J. Wang *et al.*, “Reinforcement with graphene nanosheets in aluminum matrix composites,” *Scripta Mater.*, vol. 66, no. 8, pp. 594–597, Apr. 2012.
- [64] M.A. Rafiee *et al.*, “Fracture and fatigue in graphene nanocomposites,” *Small*, vol. 6, no. 2, pp. 179–183, Jan. 2010.
- [65] O.C. Compton, S. Kim, C. Pierre, J.M. Torkelson, and S.T. Nguyen, “Crumpled graphene nanosheets as highly effective barrier property enhancers,” *Adv. Mater.*, vol. 22, no. 42, pp. 4759–4763, Sept. 2010.
- [66] K. Zhang, L.L. Zhang, X.S. Zhao, and J. Wu, “Graphene/polyaniline nanofiber composites as supercapacitor electrodes,” *Chem. Mater.*, vol. 22, no. 4, pp. 1392–1401, Jan. 2010.

- [67] G. Zhou *et al.*, “Graphene-wrapped Fe₃O₄ anode material with improved reversible capacity and cyclic stability for lithium ion batteries,” *Chem. Mater.*, vol. 22, no. 18, pp. 5306–5313, Aug. 2010.
- [68] H. Zhang, X. Lv, Y. Li, Y. Wang, and J. Li, “P25-graphene composite as a high performance photocatalyst,” *ACS Nano*, vol. 4, no. 1, pp. 380–386, Dec. 2009.
- [69] C.Y. Poon and B. Bhushan, “Comparison of surface roughness measurements by stylus profiler, AFM and non-contact optical profiler,” *Wear*, vol. 190, no. 1, pp. 76–88, Nov. 1995.
- [70] D.E. Dimla, “Sensor signals for tool-wear monitoring in metal cutting operations—a review of methods,” *Int. J. Mach. Tools Manu.*, vol. 40, no. 8, pp. 1073–1098, June 2000.
- [71] K. Nakayama, M.C. Shaw, and R.C. Brewer, “Relationship between cutting forces, temperatures, built-up edge and surface finish,” *CIRP Ann.-Manuf. Techn.*, vol. 14, no. 2, pp. 211–223, 1965.
- [72] D. O’sullivan and M. Cotterell, “Temperature measurement in single point turning,” *J. Mater. Process. Tech.*, vol. 118, no. 1, pp. 301–308, Dec. 2001.
- [73] H. Weule, V. Hüntrup, and H. Tritschler, “Micro-cutting of steel to meet new requirements in miniaturization,” *CIRP Ann.-Manuf. Techn.*, vol. 50, no. 1, pp. 61–64, 2001.
- [74] S. To, W.B. Lee, and C.Y. Chan, “Ultraprecision diamond turning of aluminium single crystals,” *J. Mater. Process. Tech.*, vol. 63, no. 1, pp. 157–162, Jan. 1997.
- [75] M.E. Merchant, “Mechanics of the metal cutting process. I. Orthogonal cutting and a type 2 chip,” *J. Appl. Phys.*, vol. 16, no. 5, pp. 267–275, May 1945.
- [76] R. Komanduri, “In Memoriam: M. Eugene Merchant,” *J. Manuf. Sci. Eng.*, vol. 128, no. 4, pp. 1034–1036, Nov. 2006.
- [77] T.H.C. Childs and G.W. Rowe, “Physics in metal cutting,” *Rep. Prog. Phys.*, vol. 36, no. 3, pp. 223, Mar. 1973.
- [78] G. Bissacco, H.N. Hansen, and K. Slunsky, “Modelling the cutting edge radius size effect for force prediction in micro milling,” *CIRP Ann.-Manuf. Techn.*, vol. 57, no. 1, pp. 113–116, 2008.

- [79] E.J.A. Armarego, "A generic mechanics of cutting approach to predictive technological performance modeling of the wide spectrum of machining operations," *Mach. Sci. Technol.*, vol. 2, no. 2, pp. 191–211, Nov. 1998.
- [80] M.P. Vogler, R.E. DeVor, and S.G. Kapoor, "Microstructure-level force prediction model for micro-milling of multi-phase materials," *J. Manuf. Sci. Eng.*, vol. 125, no. 2, pp. 202–209, Apr. 2003.
- [81] T.D. Marusich and M. Ortiz, "Modelling and simulation of high-speed machining," *Int. J. Numer. Meth. Eng.*, vol. 38, no. 21, pp. 3675–3694, Nov. 1995.
- [82] E. Ceretti, M. Lucchi, and T. Altan, "FEM simulation of orthogonal cutting: serrated chip formation," *J. Mater. Process. Technol.*, vol. 95, no. 1, pp. 17–26, Oct. 1999.
- [83] Y.B. Guo and D.W. Yen, "A FEM study on mechanisms of discontinuous chip formation in hard machining," *J. Mater. Process. Technol.*, vol. 155, pp. 1350–1356, Nov. 2004.
- [84] K.W. Kim, W.Y. Lee, and H.C. Sin, "A finite element analysis for the characteristics of temperature and stress in micro-machining considering the size effect," *Int. J. Mach. Tools. Manu.*, vol. 39, no. 9, pp. 1507–1524, Sep. 1999.
- [85] C.R. Dandekar and Y.C. Shin, "Multi-step 3-D finite element modeling of subsurface damage in machining particulate reinforced metal matrix composites," *Compos Part A- Appl. S.*, vol. 40, no. 8, pp. 1231–1239, Aug. 2009.
- [86] R. Komanduri and L.M. Raff, "A review on the molecular dynamics simulation of machining at the atomic scale," *P. I. Mech. Eng. B-J. Eng.*, vol. 215, no. 12, pp. 1639–1672, Nov. 2001.
- [87] S. Goel, X. Luo, and R.L. Reuben, "Molecular dynamics simulation model for the quantitative assessment of tool wear during single point diamond turning of cubic silicon carbide," *Comp. Mater. Sci.*, vol. 51, no. 1, pp. 402–408, Jan. 2012.
- [88] J.D. Silliman, *Cutting and Grinding Fluids: Selection and Application*. Dearborn, MI: Society of Manufacturing Engineers, 1992.
- [89] M.A. El Baradie, "Cutting fluids: Part I. characterisation," *J. Mater. Process. Technol.*, vol. 56, no. 1, pp. 786–797, Jan. 1996.

- [90] T. Wakabayashi, I. Inasaki, S. Suda, and H. Yokota, "Tribological characteristics and cutting performance of lubricant esters for semi-dry machining," *CIRP Ann.-Manuf. Techn.*, vol. 52, no. 1, pp. 61–64, 2003.
- [91] S.J. Skerlos, K.F. Hayes, A.F. Clarens, and F. Zhao, "Current advances in sustainable metalworking fluids research," *Int. J. Sust. Manuf.*, vol. 1, no. 1–2, pp. 180–202, 2008.
- [92] Y.M. Shashidhara and S.R. Jayaram, "Vegetable oils as a potential cutting fluid—an evolution," *Tribol. Int.*, vol. 43, no. 5, pp. 1073–1081, Jan. 2010.
- [93] E.S. Forbes, "Antiwear and extreme pressure additives for lubricants," *Tribology*, vol. 3, no. 3, pp. 145–152, Aug. 1970.
- [94] B. Shen, A.J. Shih, and S.C. Tung, "Application of nanofluids in minimum quantity lubrication grinding," *Tribol. T.*, vol. 51, no. 6, pp. 730–737, Oct. 2008.
- [95] H. Xie, W. Yu, Y. Li, and L. Chen, "Discussion on the thermal conductivity enhancement of nanofluids," *Nanoscale Res. Lett.*, vol. 6, no. 1, pp. 124, Feb. 2011.
- [96] J. Buongiorno, "Convective transport in nanofluids," *J. Heat Transf.*, vol. 128, no. 3, pp. 240–250, Mar. 2006.
- [97] L. De Chiffre, "Mechanics of metal cutting and cutting fluid action," *Int. J. Mach. Tool Des. Res.*, vol. 17, no. 4, pp. 225–234, 1977.
- [98] I. Ghai *et al.*, "Droplet behavior on a rotating surface for atomization-based cutting fluid application in micro-machining," *J. Manuf. Sci. Eng.*, vol. 132, no. 1, pp. 011017, Feb. 2010.
- [99] I. Ghai, J. Samuel, R.E. DeVor, and S.G. Kapoor, "Analysis of Droplet Spreading on a Rotating Surface and the Prediction of Cooling and Lubrication Performance of an Atomization-Based Cutting Fluid System," *J. Manuf. Sci. Eng.*, vol. 135, no. 3, pp. 031003, May 2013.
- [100] B. Lux, R. Haubner, and P. Renard, "Diamond for tooling and abrasives," *Diam. Relat. Mater.*, vol. 1, no. 10, pp. 1035–1047, Nov. 1992.
- [101] D. Dornfeld, S. Min, and Y. Takeuchi, "Recent advances in mechanical micro-machining," *CIRP Ann.-Manuf. Techn.*, vol. 55, no. 2, pp. 745–768, 2006.

- [102] H. Huang, L. Yin, and L. Zhou, "High speed grinding of silicon nitride with resin bond diamond wheels," *J. Mater. Process. Technol.*, vol. 141, no. 3, pp. 329–336, Nov. 2003.
- [103] C.J. Andrewes, H.Y. Feng, and W.M. Lau, "Machining of an aluminum/SiC composite using diamond inserts," *J. Mater. Process. Technol.*, vol. 102, no. 1, pp. 25–29, May 2000.
- [104] E. Paul, C.J. Evans, A. Mangamelli, M.L. McGlaufflin, and R.S. Polvani, "Chemical aspects of tool wear in single point diamond turning," *Precis. Eng.*, vol. 18, no. 1, pp. 4–19, Jan. 1996.
- [105] A.G. Thornton and J. Wilks, "Tool wear and solid state reactions during machining," *Wear*, vol. 53, no. 1, pp. 165–187, Mar. 1979.
- [106] H. Tanaka, S. Shimada, N. Ikawa, and M. Yoshinaga, "Wear mechanism of diamond cutting tool in machining of steel," in *Key Eng. Mat.*, vol. 196, pp. 69–78, Dec. 2000.
- [107] R. Narulkar, S. Bukkapatnam, L.M. Raff, and R. Komanduri, "Graphitization as a precursor to wear of diamond in machining pure iron: a molecular dynamics investigation," *Comp. Mater. Sci.*, vol. 45, no. 2, pp. 358–366, Apr. 2009.
- [108] Y. Wang, N. Suzuki, E. Shamoto, and Q. Zhao, "Investigation of tool wear suppression in ultraprecision diamond machining of die steel," *Precis. Eng.*, vol. 35, no. 4, pp. 677–685, Oct. 2011.
- [109] C. Evans and J.B. Bryan, "Cryogenic diamond turning of stainless steel," *CIRP Ann.-Manuf. Techn.*, vol. 40, no. 1, pp. 571–575, 1991.
- [110] A.G. Thornton and J. Wilks, "The wear of diamond tools turning mild steel," *Wear*, vol. 65, no. 1, pp. 67–74, Dec. 1980.
- [111] J.M. Casstevens, "Diamond turning of steel in carbon-saturated atmospheres," *Precis. Eng.*, vol. 5, no. 1, pp. 9–15, Jan. 1983.
- [112] F. Yavari, "Graphene nano-devices and nano-composites for structural, thermal and sensing applications," PhD dissertation, Dept. Mech. Aero. Nucl. Eng., Rensselaer Polytechnic Inst., Troy, NY, 2012.

- [113] K.A. Calzada *et al.*, “Failure mechanisms encountered in micro-milling of aligned carbon fiber reinforced polymers,” *Trans. NAMRI/SME*, vol. 38, pp. 221–228, July 2010.
- [114] K.A. Calzada, S.G. Kapoor, R.E. DeVor, J. Samuel, and A.K. Srivastava, “Modeling and interpretation of fiber orientation-based failure mechanisms in machining of carbon fiber-reinforced polymer composites,” *J. Manuf. Process.*, vol. 14, no. 2, pp. 141–149, Apr. 2012.
- [115] A. Yu, P. Ramesh, M.E. Itkis, E. Bekyarova, and R.C. Haddon, “Graphite nanoplatelet-epoxy composite thermal interface materials,” *J. Phys. Chem. C*, vol. 111, no. 21, pp. 7565–7569, April 2007.
- [116] J. Samuel, A. Dikshit, R.E. DeVor, S.G. Kapoor, and K.J. Hsia, “Effect of carbon nanotube (CNT) loading on the thermomechanical properties and the machinability of CNT-reinforced polymer composites,” *J. Manuf. Sci. Eng.*, vol. 131, no. 3, pp. 031008, May 2009.
- [117] N. Bhatnagar, N. Ramakrishnan, N.K. Naik, and R. Komanduri, “On the machining of fiber reinforced plastic (FRP) composite laminates,” *Int. J. Mach. Tools Manu.*, vol. 35, no. 5, pp. 701–716, May 1995.
- [118] R. Varatharajan, S.K. Malhotra, L. Vijayaraghavan, and R. Krishnamurthy, “Mechanical and machining characteristics of GF/P and GF/Polyester composites,” *Mater. Sci. Eng.: B*, vol. 132, no. 1, pp. 134–137, July 2006.
- [119] J. Zhu *et al.*, “Processing a glass fiber reinforced vinyl ester composite with nanotube enhancement of interlaminar shear strength,” *Compos. Sci. Technol.*, vol. 67, no. 7, pp. 1509–1517, June 2007.
- [120] K.-H. Park, A. Beal, P. Kown, and J. Lantrip, “A comparative study of carbide tools in drilling of CFRP and CFRP-Ti stacks,” *J. Manuf. Sci. Eng.*, vol. 136, no. 1, pp. 014501, Feb. 2014.
- [121] J.P. Davim, L.R. Silva, A. Festas, and A.M. Abrao, “Machinability study on precision turning of PA66 polyamide with and without glass fiber reinforcing,” *Mater. Design*, vol. 30, no. 2, pp. 228–234, Feb. 2009.

- [122] H.Y. Puw and H. Hocheng, "Milling of polymer composites," in *Machining of Ceramics and Composites*, S. Jahanmir *et al.* Eds., New York, NY: Marcel Dekker, 1999, pp. 267-294.
- [123] X. Zhang *et al.*, "Interfacial microstructure and properties of carbon fiber composites modified with graphene oxide," *ACS Appl. Mater. Interfaces*, vol. 4, no. 3, pp. 1543–1552, Mar. 2012.
- [124] J. Lin, L. Wang, and G. Chen, "Modification of graphene platelets and their tribological properties as a lubricant additive," *Tribol. Lett.*, vol. 41, no. 1, pp. 209–215, Jan. 2011.
- [125] M.M. Maru and D.K. Tanaka, "Consideration of stribeck diagram parameters in the investigation on wear and friction behavior in lubricated sliding," *J. Braz. Soc. Mech. Sci.* vol. 29, no. 1, pp. 55–62, Mar. 2007.
- [126] W.S. Hummers Jr and R.E. Offeman, "Preparation of graphitic oxide," *J. Am. Chem. Soc.*, vol. 80, no. 6, pp. 1339–1339, Mar. 1958.
- [127] M.J. McAllister *et al.*, "Single sheet functionalized graphene by oxidation and thermal expansion of graphite," *Chem Mater.*, vol. 19, no. 18, pp. 4396–4404, May 2007.
- [128] S. You, S.M. Luzan, T. Szabó, and A.V. Talyzin, "Effect of synthesis method on solvation and exfoliation of graphite oxide," *Carbon*, vol. 52, pp. 171–180, Sep. 2013.
- [129] J.P. Rourke *et al.*, "The real graphene oxide revealed: stripping the oxidative debris from the graphene-like sheets," *Angew. Chem.*, vol. 123, no. 14, pp. 3231–3235, Mar. 2011.
- [130] A. Braun *et al.*, "Validation of dynamic light scattering and centrifugal liquid sedimentation methods for nanoparticle characterisation," *Adv. Powder Technol.*, vol. 22, no. 6, pp. 766–770, Nov. 2011.
- [131] M.D. Stoller, S. Park, Y. Zhu, J. An, and R.S. Ruoff, "Graphene-based ultracapacitors," *Nano Lett.*, vol. 8, no. 10, pp. 3498–3502, Sep. 2008.
- [132] Q. Du *et al.*, "Preparation of functionalized graphene sheets by a low-temperature thermal exfoliation approach and their electrochemical

- supercapacitive behaviors,” *Electrochim. Acta*, vol. 55, no. 12, pp. 3897–3903, Apr. 2010.
- [133] N.R. Karthikeyan, J. Philip, and B. Raj, “Effect of clustering on the thermal conductivity of nanofluids,” *Mater. Chem. Phys.*, vol. 109, no. 1, pp. 50–55, May 2008.
- [134] B. Chu, E. Singh, N. Koratkar, and J. Samuel, “Graphene-enhanced environmentally-benign cutting fluids for high-performance micro-machining applications,” *J. Nanosci. Nanotechnol.*, vol. 13, no. 8, pp. 5500–5504, Aug. 2013.
- [135] P.J. Bittorf, S.G. Kapoor, R.E. DeVor, and N. Rajagopalan, “Effect of water phase surface tension and viscosity on metalworking fluid functionality,” *Trans. NAMRI/SME*, vol. 34, pp. 555–562, 2006.
- [136] P.J. Bittorf, S.G. Kapoor, and R.E. DeVor, “Transiently stable emulsions for metalworking fluids,” *Trans. NAMRI/SME*, vol. 35, pp. 343–350 2007.
- [137] P. Kwon, T. Schiemann, and R. Kountanya, “An inverse estimation scheme to measure steady-state tool–chip interface temperatures using an infrared camera,” *Int. J. Mach. Tools Manu.*, vol. 41, no. 7, pp. 1015–1030, May 2001.
- [138] F. Girard, M. Antoni, S. Faure, and A. Steinchen, “Evaporation and Marangoni driven convection in small heated water droplets,” *Langmuir*, vol. 22, no. 26, pp. 11085–11091, Dec. 2006.
- [139] B. Chu, E. Singh, J. Samuel, and N. Koratkar, “Graphene oxide colloidal suspensions as cutting fluids for micro-machining—Part I: Fabrication and performance evaluation,” *J. Micro Nano-Manuf.*, vol. 3, no. 4, pp. 041002–041002, Aug. 2015.
- [140] M.I. Baskes, “Modified embedded-atom potentials for cubic materials and impurities,” *Phys. Rev. B*, vol. 46, no. 5, pp. 2727–2742, Aug. 1992.
- [141] M.I. Baskes, “Determination of modified embedded atom method parameters for nickel,” *Mater. Chem. Phys.*, vol. 50, no. 2, pp. 152–158, Sep. 1997.
- [142] H. Fang *et al.*, “Numerical Tools for Atomistic Simulations,” Sandia Nat. Lab., Albuquerque, NM, Rep. SAND2003-8782, 2004.

- [143] L.S.I. Liyanage *et al.*, “Structural, elastic, and thermal properties of cementite Fe₃C calculated using a modified embedded atom method,” *Phys. Rev. B*, vol. 89, no. 9, pp. 094102, Mar. 2014.
- [144] C.A. Becker, F. Tavazza, Z.T. Trautt, and R.A.B de Macedo, “Considerations for choosing and using force fields and interatomic potentials in materials science and engineering,” *Curr. Opin. Solid St. M.*, vol. 17, no. 6, pp. 277–283, Dec. 2013.
- [145] S. Plimpton, “Fast Parallel Algorithms for Short-Range Molecular Dynamics,” *J. Comp. Phys.*, vol. 117, no. 1, pp. 1–19, Mar. 1995.
- [146] A. Stukowski, “Structure identification methods for atomistic simulations of crystalline materials,” *Modelling Simul. Mater. Sci. Eng.*, vol. 20, no. 4, pp. 045021, May 2012.
- [147] A. Bródka, T. W. Zerda, and A. Burian, “Graphitization of small diamond cluster — Molecular dynamics simulation,” *Diam. Relat. Mater.*, vol. 15, no. 11–12, pp. 1818–1821, Nov. 2006.
- [148] A. Bródka, A. Burian, S. Tomita, and V. Honkimäki, “Molecular dynamics study of structure and graphitization process of nanodiamonds,” *J. Mol. Struct.*, vol. 887, no. 1–3, pp. 34–40, Sep. 2008.
- [149] B. Chu and J. Samuel, “Graphene oxide colloidal suspensions as cutting fluids for micro-machining—Part II: Droplet dynamics and film formation,” *J. Micro Nano-Manuf.*, vol. 3, no. 4, pp. 041003–041003, Aug. 2015.
- [150] M.S. Uddin, K.H.W. Seah, X.P. Li, M. Rahman, and K. Liu, “Effect of crystallographic orientation on wear of diamond tools for nano-scale ductile cutting of silicon,” *Wear*, vol. 257, no. 7–8, pp. 751–759, Oct. 2004.
- [151] P. Koshy, R.C. Dewes, and D.K. Aspinwall, “High speed end milling of hardened AISI D2 tool steel (~58 HRC),” *J. Mater. Process. Technol.*, vol. 127, no. 2, pp. 266–273, Sep. 2002.
- [152] R. Connolly and C. Rubenstein, “The mechanics of continuous chip formation in orthogonal cutting,” *Int. J. Mach. Tool Des. Res.*, vol. 8, no. 3, pp. 159–187, Oct. 1968.

- [153] K. Iwata, T. Morikawi, and K. Okuda, "Analysis of cutting temperature in ultra-high precision diamond cutting of copper," *J. Jpn. Soc. Precis. Eng.*, vol. 53, no. 8, pp. 1253–1258, 1987.
- [154] T. Ueda, M. Sato, and K. Nakayama, "The temperature of a single crystal diamond tool in turning," *CIRP Ann.-Manuf. Techn.*, vol. 47, no. 1, pp. 41–44, 1998.
- [155] A. Dikshit, J. Samuel, R.E. DeVor, and S.G. Kapoor, "Microstructure-level machining simulation of carbon nanotube reinforced polymer composites—Part I: Model development and validation," *J. Manuf. Sci. Eng.*, vol. 130, no. 3, pp. 031114–031114, May 2008.
- [156] A. Gupta, T. Sakthivel, and S. Seal, "Recent development in 2D materials beyond graphene," *Prog. Mater. Sci.*, vol. 73, pp. 44–126, Aug. 2015.
- [157] B. Chu, J. Samuel, and N. Koratkar, "Micromilling responses of hierarchical graphene composites," *J. Manuf. Sci. Eng.*, vol. 137, no. 1, p. 011002, Sep. 2014.

Author's Biography

Bryan Chu is a PhD candidate in the Dept. of Mechanical Aerospace and Nuclear Engineering at Rensselaer Polytechnic Institute. His current research interests involve investigating the use of graphene and other 2D materials for micro-machining applications, developing ontologies for additive manufacturing processes, and developing molecular dynamics models for ultraprecision machining operations. In addition, he has also worked on industry-funded research investigating the use of ultrasonic micro-drilling techniques to reduce the manufacturing costs of gas direct-injection seats and the design of energy harvesting devices for rotary wing aircrafts. His research efforts at Rensselaer have resulted in a total of 8 journal articles (6 published, 1 in-review and 1 in-preparation) and 4 conference papers. He currently holds a Bachelor of Science degree in Mechanical Engineering from Cornell University (2011) and is expected to complete his PhD work (supervised by Prof. Johnson Samuel) in May 2016.